Silicon-On-Insulator Photonic Components with a Liquid Crystal Upper Cladding

Fotonische componenten in silicium-op-isolator met een toplaag van vloeibare kristallen

Thomas Ako

Promotoren: prof. dr. ir. J. Beeckman, prof. dr. ir. K. Neyts
Proefschrift ingediend tot het behalen van de graad van
Doctor in de Ingenieurswetenschappen: Elektrotechniek

Vakgroep Elektronica en Informatiesystemen
Voorzitter: prof. dr. ir. R. Van de Walle
Faculteit Ingenieurswetenschappen en Architectuur
Academiejaar 2014 - 2015

UNIVERSITEIT
GENT

ISBN 978-90-8578-820-1
NUR 959
Wettelijk depot: D/2015/10.500/63

Universiteit Gent
Faculteit Ingenieurswetenschappen en architectuur
Vakgroep Elektronica en Informatiesystemen

Fotonische componenten in silicium-op-isolator met een toplaag van vloeibare kristallen

Silicon-On-Insulator Photonic Components with a Liquid Crystal Upper Cladding

---

Thomas Ako

Proefschrift tot het bekomen van de graad van
Doctor in de Ingenieurswetenschappen:
Elektrotechniek
Academiejaar 2014-2015

Universiteit Gent
Faculteit Ingenieurswetenschappen en
architectuur
Vakgroep Elektronica en Informatiesystemen

Promotoren: Prof. Dr. Ir. Jeroen Beeckman
Prof. Dr. Ir. Kristiaan Neyts

Examencommissie: Prof. Dr. Ir. Luc Taerwe (Voorzitter), UGent, Bouwkundige Constructies
Prof. Dr. Ir. Jeroen Beeckman (Promotor), UGent, ELIS
Prof. Dr. Ir. Kristiaan Neyts (Promotor), UGent, ELIS
Prof. Dr. Ir. Wim Bogaerts, UGent, INTEC
Prof. Dr. Ir. Pascal Kockaert, Université Libre de Bruxelles
Prof. Dr. Ir. Jos van der Tol, Technische Universiteit Eindhoven
Prof. Dr. Ir. Patrick De Visschere (Secretaris), UGent, ELIS
Prof. Dr. Ir. Herbert De Smet, UGent, ELIS

Universiteit Gent
Faculteit Ingenieurswetenschappen en architectuur

Vakgroep Elektronica en Informatiesystemen
Sint Pietersnieuwstraat 41, B-9000 Gent, België

Tel.: +32-9-264.33.66
Fax.: +32-9-264.35.94

Proefschrift tot het behalen van de graad van
Doctor in de Ingenieurswetenschappen:
Elektrotechniek
Academiejaar 2014-2015

Dankwoord

dankwoord...

Aalter, Augustus 2014
Thomas Ako

Table of Contents

List of Figures

List of Tables

List of Acronyms

B

BVP	Boundary Value Problem

C

CD	Compact Disc
CMOS	Complementary Metal Oxide Semiconductor

D

DBR	Distributed Bragg Reflector
DFB	Distributed feedback
DVD	Digital Video Disc

F

FDTD	Finite Difference Time Domain
FEM	Finite Element Method

H

HCG	High Contrast Grating

I

IMEC	Interuniversity Microelectronics Center
IR	Infra Red
ITO	Indium Tin Oxide
IYL	International Year of Light

L

LC	Liquid Crystal
LCD	Liquid Crystal Display

P

PML	Perfectly Matched Layer
PMMA	Poly(methyl metacrylate

R

RF	Radio Frequency

S

SOI	Silicon On Insulator
SWA	Slab Waveguide Array
SEM	Scanning Electron Microscope

T

TE	Transverse Electric

TM	Transverse Magnetic

U

UV	Ultra Violet

V

VCSEL	Vertical Cavity Surface Emitting Laser

Nederlandse samenvatting

Licht en lichtgebaseerde technologie is van groot belang in onze huidige maatschappij. Fotonica is de wetenschap en technologie rond de generatie, transmissie en detectie van licht. De meest gekende toepassingen van fotonica zijn optische sensors, verlichting, beeldschermen en optische communicatiesystemen. Het is moeilijk voor te stellen hoe het leven zou zijn zonder de huidige beeldschermtechnologie en optische communicatiesystemen. De geavanceerde beeldschermtechnologie heeft het mogelijk gemaakt om smartphones en TVs te maken die beelden met hoge resolutie en kleuren kunnen weergeven. Anderzijds zorgt het optische communatienetwerk voor de lange afstandscommunicatie voor onder meer het internet. Nochtans is elektronica nog steeds noodzakelijk voor communicatie over korte afstanden, voor interconnecties op chipniveau en voor signaalverwerking. De wet van Moore en de continue vraag naar chips met lagere kostprijs en meer rekenkracht heeft ertoe geleid dat steeds meer transistoren op een elektronische chip kunnen geplaatst worden. Maar deze manier van werken heeft ook zijn grenzen bereikt aangezien de hoge densiteit aan transistoren problemen heeft i.v.m. afvoeren van de gegenereerde warmte, lekstromen en overspraak. Fotonica heeft het potentieel om minstens een aantal van deze problemen op te lossen. Fotonische chips waarin de metalen interconnecties vervangen worden door optische interconnecties werden reeds voorgesteld. Zulke fotonische chips in silicium zijn interessant omdat ze compatibel zijn met de huidige CMOS fabricage- en verwerkingstechnologie die vandaag de dag gebruikt wordt voor elektronische chips. Daarnaast biedt het silicium-op-isolator platform een hoog brekingsindexcontrast, waardoor sub-micrometer componenten met vrij kleine bochten kunnen gemaakt worden. Tot slot zou het silicium platform hoge transmissiesnelheden aankunnen en lagere warmteontwikkeling vertonen doordat fotonen niet tot resistieve warmteontwikkeling leiden zoals elektrische stromen.

Ondanks enkele attractieve aspecten is silicium fotonica niet in staat om bepaalde functies te vervullen. Dit is vooral omwille van het feit dat silicium een materiaal is met centro-symmetrische kristalstructuur. Hierdoor is er geen lineair elektro-optisch effect. Silicium heeft wel een tweede-orde elektro-optisch effect, maar dit effect is in de praktijk onbruikbaar door generatie van vrije ladingsdragers. Bijgevolg wordt het afstemmen van fotonische componenten vandaag de dag gedaan via het thermo-optische effect. Het instellen van een bepaalde temperatuur gebeurt via resistieve opwarming. Het gevolg is dat een constant elektrisch vermogen nodig is en dat de afstembereikbaarheid klein is. De integratie van geschikte elektro-optische materialen zoals vloeibare kristallen kan dit oplossen.

Het succes van beeldschermtechnologie is vooral toe te schrijven aan het succes van vloeibare kristallen. Vloeibare kristallen zijn materialen met een bijkomende vloeibaar-kristallijne fase die qua temperatuur tussen de vaste en de vloeibare fase kan gevonden worden. Vloeibaarkristalmaterialen hebben een bepaalde ordening op lange afstanden (meerdere molecuulafstanden). De gemiddelde oriëntatie van de moleculen wordt de director genoemd. De ordening is een eigenschap die typisch geassocieerd wordt met kristallen. Anderzijns hebben nematische vloeibare kristallen geen positionele ordening, maar zijn ze wel vloeibaar. Vloeibaarkristalmoleculen hebben typisch een langwerpige vorm met één lange as en twee korte assen. Ze worden gekarakteriseerd door een optische en een diëlektrische anisotropie die overeenkomt met een verschil in eigenschappen langs de korte en de lange as van het vloeibaar kristal. De diëlektrische anisotropie maakt het mogelijk dat vloeibare kristallen zich heroriënteren onder invloed van een aangelegd elektrisch veld. Deze heroriëntatie resulteert in een verandering in optische eigenschappen van het vloeibaar kristal. Aangezien de anisotropie van vloeibare kristallen groot is t.o.v. andere materialen, hebben vloeibare kristallen uitstekende elektro-optische eigenschappen. Hierdoor zijn vloeibaar-kristalbeelschermen vandaag de dag de meest gebruikte vlakke beeldschermtechnologie. In de pixels van zo een beeldscherm wordt de transmissie door de verschillende pixels veranderd door elektrische spanningen aan te leggen. De elektro-optische eigenschappen van vloeibare kristallen zorgen er ook voor dat ze een interessant materiaal zijn voor de integratie met silicium fotonische componenten. Eerder onderzoek had reeds veelbelovende resultaten opgeleverd, waaronder het afstemmen van ring resonatoren. In dit werk zullen we werken met ondiep-geëtste golfgeleiders, hoog-contrast-roosterreflectors en diep geëtste golfgeleiders. Wanneer elk van deze componenten is bedekt met een vloeibaar kristal, dan zal een heroriëntatie van het vloeibaar kristal de brekingsindex veranderen rond de component. De verandering in die brekingsindex heeft ook een effect op de effectieve index van de optische golfgeleidermodes en de reflectiviteit van de roosters. Aangezien de oriëntatie van het vloeibaar kristal (en dus de brekingsindex van de omgeving van de component) kan veranderd worden door een spanning aan te leggen is het dus mogelijk om silicium fotonische componenten te bekomen met spanningsafstembare functionaliteit.

Ondiep geëtste golfgeleiders

Zoals de naam al doet vermoeden hebben ondiep geëtste golfgeleiders een laag silicium naast de golfgeleiderkern dat lichtjes dunner is dan de kern. Het licht in de golfgeleider is gevangen in de verticale richting door het brekingsindexcontrast tussen het oxide, de silicium kern en lucht. Het licht is lateraal ook gevangen door het verschil in dikte van de siliciumlaag. Het hoge indexcontrast tussen de kern en de cladding heeft tot gevolg dat de golfgeleider dubbelbrekende golfgeleidermodes ondersteunt. De modes zijn hybride maar kunnen toch in twee klassen onderverdeeld worden: de transversaal elektrische (quasi-TE) mode en de transversaal magnetische (quasi-TM) mode. De quasi-TE mode heeft de grootste elektrische component langs de laterale (loodrecht op de zijwanden van de golfgeleider) as. De verticale (loodrechts op de substraat) en longitudinale (langs de voortplantingsrichting) component zijn niet nul, maar zijn gevangen in de golfgeleiderkern. Bij de quasi-TM mode anderzijds is de elektrische component het grootst langs de verticale as. De laterale en longitudinale component zijn echter niet-nul op een afstand van de golfgeleiderkern, namelijk in het ondiep geëtste deel van de golfgeleider. Voor de quasi-TM mode in ondiep geëtste (zowel rechte als gekromde) golfgeleiders en ring resonatoren werd aangetoond (zowel theoretisch als experimenteel) dat er verliezen optreden afhankelijk van de breedte van de golfgeleiderkern. Dit komt door het feit dat de effectieve index van de quasi-TM modes ongeveer gelijk is aan de effectieve index van de niet-geleide (stralende) TE mode in de ondiep geëtste cladding. Aangezien dit een stralende mode is, kan die propageren in om het even welke richting. Bijgevolg is er een hoek waaronder de quasi-TM mode kan fase-gekoppeld met de stralende TE mode. Die laterale lekverliezen volgen een cyclisch patroon in functie van de breedte van de golfgeleiderkern. De breedte waarbij de lekverliezen minimaal zijn worden magische breedtes genoemd. Analoog is er ook een golflengte (bij een vaste breedte) waarbij de lekverliezen minimaal zijn: de magische golflengte.

In mijn doctoraat heb ik de afstembaarheid onderzocht van de magische breedte en golflengte voor de fundamentele quasi-TM mode in ondiep geëtste golfgeleiders. Het mechanisme van laterale lekverliezen voor een golfgeleider bedekt met lucht wordt uitgelegd en deze theorie wordt uitgebreid voor het geval van een anisotrope toplaag. Dankzij simulaties van het lateraal lekmechanisme worden ondiep geëtste golfgeleiders ontworpen met optimale parameters voor de experimentele karakterisatie. Gedurende de ontwerpfase werd een vloeibaar kristalsimulator gebruikt om de director oriëntatie in de vloeibaar-kristallaag te berekenen voor verschillende aangelegde spanningen. Deze directororiëntatie wordt dan gebruikt in de modeberekening die de effectieve indices van de modes oplevert. De laterale lekverliezen van een mode kan berekend worden via het imaginair gedeelde van de effectieve index. Hierdoor wordt het mogelijk om te voorspellen welke golfgeleiderbreedtes magisch zijn. Componenten werden gemaakt waarbij de silicium chip (met de golfgeleiders) het onderste substraat is en een glasplaat het bovenste substraat. Beide substraten worden samengehouden door UV lijm. Kleine balletjes worden gemengd met de lijm om de dikte van de luchtlaag tussen de twee substraten te bepalen. De component wordt dan gevuld met vloeibaar kristal via cappilaire werking. De bovenste glasplaat heeft een indium tin oxide (ITO) laag, een laag polymethylmetacrylaat (PMMA) en een nylon aligneringslaag. Het ITO en het onderste substraat hebben elektrische contacten om een spanning over het vloeibaar kristal te kunnen aanleggen. De PMMA-laag zorgt ervoor dat het evanescente licht van de mode niet geabsorbeerd wordt door het ITO. De nylon aligneringslaag zorgt ervoor dat de director een gepaste oriëntatie heeft. De oriëntatie van het vloeibaar kristal werd onderzocht met een polarisatiemicroscoop. Het vloeibaar kristal is parallel met de golfgeleiders. Wanneer een spanning wordt aangelegd heroriëntert de director zodat hij een hoek maakt met het substraatoppervlak. Als de spanning verder wordt opgedreven is de director vrijwel evenwijdig met de normaal op het oppervlak van het substraat.

Als TM gepolariseerd licht in de golfgeleider wordt geschoten is het mogelijk om de laterale lekverliezen te veranderen. Metingen werden gedaan van de verliezen in functie van de aangelegde spanning voor verschillende componenten met verschillende dikte. De silicium chip in elke component heeft verschillende golfgeleiders en de metingen worden uitgevoerd voor het golflengtegebied van 1510 nm tot 1590 nm. De resultaten zijn in goede overeenstemming met de simulaties, wat aantoont dat het mechanisme goed begrepen wordt. Voor een breedte van 785 nm is het mogelijk om de magische golflengte over 39.5 nm te verschuiven (van 1564 nm tot 1524.5 nm) met spanningen die variëren van 0 V$_{rms}$ tot 200 V$_{rms}$. We tonen ook aan dat het mogelijk is om de verliezen zowel te verhogen als te verlagen voor verschillende golflengtes. Het is bijvoorbeeld mogelijk om de transmissieverliezen te veranderen met 20 dB/cm.

Hoog-contrastroosters

Een hoog-contrastrooster (HCG) is een rooster met een hoog brekingsindexcontrast tussen het roostermateriaal en de omgeving en werkt in het nabije-golflengtegebied. In dit regime is de periode van het rooster kleiner dan de golflengte van het invallende licht, maar groter dan de golflengte in het roostermateriaal. HCGs worden bestudeerd omwille van hun opmerkelijke reflectieve eigenschappen. Voor TM gepolariseerd licht (loodrecht met de roosterlijnen) en loodrechte inval vertonen ze breedbandige ($\frac{\Delta\lambda}{\lambda} = 35\text{nm}$) reflectiviteit ($> 99\%$). TE gepolariseerd licht (parallel met de roosterlijnen) dat loodrecht invalt vertoont scherpe pieken met hoge Q-factor die gekenmerkt zijn door een snelle verandering in reflectiviteit, gaange van bijna 0% tot bijna 100% over een small golflengtegebied. De meest voor de hand liggende toepassing van HCGs is als vervanger voor gedistribueerde Bragg reflectoren voor de topspiegel van VCSELs. Ook zijn er applicaties in vlak focuserende reflectoren/lenzen en holle-kerngolfgeleiders.

De reflectieve eigenschappen van HCGs zijn volledig bepaald door hun geometrie (i.e. de periode, dikte en vulfactor) en ze kunnen uitgelegd worden door ze te beschouwen als een sub-golflengte golfgeleider reeks (SWA). Wanneer licht invalt op een HCG propageren de SWA modes in een richting parallel met de normaal op de HCG. In het nabije golflengtegebied zijn er exact twee SWA modes. Dankzij het grote brekingsindexverschil tussen de bovenste en onderste interface worden de SWA modes terug gereflecteerd in de HCG en koppelen ze terug naar elkaar. Bijgevolg bestaan er Fabry-Perot resonantievoorwaarden voor beide modes. Voor een HCG met een bepaalde geometrie bereiken beide SWA modes hun Fabry-Perot resonantie tegelijkertijd. Voor TM gepolariseerd licht correspondeert een breedbandige reflectie met de conditie van π faseverschil, m.a.w. destructieve interferentie tussen beide SWA modes, bij het uitgangsvlak. Aangezien het nabije golflengtekarakter van de HCG diffractie verbiedt naar hogere order modes wordt al het licht gereflecteerd. Anderzijds corresponderen de resonatiepieken van TE gepolariseerd licht met constructieve interferentie van de SWA modes. Dit leidt tot opbouw van elektrisch veld binnen de HCG. Deze opbouw is verantwoordelijk voor de scherpe veranderingen in reflectie over een klein golflengtegebied.

HCGs die werken voor TE en TM hebben evenveel potentieel om afgestemd te worden. Maar het is gemakkelijker om een verschuiving te meten van een smalle piek, dan van een brede piek. Bovendien aligneren de vloeibaar-kristalmoleculen bij voorkeur parallel aan de longitudinale structuren van het rooster. Bijgevolg wordt in dit werk gefocust op HCGs met vloeibaar-kristaltoplaag in het golflengtegebied van 1500 nm tot 1700 nm voor TE gepolariseerd licht dat loodrecht invalt. Het vloeibaar-kristalsimulatieprogramma in combinatie met een eindige elementen gebaseerde frequentiedomein oplosser wordt gebruikt om de reflectiviteit van verschillende HCGs te simuleren. Rekening houdende met enkele eenvoudige ontwerpregels en met de limitaties van de fabricagetechnologie worden enkele HCGs ontworpen met licht verschillende parameters (periode, dikte en vulfactor). Met deze chips worden componenten gemaakt waarbij het onderste substraat de silicium chip is (met de HCGs) en het bovenste een glassubstraat. Beide worden samengehouden door UV hardende lijm. Balletjes van enkele micrometer groot worden gemengd met de lijm om de dikte van de luchtlaag te bepalen, waarna vloeibaar kristal wordt ingebracht. De oriëntatie van het vloeibaar kristal wordt gecontroleerd met een polarisatiemicroscoop. Het vloeibaar kristal blijkt parallel te oriënteren met de roosterlijnen. Wanneer een elektrische spanning wordt aangelegd heroriënteren de vloeibaar-kristalmoleculen zodat ze meer en meer via de normaal op het substraat komen te liggen.

Simulaties tonen aan dat de HCGs met vloeibaar kristal een bredere TE reflectiepiek hebben in vergelijking met de HCGs in lucht. De totale dimensie van de HCGs is 50μm bij 50μm. Doordat ze zo klein zijn is het noodzakelijk om een setup te bouwen die zowel met visueel licht werkt om de HCGs te visualiseren als met infrarood licht om de reflectie te bepalen. Met deze setup worden metingen uitgevoerd van het gereflecteerde vermogen in functie van de aangelegde spanning bij een vaste golflengte. Deze metingen bevestigen dat de reflectie spanningsafhankelijk is. Daarnaast worden ook metingen uitgevoerd in functie van de golflengte bij vaste spanningen. Deze metingen tonen aan dat de reflectie golflengteafhankelijk is.

Diep geëtste golfgeleiders

Diep geëtste golfgeleiders zijn eenvoudige types golfgeleiders die bestaan uit een silicium laag die volledig geëtst is zodat enkel een small stuk silicium overblijft (typisch met een breedte kleiner dan 1μm bovenop de oxidelaag. Door hun compacte afmetingen zijn ze zeer geschikt voor dichte integratie. Dankzij hun geometrie en hun hoge indexcontrast (net zoals ondiep geëtste golfgeleiders) zijn er TE en TM golfgeleidermodes. Dankzij het gebruik van vloeibaar kristal kunnen ze afstembaar gemaakt worden via het aanleggen van een spanning. De TE mode vertoont een elektrisch veld dat sterk gebonden in aan de kern. De afstembaarheid is klein. Een sterke component van het elektrisch veld is de laterale component die loodrecht staat op de zijwanden van de golfgeleider. De longitudinale component (langs de voortplantingsrichting) is ook vrij groot. Bijgevolg kan het afstemmen bereikt worden door het vloeibaar kristal eerst in de laterale richting te leggen en daarna te draaien zodat het evenwijdig komt met de longitudinale richting. De TM mode is niet zo sterk aan de kern gebonden. Bijgevolg is de afstembaarheid ook groter in vergelijking met TE. De sterkste component van het elektrisch veld is de verticale component (loodrecht op het substraat). De laterale en longitudinale componenten zijn ook relatief groot. De afstembaarheid van de TM mode kan bereikt worden door het vloeibaar kristal ofwel langs de laterale of the longitudinale richting te leggen en dan te draaien zodat het evenwijdig komt langs de verticale richting. Maar in praktische situaties is enkel het heroriënteren van longitudinaal naar verticaal mogelijk. Dat komt door het feit de het vloeibaar kristal prefereert om langs (de hoeken) van de golfgeleider te liggen.

Het ontwerp gaat verder als volgt: de vloeibaar-kristalberekening wordt gebruikt om de oriëntatie te bepalen. Deze data wordt dan gebruikt in de modeberekening die de effectieve index van de mode oplevert. De berekening gebeurt voor verschillende spanningen en golfgeleiderbreedtes. Voor elke mode wordt de geschikte beginoriëntatie van het vloeibaar kristal gebruikt. De simulaties tonen dat de effectieve indices van de TE en de TM modes in deze golfgeleiders kunnen aangepast worden, waarbij TM een grotere afstembaarheid heeft. Voor voldoende dunne golfgeleiders is er een spanningsgereguleerde cut-off van de fundamentele TE en TM mode mogelijk.

English summary

Light and light-based technologies fulfill a very important role in our society today. The technologies related to the generation, transmission and detection of light are collectively referred to as photonics. The most notable applications of photonics include optical sensors, lighting, display technology and optical communication systems. It is hard to imagine what life would be like today without current display technology and optical communications. Display technology has made it possible to have smart phones and TVs with high definition picture quality. On the other hand, optical communication systems are at the heart of the long-haul telecommunication systems which constitute the internet. However, electronics is still indispensable for short-distance communications, chip-level interconnection and signal processing. Driven by Moore's law and increasing demand for low-cost chips with higher processing speeds, engineers have found clever ways to pack an ever increasing number of transistors into electronic chips. This approach has its limits though, since current densely integrated electronic chips suffer from drawbacks like heat buildup, current leakage and crosstalk. Photonics has a huge potential which can be harnessed to overcome these difficulties. Photonic chips in which copper interconnects are replaced by silicon interconnects have been proposed. This so-called silicon photonic chips are very attractive because they are compatible with CMOS fabrication and processing technology currently used to manufacture electronic chips. Additionally, the silicon-on-insulator platform used for silicon photonics has a high refractive index contrast. This makes it possible to use sub-micrometer-sized components with very small bends, resulting in dense integration. Finally, silicon photonic chips should in principle yield higher speeds and lower power consumption since they work using light which propagates faster than electrons.

Despite its attractive features, silicon photonics cannot yet fulfill certain functions. This is mostly down to the fact that silicon being a material with a centro-symmetric crystal structure has no linear electro-optic effect. It does have a second-order electro-optic effect but its magnitude is small and its use is hampered by free-carrier generation. Consequently, tunability in silicon photonics is typically achieved by thermo-optical means through the use of resistive heaters. However, this approach needs a constant power supply and has a limited tuning range. As a result, it is necessary to integrate liquid crystals with a other materials in order to obtain chips with optimal electro-optic functionality.

Display technology owes much of its success to liquid crystals. Liquid crystals are materials which have an additional (liquid crystal (LC)) phase between the solid and liquid phases. LCs have long range orientational order, the common orientation is the director. This orderliness is a property usually associated with a crystal. On the other hand, LCs have no positional order, they retain the macroscopic properties of a liquid. LC molecules are typically elongated with one long (preferred) axis and two short axes. They are characterized by optical and dielectric anisotropy which arises from the difference in optical and dielectric properties along the long and short axes of the LC. The dielectric anisotropy means LCs reorient themselves in the presence of an applied electric field. This reorientation results in a change in the optical properties of the LC. Since the optical anisotropy of LCs can be large, this voltage-driven reorientation mechanism means LCs have excellent electro-optic behavior. This is precisely the property which has resulted in their widespread use in displays, where the transmission of pixels containing LC must be changed from a low (dark) to a high (bright) state by the application of a low voltage. The electro-optic effect of LCs makes them ideal for integration with silicon photonic devices. This has indeed researched earlier and has resulted in the tuning of silicon ring resonators. In this work, we intend to use LCs to tune the properties of shallow-etched waveguides, high contrast grating reflectors and deep-etched waveguides. When each of these devices are clad with LC, a reorientation of the LC means a change of the refractive index around the device. This refractive index change has an effect on the effective indices of the waveguides and reflectivity of the high contrast gratings. Since the orientation of the LC (and hence the index of the device's surrounding) can be varied by varying the voltage applied over it, it is thus possible to obtain LC-clad silicon photonic devices with voltage-tunable functionality.

Shallow-etched waveguides

Like their name implies, shallow-etched waveguides have a shallow-etch of silicon flanking either side of the waveguide core. The light in the waveguide is confined vertical direction by the index mismatch between the oxide, the silicon core and air. Lateral confinement is provided by the step-height difference between the waveguide core and the shallow-etch. The high index contrast between the waveguide core and cladding means that when light is launched into the waveguide, it supports birefringent waveguide modes. The modes are hybrid but can be divided into two main classes; the transverse electric (TE-like) and transverse magnetic (TM-like) modes. For the TE-like mode, the main component of the electric field is the lateral (perpendicular to the side walls of the waveguide) component. The vertical (normal to the waveguide's top surface) and longitudinal (parallel to the waveguide) components are non-zero but they are confined to the core of the waveguide. On the other hand, for the TM-like mode the main component of the electric field is the vertical component. The lateral and longitudinal components are non-zero away from the waveguide core i.e. in the shallow-etched cladding of the waveguide. The TM-like waveguide mode in shallow-etched (bent and straight) waveguides and ring resonators has been shown (both theoretically and experimentally) to exhibit waveguide-width-dependent lateral leakage loss. This arises because the effective index of the TM-like waveguide mode is comparable to the effective index of the unguided radiating TE-like shallow-etched cladding mode. Since the latter is unguided, it can propagate in any direction. Consequently, there is an angle at which it is phase-matched to the TM-like waveguide mode along the z-axis. The lateral leakage loss of the waveguide plotted as a function of the waveguide width follows a cyclic pattern with well defined minima. The waveguide widths at which the lateral leakage loss is minimal are the magic widths. The wavelength analogue of the magic width (magic wavelength) has also been reported. i.e. For a waveguide with a fixed width, the lateral leakage loss plotted as a function of the wavelength follows a cyclic pattern with well defined minima.

In my research I investigate the tunability of the magic width and magic wavelength for the fundamental TM-like mode in LC-clad shallow-etched waveguides. I review the lateral leakage loss mechanism for an air-clad shallow-etched waveguide and extend it to the case where the shallow-etched waveguides have an anisotropic cladding. Using the understanding of the lateral leakage loss mechanism, I design shallow-etched waveguides with optimal parameters for experimental characterization. During the design phase, I use an LC solver to calculate the director distribution in the LC layer above the waveguides for various applied voltages. This director distribution is imported into a mode solver which computes the effective indices of the modes supported by the waveguides. The lateral leakage loss of a mode is extracted from the imaginary part of its effective index. This makes it possible to determine which waveguides are magic in the wavelength window of our measurement setup. I then fabricate cells in which the silicon chip (with the waveguides) is the bottom plate and a glass plate is the top plate. Both plates are held together by UV curable glue. Spacer balls mixed with the glue determine the cell gap. The cell is filled with LC by capillary action. The glass plate has a conductive indium tin oxide (ITO) layer, a layer of polymethyl methacrylate (PMMA) and a nylon alignment layer. The ITO and the bottom part (silicon substrate) of the chip have electrical contacts for applying a voltage over the LC. The PMMA makes sure evanescent light from the waveguide is not absorbed by the ITO. The nylon alignment layer ensures the LC director has an appropriate orientation. The orientation of the LC above the waveguides is checked with a polarization microscope. The LC are found to be parallel with the waveguides. When a voltage is applied to the cell, the LCs reorient so that the director makes an angle with the normal to the waveguide surface. As the voltage is increased further, the angle the director makes with the normal to the waveguide surface reduces.

When TM polarized light is launched in the shallow-etched waveguides, it is possible to tune their lateral leakage loss. I perform measurements of the loss as a function of the applied voltage for several cells with different thicknesses. The silicon chip in each cell has several waveguides and the measurements are performed for the wavelength window from 1510nm to 1590nm. The measurement results are found to be in agreement with simulations, indicating that the mechanism by which the device works is well understood. For a 785nm wide shallow-etched waveguide, it is possible to shift the minimum in leakage loss by 39.5 nm from 1564 nm to 1524.5 nm by changing the applied voltage from 0 V$_{rms}$ to 200 V$_{rms}$. We also show that it is possible to increase (or decrease) the loss in the same waveguide at different wavelengths. For example, selective wavelength transmission with an extinction ratio of 20 dB/cm is demonstrated.

High contrast gratings

A high contrast grating (HCG) is a grating with a high index contrast between the grating material and its surroundings which operates in the near-wavelength regime. In this regime, the period of the grating is smaller than the wavelength of the incident light but larger than the wavelength inside the grating material. HCGs are studied because of their remarkable reflective properties. For TM polarized (perpendicular to the grating bars) normally incident light, they exhibit broadband ($\frac{\Delta\lambda}{\lambda} = 35$ nm) high reflectivity ($> 99\%$) whereas for TE polarized (parallel to the grating bars) normally incident light, they exhibit sharp high quality resonances typified by a rapid change in reflectivity from 0% to 100% over a narrow range of wavelengths. The most notable application of HCGs is their use as the replacement of distributed Bragg reflectors for the top reflector in VCSELs. They have also been proposed in applications for flat focusing reflectors/lenses and hollow-core waveguides.

The reflective properties of HCGs are completely characterized by their geometry (i.e. period, thickness and duty cycle) and can be explained by taking into account the fact that they are equivalent to sub-wavelength waveguide arrays (SWAs). As such when light is incident on a HCG, SWA modes propagating in a direction parallel to the normal to the HCG are generated. In the near-wavelength regime, there are exactly two SWA modes. Due to the large refractive index jump that exists at the top and bottom interfaces of the HCG, the SWA modes reflect back into the HCG and couple to each other as well. Consequently, there exist Fabry-Perot resonance conditions for both modes. For a HCG with a given geometry both SWA modes attain their Fabry-Perot (FP) resonance condition simultaneously. For TM polarized incident light, broadband reflection corresponds to when there is π phase difference i.e. destructive interference between both SWA modes (at their FP resonance condition) at the output plane of the HCG. Since the near-wavelength character of the HCG prevents diffraction into higher diffraction orders, all the light is reflected. On the other hand, TE polarized high quality resonances correspond to constructive interference of the SWA modes (at their FP resonance condition). This leads to a buildup of the field inside the HCG. This buildup is responsible for the sharp transition from from 0% to 100% over a narrow range of wavelengths.

Air-clad HCGs working for TE and TM polarized light have equal potential for tuning. However, it easier to measure a shift in a narrow band of wavelengths. Additionally, LC molecules typically tend to align parallel to parallel to longitudinal structures like the high index bars of a HCG. Consequently, in my research, I focus on tuning the reflection of LC-clad HCGs working in the wavelength range 1500nm t0 1700nm for TE polarized normally incident light. I use an LC solver and a finite element based frequency domain solver to simulate the reflectivity of various LC-clad HCGs. Using some basic design rules and taking into account constraints imposed by the type of chips available, I design five HCGs with slightly different parameters (i.e. period, thickness and duty cycle). Following this, I fabricate LC cells in which the bottom plate is a silicon chip (with the HCGs) and a glass plate is the top plate. Both plates are held together by UV curable glue. Spacer balls mixed with the glue determine the cell gap. The cell is filled with LC by capillary action. The glass plate has a conductive indium tin oxide (ITO) layer and a nylon alignment layer. The ITO and the bottom part (silicon substrate) of the chip have electrical contacts for applying a voltage over the LC. The nylon alignment layer ensures the LC director has an appropriate orientation. The orientation of the LC above the HCGs is checked with a polarization microscope. The LC are found to be parallel with the high index bars of the HCGs. When a voltage is applied to the cell, the LCs reorient so that the director makes an angle with the normal to the HCG surface. As the voltage is increased further, the angle the director makes with the normal to the HCG surface reduces.

Simulations show that the LC-clad HCGs we design have broader TE high quality resonance peaks compared to the air-clad case. The HCGs I fabricate have dimensions of 50 μm by 50 μm. Due to their small size, and the wavelength range within which they work, it is necessary to build a setup in which we can image (with visible light) and illuminate (with infrared light, $\lambda = 1500$ nm to 1700 nm) the HCGs. Using this setup, I perform measurements of the reflected intensity of the HCGs as a function of the applied voltage at fixed wavelengths. These measurements confirm that the reflection of the LC-clad HCGs is voltage dependent. I also perform measurements of the reflected intensity of the LC-clad HCGs as a function of the wavelength for fixed applied voltages. These measurements also indicate that the reflection of the HCGs is wavelength dependent.

Deep-etched waveguides

Deep-etched waveguides are simple types of waveguides which are formed when the active silicon layer on a silicon-on-insulator chip is completely etched away leaving only a strip of silicon with a narrow (less than 1 μm) width on the buried oxide layer. Their compact size makes them suitable high density integration. Due to the geometry and high index contrast of the waveguide, and similarly to shallow-etched waveguides, deep-etched waveguides support TE and TM waveguide modes. I intend to design voltage tunable optical switches by integrating deep-etched waveguides with LC. For the TE mode, the electric field is strongly confined in the waveguide core. Its tuning range is small. The strongest component of the electric field is the lateral (perpendicular to the side walls of the waveguide) component. The longitudinal component (parallel to the waveguide) is also considerable. Consequently, tuning the TE mode is achieved by first orienting the LC in the lateral direction and reorienting it so that it becomes oriented along the longitudinal direction. The TM mode is not as strongly confined to the waveguide core as the TE mode. Accordingly, the tuning range of the TM mode is larger than that of the TE mode. The strongest component of the electric field is the vertical (perpendicular to the top surface of the waveguide) component. The lateral and longitudinal components are also considerable. The tuning of the TM mode can be achieved by orienting the LC along either the lateral or longitudinal direction and reorienting it so that it becomes oriented along the vertical direction. However, in practical situations the tuning by reorientation from the longitudinal to the vertical direction is more feasible. This is a result of the fact that LC prefers to be oriented parallel to the waveguides.

The design proceeds as follows; the LC solver is used to calculate the director orientation over the deep-etched waveguide. The output of the LC calculation is used in the mode solver to compute the effective index of the waveguide mode. This is done for waveguides with different widths, for several applied voltages. For each type of mode, the appropriate type of LC cladding is used. The simulations show that the effective indices of the TE and TM modes in the deep-etched waveguide can be tuned, with the tuning range of the latter being larger than that of the former. Moreover, for sufficiently narrow waveguides, a voltage-controlled cutt-off for the fundamental TE and TM modes is demonstrated.

1
Introduction

1.1 Light

> And God said, ”Let there be light” and there was light.
>
> Genesis 1:3, The Bible

Man has been fascinated by light for time immemorial. In the biblical story of creation, God created light early on during the first day of creation; right after the earth and the heavens. From the discovery of fire, the light bulb and more recently the laser; our society has used light for increasingly diverse applications. In recognition of the fact that technologies concerned with the generation, transmission and detection of light permeate all aspects of our lives today and are set to do so for decades to come, the United Nations 68th general assembly proclaimed the year 2015 the International Year of Light and Light-based Technologies (IYL2015) [1]. These technologies are commonly referred to as photonics. Photonics covers a broad range of applications like laser machining, lighting, spectroscopy, holography, medical diagnosis and therapy, CD/DVD/Blu Ray technology, solar energy generation, optical sensors, display technology, metrology, military technology and optical telecommunications. From this list, we can single out display technology and optical telecommunications as those which arguably have had an overarching impact on society. This is mainly due to the fact that we come in contact with them everyday. Typical examples are the internet, flat panel TVs and displays, smart phones, tablets etc. Since the commercialization of the first consumer product with a liquid crystal display (LCD) (a pocket calculator with an LCD display by Sharp in 1973), LCD technology has improved steadily and has dominated display technology since the late 1990s. LCD technology is the main driver behind today’s billion dollar display industry (see figure 1.1). LCDs main advantages are their small thickness and low power consumption. Similarly, optical telecommunications currently dominate the global long-haul telecommunications market. It is the driving force behind the internet. Short distance communication and chip-level signal processing is currently dominated by electronics. In contrast, the increasing demand for low-cost, high-speed connectivity everywhere (from the network level to the intra-system level) has forced engineers to continually find ways to pack large quantities of transistors and related circuitry into chips. However, transmitting electrical signals over copper wire traces on a chip containing millions of transistors has several drawbacks. These include heat buildup, current leakage and crosstalk between adjacent wire traces. Because of these drawbacks, today's data centers require extensive cooling facilities [2]. Silicon photonics promises to resolve these problems by replacing copper interconnects with optical interconnects made out of silicon. In recent years, silicon photonics has established itself as a platform for high-speed signal processing at a reduced cost. The silicon photonics market has witnessed sustained growth (see figure 1.2). This growth is a consequence of the fact that silicon photonics is compatible with current CMOS fabrication methodologies i.e. it is cheap. This thesis is concerned with the synergies and new opportunities which arise as a result of combining LCD and silicon photonics technologies. In order to achieve this, it is necessary to start with the fundamental building blocks of each technology and integrate them to obtain low-cost high-speed tunable components for applications such as reconfigurable optical switches and interconnects, tunable optical filters, optical phase shifters and modulators etc.

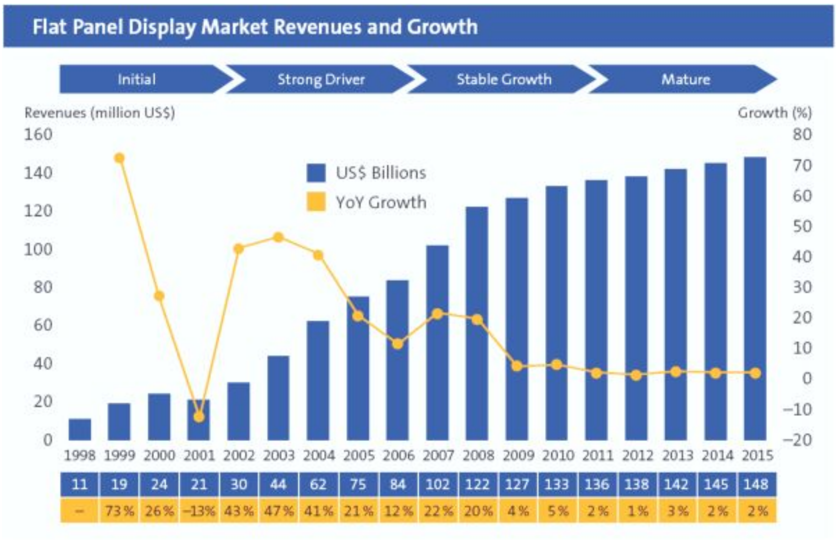

Figure 1.1: Flat panel display revenue and growth. Source: German Flat Panel Display Forum [3]

1.1.1 This PhD

Silicon photonics owes its tremendous success to the unique properties of the silicon-on-insulator material platform. The platform possesses a high index contrast, consequently devices with tight bends are feasible and high density integration is possible. It is also compatible with complementary metal oxide semiconductor (CMOS) fabrication

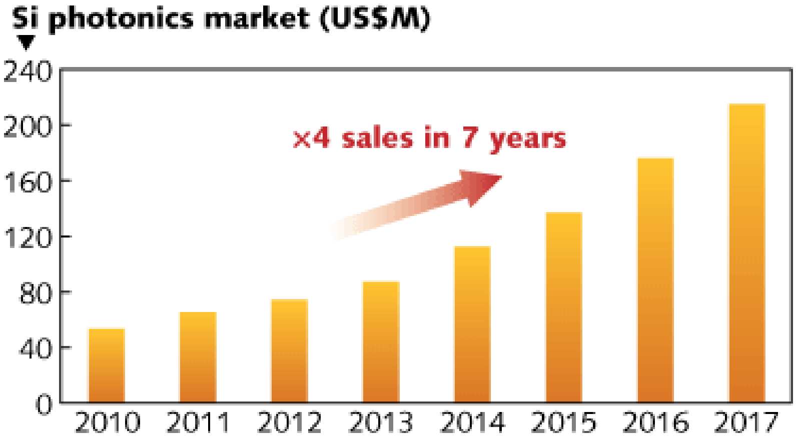

Figure 1.2: Forecast of the silicon photonics market growth. Source: LaserFocusWorld [4]

processes used to fabricate electronic integrated circuits. This makes the technology low-cost. Unfortunately, silicon has a centro-symmetric crystal structure and hence no electro-optic (Pockels) effect. It is possible to use the second order electro-optic effect of silicon. However, this is seldom used because it results in free carrier generation. Consequently, the only other route towards high-speed signal modulation and switching for silicon photonics has been integration with resistive heaters [5–8] for thermo-optic control. However, thermo-optic tuning has some disadvantages. It is slow, has a limited tuning range and most importantly it requires a constant power supply.

On the other hand, liquid crystals are very interesting materials whose large electro-optic effect has made them indispensable to display technology. In addition to their use in displays, liquid crystals are also used in non-display applications. These include spatial light modulators [9], liquid crystal lasers [10], soliton generation [11, 12] and liquid crystal filters and switches [13, 14]. In this work the idea is to have a liquid crystal upper cladding on a number of conventional silicon photonic components. In this way we can achieve low-power electro-optic tuning of the functionality of the silicon photonic components by applying a moderate voltage over the liquid crystal cladding. The achievable tuning range should be wide given the large electro-optic effect of liquid crystals.

There have been previous reports on the tuning of the fundamental building blocks of complex silicon photonic systems. Examples include tuning of silicon ring resonators [15–17], and silicon photonic crystals [18, 19]. Desmet et al [20] report on the tuning of a 3μm wide silicon waveguide using liquid crystals. This PhD is focused on the tuning of the functionalities of fundamental silicon photonic components like shallow-etched, deep-etched and slot waveguides and high contrast gratings. We start with numerical analysis of each of the components. This results in various designs suitable for tunable operation. Next, we perform fabrication and processing using appropriate materials in a clean room environment in order to obtain liquid crystal clad silicon photonic components whose parameters closely match the designs produced earlier. The fabricated components are experimentally characterized using state of the art characterization facilities. The experimentally acquired data is compared with data generated from the design phase in order to ensure the devices operate according to specifications. Finally, factors affecting the optimal operation of each of the components in practical situations are investigated.

1.1.2 Overview of the chapters

The remainder of this introductory chapter gives a more in depth introduction to liquid crystals (the material behind LCDs) and silicon photonics. The rest of this book is arranged as follows. Chapter 2 presents a treatment of the tunability of shallow-etched waveguides. The mechanism for leakage loss in these waveguides is revisited and extended for the case where the waveguide has a liquid crystal cladding. The simulation tools used in modeling the shallow-etched waveguides are introduced. Following this, the steps involved in fabricating the LC-clad shallow-etched waveguides are outlined. Experimental leakage loss measurements of liquid crystal clad waveguides are also presented. Later in the chapter, the experimental results obtained can be explained using the mechanisms developed earlier in the chapter. Several factors affecting the functionality of the experimental device are also discussed. Chapter 3 discusses the possibility of realizing voltage controlled optical switches by integrating liquid crystals with deep-etched waveguides. Chapter 4 reports on the realization of an on-chip state of the art phase shifter based on slot waveguides in silicon-on-insulator. The design, fabrication and characterization of the phase-shifter are explained. A phase shifter with a record voltage-length product is demonstrated. Chapter 5 is devoted to studying the tunability of high contrast gratings (HCGs). It starts with some background about diffraction gratings in general and provides detailed explanations about how HCGs work. It also includes details about the simulation and fabrication of liquid crystal clad HCGs. It closes with experimental measurements of the reflectivity of liquid crystal clad HCGs and discusses factors affecting the operation of the experimental device. Chapter 6 is the final chapter of this book. It gives a summary of all the work done during my PhD, emphasizing the key achievements. It also gives an outlook and perspectives for future work.

1.2 Liquid crystals

In this section, we introduce liquid crystals and proceed to explore the properties which make them indispensable for the investigations carried out in this thesis. A single section in a chapter of a PhD can hardly provide an exhaustive discussion on liquid crystals. The interested reader is referred to the wikipedia entry on liquid crystals [21] as well as classic books on liquid crystals like [22, 23]. This section is largely based on these sources. Liquid crystals (LCs) are very interesting materials with remarkable properties. They are sometimes referred to as the fourth state of matter. They can flow like liquids and at the same time, their molecules exhibit order similar to the crystal structure of solids. These molecules are typically organic molecules with an anisotropic geometry e.g. rod-like, disc-like, banana-shaped etc. They were discovered by the Austrian scientist Friedrich Reinitzer in 1888. There exist two main types of LCs; lyotropic and thermotropic LCs. Lyotropic LCs are materials in which molecules dissolved in a solvent exhibit ordered arrangements. On the other hand, thermotropic LCs have molecules which exhibit order within a well defined temperature range. At higher temperatures, the molecules are organized randomly; we obtain an isotropic liquid. At lower temperatures, the molecules are well ordered and we have a solid. The temperature at which the LC transitions into an isotropic liquid is called the clearing temperature (T_c). Below this temperature, the LC is a cloudy liquid. Above T_c, it is a clear colorless liquid. This unique property led to the first practical use of LCs in the 70s. Two decades later, these amazing materials became central to the display industry. They have since found applications outside the display industry as modulators [24, 25], tunable lenses [26–28], smart materials e.g. polymer dispersed LCs (PDLCs) [29, 30], and are increasingly integrated with other materials [31, 32]. This latter application is the main theme of this thesis.

1.2.1 Thermotropic liquid crystals

As mentioned earlier, thermotropic LCs only exhibit liquid crystalline behavior within a given temperature range. They are often made up of elongated or rod-like molecules. At high temperatures, they from isotropic liquids; thermal motion is high, and the orientation of the molecules is random. At lower temperatures, they become LCs; thermal motion can be overcome by the interaction between the LC molecules. Some measure of ordering in either the position or orientation of the LC can then be achieved. Many thermotropic LCs may exhibit a variety of phases (smectic, nematic) as the temperature is increased. We will briefly discuss each of these phases.

1.2.1.1 Nematic liquid crystals

Nematic LCs are one of the most common LC phases. Their name derives from the Greek word for thread (nema). They are named in this way because of the thread-like topological defects (disinclinations) which characterize this LC phase. In a nematic LC, the rod-like molecules of the LC have no positional order, but they exhibit a long range orientational order. The molecules are on average oriented in the same direction, pointing along the director ($\vec{L}$) as shown in fig.1.3. The nematic LC phase is uniaxial i.e. the phase has one long (preferred) axis, with the other two axes being equivalent. Finally, nematics possess a fluidity similar to that of isotropic liquids and they can be aligned by a properly treated surface, electric field or magnetic field. These make nematics very attractive for applications requiring a wide tuning of optical properties by means of an applied electric field like LCDs. In this thesis, these very attractive features of nematics are harnessed to tune various SOI nanophotonic components.

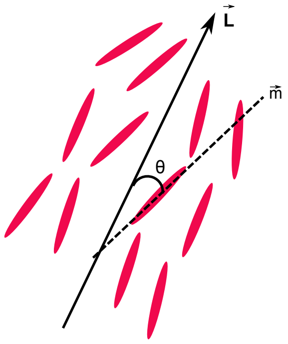

Figure 1.3: The nematic LC phase. The molecules have random positions but they are oriented along the director ($\vec{L}$). The long axis ($\vec{m}$) of the individual molecules can make an angle θ with the director ($\vec{L}$).

1.2.1.2 Smectic liquid crystals

The smectic phase of LCs usually occurs at temperatures lower than the nematic phase. In this phase, one dimensional positional order exists in addition to the long range order. The molecules are arranged in smectic planes. Within these planes the molecules can rotate around the director. In the smectic A phase, the smectic planes are normal to the director. On the other hand, in the smectic C phase the smectic planes are oriented at an angle with respect to the director. Both phases are depicted in fig.1.4.

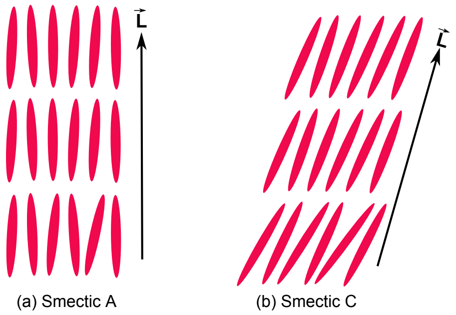

(a) Smectic A (b) Smectic C

Figure 1.4: The smectic LC phase. (a) Smectic A phase, smectic planes are normal to the director. (b) Smectic C phase, smectic planes are at an angle to the director.

1.2.2 Various properties of nematic liquid crystals

Throughout this PhD, nematic LCs are used. Nematic LCs are widely used in display technology and photonics. The elongated molecules which make up nematic LCs usually consist of two or more aromatic rings connected by a linkage group. Attached to the aromatic rings at each end of the molecule is a terminal group and a side chain. Each of these parts has an influence on the various physical properties of the LC. The aromatic rings provide the molecular interaction which gives rise to the nematic phase at low temperatures. The linkage group ensures the LC is stable e.g. when it is illuminated by UV light. The dielectric constant and anisotropy (at low frequency) of the LC derive from the terminal group and its dipole moment. Finally, the elastic properties and the clearing temperature (T_c) of the LC are linked with the composition of the side chain. In fig.1.5 a diagram of the general structure of a nematic LC and the chemical structure of the constituents of the commercially available LC E7 [33] are shown.

In what follows, a brief review of the main physical properties of nematic LCs is given. These characteristics are the order parameter, the dielectric and optical anisotropy, the elastic properties, alignment on a surface, behavior in external electric fields, and the Fréederickz transition.

1.2.2.1 Order parameter

As its name implies, the order parameter (S) gives a measure of the degree of order in a LC. S also gives a measure of how strong the molecular interactions of the LC molecules are compared to their thermal or Brownian motion. It is expressed in (1.1). In the equation θ is the angle between

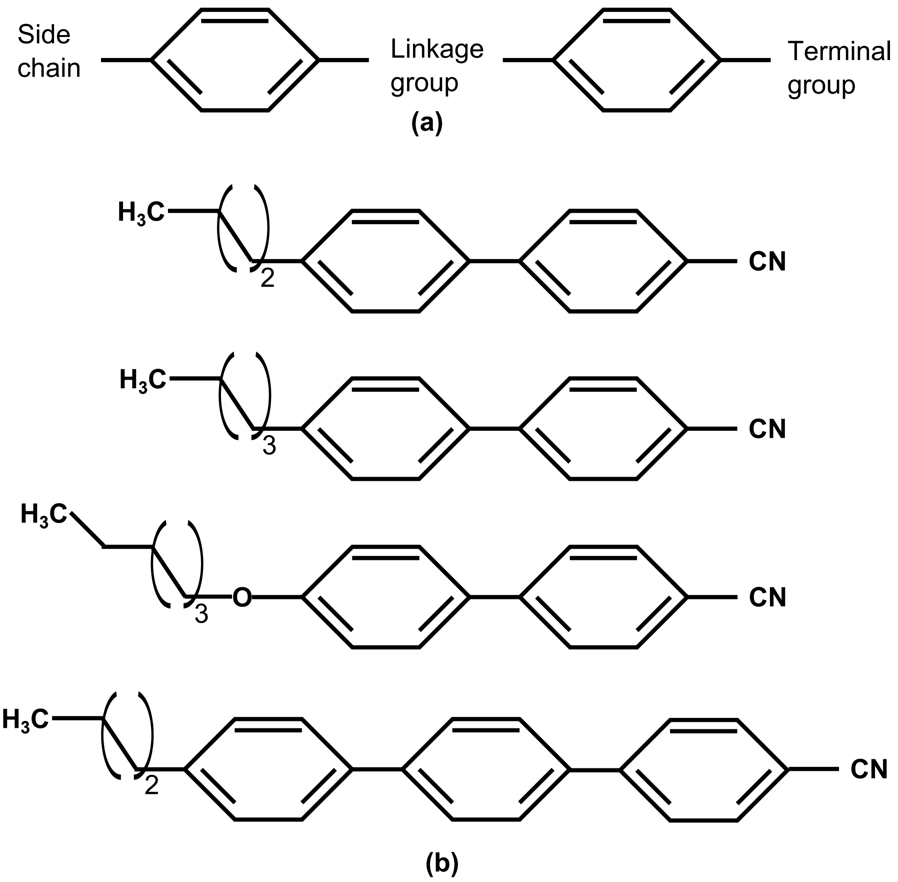

Figure 1.5: General structure of a nematic LC. Composition of the LC blend E7 (1 cyanoterphenyl and 3 cyanobiophenyl molecules).

the director ($\vec{L}$) and the long axis ($\vec{m}$) of the individual LC molecules. S is then obtained as an average over the whole volume of the LC.

$$S = \frac{1}{2}\left\langle 3(\vec{m}\cdot\vec{L})^2 - 1\right\rangle = \frac{1}{2}\left\langle 3\cos^2\theta - 1\right\rangle \tag{1.1}$$

When the temperature is increased to T_c, the LC undergoes a phase transition and becomes an isotropic liquid. This happens because the thermal energy is so high that it overcomes the inter molecular interactions. It then looses any positional or orientational order; neither the director nor nematic behavior exist. If on the other hand we have a decreasing temperature, at T_c a phase transition occurs and the isotropic liquid becomes a LC. The thermal motion is comparable to the inter molecular interaction. As such the molecules begin to show some order. In the nematic phase and close to T_c, S attains a minimum value. As the temperature is further lowered, the thermal energy decreases further and the inter molecular interactions cause the molecules to further align along the director. S increases with decreasing temperature below T_c and attains a maximum value when the thermal energy in the LC is minimal. In a nematic LC, S typically varies between 0.3 and 0.9.

1.2.2.2 Dielectric and optical anisotropy

Nematic LCs are uniaxial materials, with the axis of symmetry parallel to $\vec{L}$. Consequently, the dielectric constants differ in value along the preferred axis ($\varepsilon_{||}$) and perpendicular to this axis ($\varepsilon_{\perp}$). If the z-axis is chosen to be parallel to $\vec{L}$, the dielectric tensor of a nematic LC can be written as;

$$\bar{\bar{\varepsilon}} = \begin{bmatrix} \varepsilon_{\perp} & 0 & 0 \\ 0 & \varepsilon_{\perp} & 0 \\ 0 & 0 & \varepsilon_{||} \end{bmatrix} \tag{1.2}$$

In a general xyz coordinate system (fig.1.6), where the azimuth and the inclination of the director are ϕ and θ respectively, the dielectric tensor becomes

$$\bar{\bar{\varepsilon}} = \begin{bmatrix} \varepsilon_{\perp} + \Delta\varepsilon\sin^2\theta\cos^2\phi & \Delta\varepsilon\sin^2\theta\sin\phi\cos\phi & \Delta\varepsilon\sin\theta\cos\theta\cos\phi \\ \Delta\varepsilon\sin^2\theta\sin\phi\cos\phi & \epsilon_{\perp} + \Delta\varepsilon\sin^2\theta\sin^2\phi & \Delta\varepsilon\sin\theta\cos\theta\sin\phi \\ \Delta\varepsilon\sin\theta\cos\theta\cos\phi & \Delta\varepsilon\sin\theta\cos\theta\sin\phi & \epsilon_{\perp} + \Delta\varepsilon\cos^2\theta \end{bmatrix} \tag{1.3}$$

With the dielectric anisotropy given by $\Delta\varepsilon = \varepsilon_{||} - \varepsilon_{\perp}$. The sign and magnitude of $\Delta\varepsilon$ determine the electro-optic behavior of a liquid crystal. For liquid crystals with positive dielectric anisotropy ($\varepsilon_{||} > \varepsilon_{\perp}$) (respectively negative dielectric anisotropy ($\varepsilon_{||} < \varepsilon_{\perp}$)), the lowest electrostatic energy configuration is for a director parallel (respectively perpendicular) to an applied electric field.

The dielectric constants $\varepsilon_{||}$ and $\varepsilon_{\perp}$ are actually frequency dependent. This phenomenon is known as dispersion. This frequency dependence can be understood by looking at the various polarization mechanisms which are possible in liquid crystals: orientational, vibrational and electronic. The orientational and electronic polarizability mechanisms are dominant in the radio ($\sim$kHz) and optical ($\sim 10^{11}$kHz) frequency regimes respectively. Accordingly, the dielectric constants at typical applied voltage frequencies and optical frequencies are different. For optical radiation we work with the refractive index. The refractive indices of a LC are given by ;

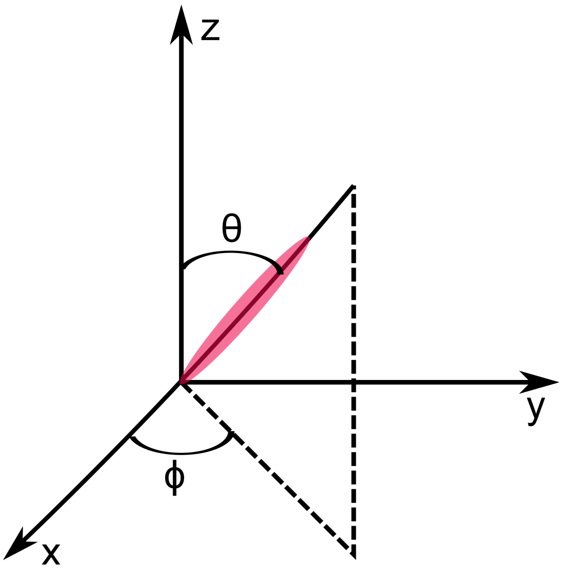

Figure 1.6: xyz coordinate system showing the tilt (θ) and twist (ϕ) angles for an individual LC molecule.

$$n_e = \sqrt{\varepsilon_{\parallel}} \tag{1.4}$$

$$n_o = \sqrt{\varepsilon_{\perp}} \tag{1.5}$$

Where n_e and n_o are the extraordinary and ordinary refractive indices of the LC. For light propagating through a LC, the polarization parallel to the optical axis ($\vec{L}$) feels an index of refraction equal to n_e. Whereas light polarized perpendicular to the optical axis feels an index of refraction equal to n_o.

1.2.2.3 Elastic Energy constants

LCs exhibit elasticity when the director is not uniform. In display or photonic devices containing LCs, a voltage is usually used to reorient the LC molecules in order to obtain a refractive index change for a given polarization. The elastic constants of the LC determine the magnitude of the restoring torque that arises as it reacts to being perturbed from its original configuration. Any static deformation of a LC can be divided into three basic deformations; these are splay, twist and bend deformations (see fig.1.7). In the Oseen-Frank theory, the total free energy (elastic energy) of a LC which is the sum of all energies stored in each of the basic three deformations is written as in (1.6).

$$f_{elastic} = \frac{K_{11}}{2}\|\nabla \cdot \vec{L}\|^2 + \frac{K_{22}}{2}\|\vec{L} \cdot \nabla \times \vec{L}\|^2 + \frac{K_{33}}{2}\|\vec{L} \times \nabla \times \vec{L}\|^2 \tag{1.6}$$

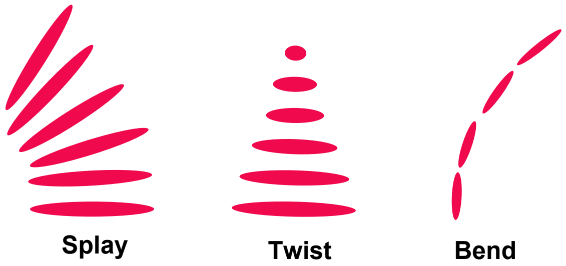

Figure 1.7: The three basic deformations of a liquid crystal associated to the three elastic constants; splay (K_{11}), twist (K_{22}), and bend (K_{33}).

The value of the elastic constants gives an indication of the ease with which the deformation can occur. Typically, the K_{22} constant is the lowest of all three constants, indicating that twist is the most favored elastic deformation.

1.2.2.4 Surface alignment and rubbing

Since nematic LCs consist of rod-like molecules, a uniform director distribution is of paramount importance if a uniaxial optical layer is desired. Nematic liquid crystals are used as tunable uniaxial optical layers in LCDs. The structural and chemical properties of the surfaces of the device have a tremendous influence on the director distribution. Appropriate treatment of the surface can cause the liquid crystal to be well aligned and result in a uniform director distribution. This is usually done by adding a thin alignment layer to a surface. The alignment layer can result in different kinds of director distributions. A thin layer of nylon alignment layer deposited on a surface and rubbed with a piece of cloth will cause the director to be aligned in the rubbing direction with a small initial tilt (pre-tilt) as shown in fig.1.8. Another common method for aligning a liquid crystal is photo-alignment. In this method, a photosensitive layer is deposited on a surface. When the layer is illuminated with polarized UV light, liquid crystal molecules in contact with the surface will be preferentially aligned in a direction perpendicular to that of the polarization of the UV light. A surface can also be treated such that the liquid crystal director is aligned normally to it. This is called homeotropic alignment. An untreated surface will also result in some form of liquid crystal alignment. Usually planar alignment with no preferred direction in the plane is energetically favorable. This gives rise to several small regions with similar director distribution called domains. A liquid crystal layer with domains is unsuitable for typical applications in displays and photonics.The anchoring strength of a surface determines the extent to which deviations from the preferential alignment direction are allowed. When a surface has strong anchoring, the liquid crystal molecules can not reorient at the surface. Whereas a surface with weak anchoring is more favorable for reorientation. When surface anchoring is taken into account, the surface energy can be written as in (1.7).

$$f_{surface} = \frac{K_s}{2}(1 - (\vec{L} \cdot \vec{L}_{pref})) \tag{1.7}$$

K_s being a constant expressed in Jm^{-2}.

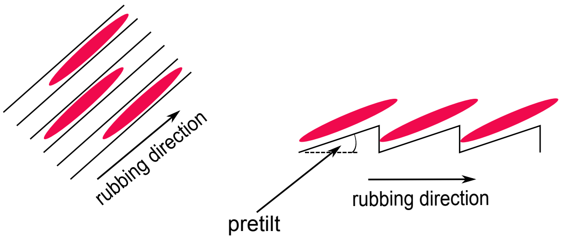

Figure 1.8: Top view of a surface with a rubbed nylon alignment layer. The molecules align in the direction of the rubbing. The side view shows the pre-tilt of the liquid crystal molecules at the surface.

1.2.2.5 Behavior in an external electric field

In an isotropic medium the dielectric displacement ($\vec{D}$) is parallel to the electric field ($\vec{E}$). In an anisotropic medium like a nematic LC, this not true any longer. The electric displacement in a nematic LC can be written as in (1.8).

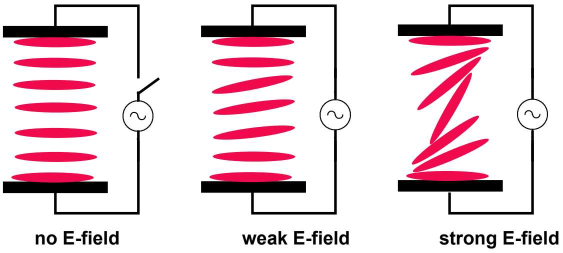

Figure 1.9: Behavior of the LC director for positive dielectric anisotropy in an external electric field. The external electric field will induce a torque on the molecules which causes them to realign parallel to it.

$$\vec{D} = [\varepsilon_{\perp}\vec{E} + \Delta\varepsilon(\vec{E}\cdot\vec{L})\vec{L}] \tag{1.8}$$

When a layer of nematic LC is sandwiched between two electrodes as is the case in practical LC based devices. Since $\vec{D}$ is not parallel to $\vec{E}$, a torque will be exerted on the liquid crystal molecules if an external electric field (generated by a applied voltage over the electrodes) is present. The electric energy density of the nematic liquid crystal can be written as:

$$f_{electric} = -\frac{1}{2}\vec{D}\cdot\vec{E} = -\frac{1}{2}\varepsilon_0[\varepsilon_{\perp}\vec{E} + \Delta\varepsilon(\vec{E}\cdot\vec{L})\vec{L}]\cdot\vec{E} \tag{1.9}$$

The molecules will try to minimize the total energy (elastic + electric). Inspection of (1.9) reveals that for a LC with positive dielectric anisotropy, this minimization can be achieved by realigning the molecules so that they become parallel to the electric field as shown in fig.1.9. For a liquid crystal with negative dielectric anisotropy, the molecules realign perpendicular to the electric field.

The reorientation of the nematic LC director in response to an applied voltage only occurs if the applied voltage is greater than a certain threshold voltage. Below this threshold voltage, the electric energy can not compensate for the increase in elastic energy which accompanies a reorientation of the molecules in response to the applied voltage. At this voltage, an elastic deformation occurs in the LC layer. This is the so-called Fréederickz transition. The value of the threshold voltage is typically equal to a few volt and depends on the boundary conditions (homeotropic or planar alignment), the elastic constants and dielectric anisotropy of the LC.

1.2.3 Optical properties

Given its uniaxiality, it is immediately obvious that light propagation in a liquid crystalline medium is more complex than in an isotropic medium. LC-based devices typically function by modifying the polarization of the light propagating through them. Accordingly, a brief review of the concept of polarization of light beams is in order.

Light beams are electromagnetic waves propagating in a medium. Light is therefore represented by its electric field vector. This vector is a function of the spatial dimensions and time. In an isotropic medium, the electric field is always perpendicular to the direction of propagation. Consider a monochromatic plane wave propagating along the z-axis in an isotropic medium. Its electric field components can be written as:

$$E_x(z,t) = A_x \cos(\omega t - kz + \phi_x) \tag{1.10}$$

$$E_y(z,t) = A_y \cos(\omega t - kz + \phi_y) \tag{1.11}$$

Where A_x and A_y are real numbers representing the amplitude of the wave, ω is the angular frequency of the light, and $k = n\omega/c = n2\pi/\lambda$ is the wave vector with n being the refractive index of the medium. ϕ_x and ϕ_y represent the phase of each of the components. The polarization state of the light beam is determined by the relative phase ($\phi = \phi_y - \phi_x$) of the two electric field components: three polarization states can be obtained.

- For ϕ =0 or π the electric field vector vibrates in a constant direction in the xy plane. The light is then said to be linearly polarized with the direction of the polarization determined by the ratio of A_x to A_y.
- For $\phi = \pm\frac{\pi}{2}$, and $A_x = A_y$, the tip of the electric field traces a circle in the xy plane. This is called circular polarization.
- When light is neither linearly nor circularly polarized, the tip of the electric field traces an ellipse in the xy plane and the light is said to be elliptically polarized.

The Jones vector representation is used to represent the evolution of polarization in an optical medium. In the Jones vector formalism a plane wave is represented as a column matrix of complex wave amplitudes as in (1.12).

$$\vec{J} = \begin{bmatrix} A_x exp(j\phi_x) \\ A_y exp(j\phi_y) \end{bmatrix} \tag{1.12}$$

In optics, the refractive index of a medium determines the speed at which light propagates in it. In a medium with refractive index n, light has a speed equal to c/n. Furthermore, the refractive index of an isotropic medium can be deduced from the relation $\varepsilon = n^2$. We know from the previous sections that nematic liquid crystals are optically uniaxial with a dielectric and corresponding optical anisotropy. It would seem straightforward to infer that it is characterized by two refractive indices given by $\varepsilon_{\|} = n_{\|}^2$ and $\varepsilon_{\perp} = n_{\perp}^2$. Such a simplistic outlook is however false. In order to get a better understanding of the case of light propagation in a uniaxial medium, it is instructive to start from an equivalent version of two Maxwell's equations for monochromatic fields:

$$\nabla \times \vec{E} = -j\omega\mu_0\vec{H} \tag{1.13}$$

$$\nabla \times \vec{H} = j\omega\varepsilon_0\bar{\bar{\varepsilon}} \cdot \vec{E} \tag{1.14}$$

In order to find the appropriate refractive index of the uniaxial medium, we consider a plane wave propagating through it with electric and magnetic field vectors given by:

$$\vec{E}(\vec{r},t) = \vec{E}exp[j(\omega t - \vec{k} \cdot \vec{r})] \tag{1.15}$$

$$\vec{H}(\vec{r},t) = \vec{H}exp[j(\omega t - \vec{k} \cdot \vec{r})] \tag{1.16}$$

By substituting (1.15) and (1.16) into (1.13) and (1.14) and eliminating $\vec{H}$ we obtain:

$$\vec{k} \times (\vec{k} \times \vec{E}) + k_0^2\bar{\bar{\varepsilon}} \cdot \vec{E} = 0 \tag{1.17}$$

With $k_0^2 = \omega^2\mu_0\varepsilon_0$ and k_0 is the vacuum wave number. (1.17) is a system of three linear algebraic equations which can be written in matrix form as:

$$\begin{bmatrix} k_0^2\varepsilon_{xx} - k_y^2 - k_z^2 & k_0^2\varepsilon_{xy} + k_xk_y & k_0^2\varepsilon_{xz} + k_xk_z \\ k_0^2\varepsilon_{xy} + k_xk_y & k_0^2\varepsilon_{yy} - k_x^2 - k_z^2 & k_0^2\varepsilon_{yz} + k_yk_z \\ k_0^2\varepsilon_{xz} + k_xk_z & k_0^2\varepsilon_{yz} + k_yk_z & k_0^2\varepsilon_{zz} - k_x^2 - k_y^2 \end{bmatrix} \begin{bmatrix} E_x \\ E_y \\ E_z \end{bmatrix} = 0 \tag{1.18}$$

(1.18) has a non trivial solution if the determinant of the 3 by 3 matrix is identical to zero. For a given propagation direction, this condition yields two solutions for k. With each solution having a different polarization.

Now let us consider the plane wave is propagating along the z-axis and the long axis of the uniaxial medium is confined to the xz plane, making an angle θ with the z-axis. Such a situation is representative of the phenomena which are the subject of this PhD. The calculation of the determinant of the 3 by 3 matrix in (1.18) then yields the following equation for k_z:

$$[(k_0^2\varepsilon_{xx} - k_z^2)k_0^2\varepsilon_{zz} - k_0^4\varepsilon_{xz}^2] \cdot [k_0^2\varepsilon_{yy} - k_z^2] = 0 \tag{1.19}$$

With solutions being:

$$k_z^2 = k_0^2\varepsilon_{yy} \tag{1.20}$$

$$k_z^2 = k_0^2\frac{\varepsilon_{xx}\varepsilon_{zz} - \varepsilon_{xz}^2}{\varepsilon_{zz}} \tag{1.21}$$

1.2.3.1 Ordinary wave

The solution (1.20) corresponds to the ordinary wave. For a uniaxial medium $\varepsilon_{yy} = \varepsilon_\perp = n_\perp^2 = n_o^2$ we have:

$$k_z^o = n_\perp k_0 = n_o k_0 \tag{1.22}$$

$$E^o = \begin{bmatrix} 0 \\ 1 \\ 0 \end{bmatrix} \tag{1.23}$$

The ordinary wave is linearly polarized along the y-axis. It is perpendicular to the plane containing the propagation direction and the long axis. It propagates with a wave number equal to the vacuum wave number scaled by the ordinary refractive index $n_o = n_\perp$

1.2.3.2 Extraordinary wave

The solution (1.21) corresponds to the extraordinary wave. For the case considered here we have $\varepsilon_{xx} = \varepsilon_\perp + \Delta\varepsilon \sin^2\theta$, $\varepsilon_{xz} = \Delta\varepsilon \sin\theta\cos\theta$, and $\varepsilon_{zz} = \varepsilon_\perp + \Delta\varepsilon\cos^2\theta$. Consequently we have the following solutions:

$$k_z^e = k_0\sqrt{\frac{\varepsilon_\perp(\varepsilon_\perp + \Delta\varepsilon)}{\varepsilon_\perp + \Delta\varepsilon\cos^2\theta}} \tag{1.24}$$

$$E^e = \begin{bmatrix} \varepsilon_{zz} \\ 0 \\ -\varepsilon_{xz} \end{bmatrix} \tag{1.25}$$

(1.24) and (1.25) can be rewritten in terms of the refractive indices ($n_\perp$ and $n_\|$) of the uniaxial medium and now read:

$$k_z^e = k_0\sqrt{\frac{1}{(\frac{\sin\theta}{n_\|})^2 + (\frac{\cos\theta}{n_\perp})^2}} \tag{1.26}$$

$$E^e = \begin{bmatrix} n_\perp^2\sin^2\theta + n_\|^2\cos^2\theta \\ 0 \\ -(n_\|^2 - n_\perp^2)\sin\theta\cos\theta \end{bmatrix} \tag{1.27}$$

The extraordinary wave propagates with a wave number determined by $n_\perp$, $n_\|$ and the angle the long axis makes with the z-axis (θ). Its electric field vector is not perpendicular to its direction of propagation. Rather, it lies in the plane containing the long axis and the propagation direction.

1.2.4 The liquid crystal used in this work

Throughout my PhD I worked with the commercially available liquid crystal E7. It is a eutectic mixture of one cyanoterphenyl and three cyanobiophenyl liquid crystal molecules. Its wide nematic range (-10°C to 60.5°C) means it is widely used in research. The physical properties of E7 are summarized in table 1.1.

Ordinary index (n_o)	1.5024
Extraordinary index (n_e)	1.6970
Parallel dielectric constant ($\varepsilon_{\parallel}$)	19.6
Perpendicular dielectric constant ($\varepsilon_{\perp}$)	5.1
Splay elastic constant ($K_{11}(pN)$)	12
Twist elastic constant ($K_{22}(pN)$)	9
Bend elastic constant ($K_{33}(pN)$)	19.5

Table 1.1: Properties of the liquid crystal E7. The refractive indices are given for 1550 nm light.

1.3 Silicon-on-Insulator (SOI) photonics

Silicon photonics has established itself as an enabling technology for future high-speed optical interconnection and data processing [34, 35]. Silicon photonics has been demonstrated to be the most viable option available to the semiconductor industry in its quest to fulfill the trend predicted by Moore's law. According to Moore's law, the number of transistors on a semiconductor chip doubles roughly every 18 months. This increase in number of transistors per unit chip area means increased computing power at a reduced cost. By replacing electrons with photons, silicon photonics would make it possible to increase the speed of data processing and transmission at chip level, thereby preserving Moore's law (albeit without using electronic transistors) and satisfying society's ever increasing demand for computing power and digital storage. The main advantage of silicon photonics is its compatibility with the complementary metal oxide semiconductor (CMOS) fabrication procedures which are currently used for manufacturing electronic chips. In addition to this, the high optical index contrast that exists between the active silicon and buried oxide layers in the SOI architecture provides very strong light confinement, making it possible to obtain efficient sub-micrometer sized light guides with very tight bends. This means several devices can be efficiently and densely integrated on the same chip resulting in lower costs. In this thesis, the focus is on improving and/or extending the capabilities of various silicon photonic components which are the building blocks of future high-speed optical interconnects, switches, tunable filters and modulators. The remainder of this section is devoted to briefly discussing the state of the art for each of the components we study in this PhD.

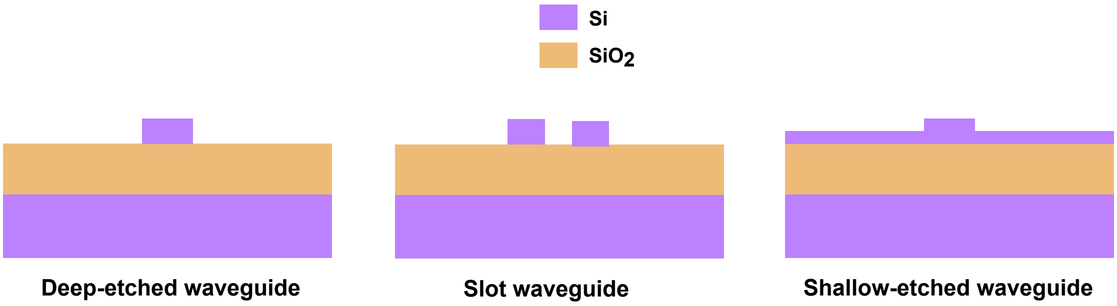

Figure 1.10: Schematic representation of each type of waveguide.

1.3.1 Deep-etched silicon waveguides

Low optical loss and compactness are two essential features of photonic integrated circuits. Deep-etched silicon waveguides are attractive in this respect due to their high index contrast. The high index contrast means these waveguides have high modal confinement. Consequently they have a small form factor e.g. a single mode deep-etched waveguide has a width of 450 nm and a height of 220 nm. In [36–38] the authors report deep-etched waveguides with propagation losses in the range 1 to 2 dB/cm at 1.55 μm. At a waveguide bend, there is an additional loss of 0.03 dB/90° bend (for a bend with 5 μm radius). The propagation loss is mainly due to scattering from the waveguide's slightly rough side walls.

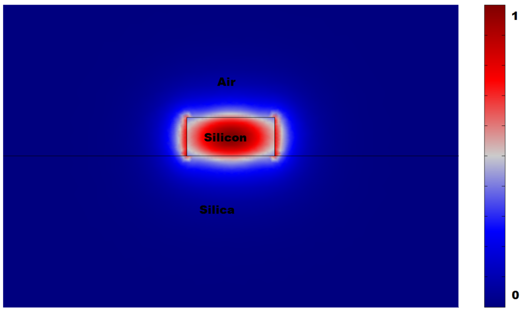

(a) TE mode

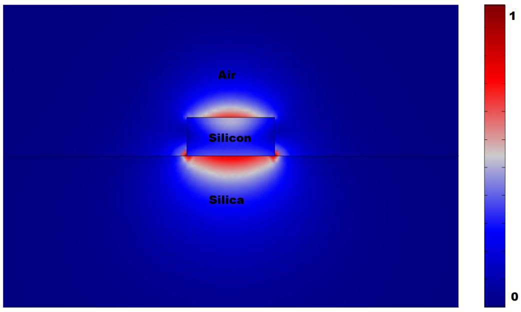

(b) TM mode

Figure 1.11: Mode profiles of the transverse electric (TE) (fig. 1.11(a)) and transverse magnetic (TM) (fig. 1.11(b)) waveguide modes for a deep-etched waveguide.

Figure 1.11 shows the TE and TM modes supported by deep-etched waveguides. Due to the high index contrast between the waveguide's core (silicon, n =3.475 at λ =1.55 μm), cladding (silica, n =1.444 at λ =1.55 μm) and air, the modes are birefringent.

1.3.2 Shallow-etched silicon waveguides

Just like their name implies, this type of waveguide has a shallow-etch of silicon flanking either side of its core as shown in fig.1.10. The shallow-etched part of the waveguide provides lateral light confinement in addition to the vertical confinement due to the index mismatch between air, silicon and silica. Consequently, shallow-etched waveguides have less propagation loss than deep-etched silicon waveguides. Propagation losses of 0.3 dB/cm at 1.55 μm have been reported for shallow-etched waveguides [36, 39]. This makes shallow-etched waveguides suitable for applications where optical signals need to be transmitted over distances of a few tens of centimeters e.g. waveguide routing in optical intra-chip interconnects. Shallow-etched waveguides also offer interesting possibilities for realizing active devices through lateral electrical access like modulators, tunable filters and lasers [40, 41].

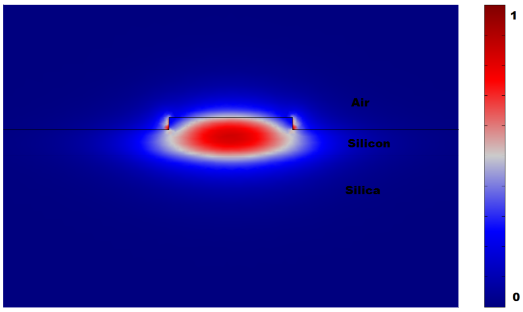

(a) TE mode

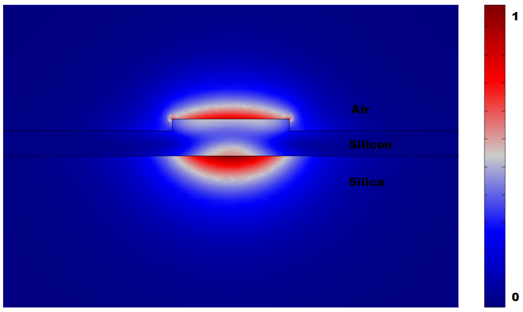

(b) TM mode

Figure 1.12: Mode profile of the quasi transverse electric (TE) and quasi transverse magnetic (TM) shallow-etched waveguide modes. The modes are birefringent

Due to the high index contrast that exists between the waveguide's core and cladding, shallow-etched waveguides support birefringent waveguide modes (see figure 1.12). In applications where shallow-etched waveguides are used, it is usually preferred to excite the TE-like waveguide mode. The TM-like waveguide modes have been shown both theoretically [42, 43] and experimentally [41, 44] to exhibit waveguide-width-dependent lateral leakage loss. This arises because the effective index of the TM-like waveguide mode is comparable to the effective index of the unguided radiating shallow-etched cladding TE mode. Since it is unguided, the radiating TE mode can propagate in any direction. Consequently, there is an angle for which it is phase-matched to the guided TM-like waveguide mode. As such, the guided TM-like waveguide mode suffers from lateral leakage loss for all waveguide widths but that for which satisfies the condition;

$$W = \frac{m\lambda}{\sqrt{{n_{eff,TE}^{(core)}}^2 - {N_{eff,TM}}^2}} \tag{1.28}$$

Waveguide widths which satisfy (1.28) are known as magic widths. At this width, the lateral leakage from both sides of the waveguide cancel out by destructive interference. The origin of (1.28) will be explained later in section 2.2. Accordingly, the lateral leakage loss of the waveguides shows a cyclic pattern with minima in loss corresponding to the magic widths as shown in figure 1.13.

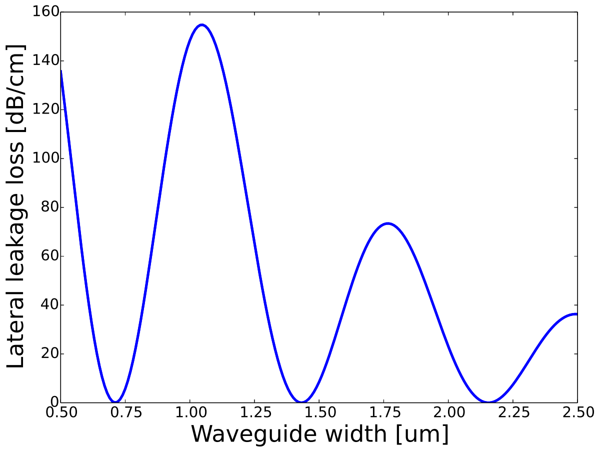

Figure 1.13: Leakage loss of the fundamental TM mode for an air clad waveguide with t_1 =205 nm, t_2 =190 nm at a wavelength of 1550 nm. The loss minima occur at 0.71 μm, 1.43 μm and 2.16 μm.

It has also been shown that shallow-etched bent waveguides and ring resonators also exhibit this leakage loss behavior [45]. In this case, the lateral leakage is dependent on the waveguide bend radius as well as waveguide width. Koshiba et al [46] present a method for reducing the lateral leakage loss in shallow-etched waveguides. They achieve this by incorporating a dimple at the center of the waveguide and arrive a fabrication tolerant design. Given that the lateral leakage loss phenomenon is quite well understood, recent investigations are now geared towards controlling the lateral leakage loss from a shallow-etched waveguide. Dalvand et al [47] proposed a design with two waveguides parallel to each other. When the waveguides are excited with TM polarized light in quadrature phase, the leakage loss from one side can be canceled if the gap between the waveguides is chosen appropriately. On the other hand, in [48] the authors show how the lateral leakage effect can be used to generate highly collimated TE radiation from the transition between a magic width and an anti-magic width waveguide.

1.3.3 Slot silicon waveguides

Despite their strong field confinement, deep-etched and shallow-etched silicon waveguides are limited by two-photon absorption (TPA) and free-carrier absorption (FCA) in all-optical switching applications [49, 50]. On the other hand, there have been tremendous advances in the field of non-linear polymer devices [51] up to speeds of 110 GHz. Consequently, there is interest in combining strongly non-linear materials with silicon waveguides for all-optical signal processing. This is the so-called silicon-organic hybrid approach, whereby the strongly guiding silicon waveguide is covered by the strongly non-linear organic material. However, due to the strong confinement in silicon, the interaction between the non-linear polymer and the waveguide mode is limited. Slot silicon waveguides are a class of waveguides which consist of two deep-etched arms separated by a sub-wavelength low-index slot (See figure 4.1). In a slot waveguide, light is strongly confined in the low-index slot. Applications of high-speed all-optical processing utilizing slot waveguides and non-linear organic polymers have been reported in the literature [49, 52].

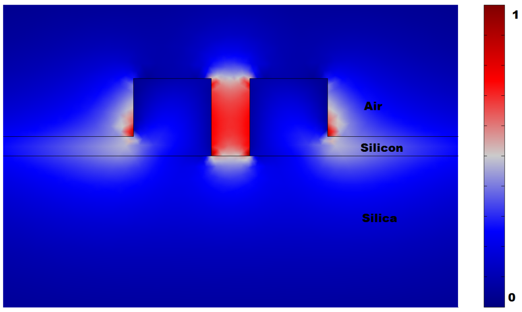

Figure 1.14: Mode profile (E_x component) of a slot waveguide mode. The color bar shows normalized intensity of the electric field.

The unique property of strong confinement in the low-index slot is achieved because Maxwell's equations require the electric field to undergo a large discontinuity at a high-index-contrast interface; with a much higher amplitude on the low-index compared to the high-index side. This unique property also makes slot waveguides suitable for on-chip sensing [53–55].

1.3.4 High contrast gratings

A high contrast grating (HCG) is a grating with high index contrast ($n \sim 2$ to 3.5) between the grating material and its surroundings which operates in the near-wavelength regime. A near wavelength grating is one in which the period is both greater than and smaller than the wavelength of light within the grating material and its surroundings respectively. Fig.1.15 shows a simple schematic of a HCG.

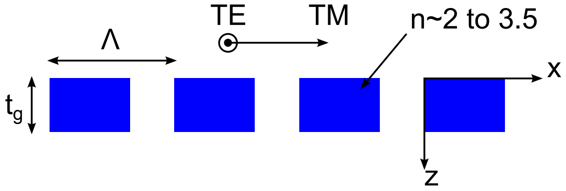

Figure 1.15: Geometry of a HCG in air featuring its period (Λ) and thickness (t_g). The grating fill factor (η) is the percentage of the grating period filled by the high index grating bars.

HCGs are interesting because of their novel reflective properties. For TM polarized (perpendicular to the grating lines), normally incident light and specific geometric dimensions HCGs have an ultra broadband ($\frac{\Delta\lambda}{\lambda} = 35\%$) reflection spectrum with very high ($R > 99\%$) reflectivity. For TE polarized (parallel to the grating lines) light, normal incidence, and given grating parameters, the reflection shows high-quality factor resonances at certain wavelengths. These features make HCGs attractive for applications as ultra thin broadband reflectors for VCSELs (replacement of DBRs) [56–61], high Q resonators [62], resonant polarization sensitive filters [63, 64], planar flat focusing mirrors/lenses [65, 66], and hollow core waveguides [67, 68].

The reflection of an HCG is completely determined by its Λ, t_g and η. A grating with the following parameters; Λ =772 nm, t_g = 502 nm, $\eta = 77\%$ and high index n_b =3.2137 shows a broadband reflection for TM polarized normally incident light. On the other hand, a grating with the following parameters; Λ =716 nm, t_g =1494 nm, $\eta = 70\%$ and n_b =3.48, exhibits high quality resonances for TE polarized normally incident light. The reflection spectra of both gratings are displayed in fig.1.16.

The wide band and sharp reflections for TM and TE polarized normally incident light arise because of the phase selection rules of the grating's geometry. The grating bars form a sub-wavelength waveguide array (SWA) in the z-direction. When light is incident on the HCG, the modes of the SWA are excited. These modes propagate within the HCG and depending on their relative phase, they undergo coupling at the boundaries of the HCG. This model has been shown to account for all the novel features of HCGs [69].

1.4 Conclusion

Light-based technologies play a fundamental role in today's society and are set to do so in future. Liquid crystal displays and optical communications are two fine examples of widespread applications of light-based technology. Due to their ability to undergo a large refractive index change in response to a low applied voltage, liquid crystals have established themselves as the material of choice in the display industry. Following their success in the display industry, liquid crystals are increasingly being used for non-display applications. These applications typically fall within the realm of photonics. On the other hand, in recent years, there has been growing interest in all-optical signal processing, optical interconnects and optical signal processing. These functionalities are investigated because they open up the

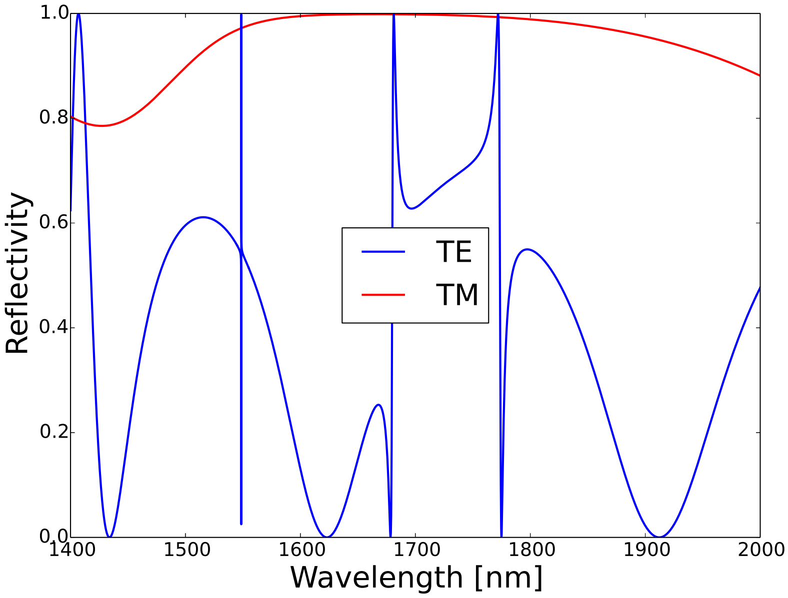

Figure 1.16: Novel reflective properties of HCGs. Red curve: TM polarized broadband reflection ($\Lambda = 772$ nm, $t_g =$502 nm, $\eta = 77\%$, $n_{bar} =$3.2137). Blue curve: TE polarized reflection featuring high Q resonance peaks ($\Lambda =$716 nm, $t_g =$1494 nm, $\eta = 70\%$, $n_{bar} =$3.48). Data taken from [69].

possibility for data transmission and signal processing at a rate which exceeds (by far) the best rate achievable today (electronically). The need for integration with electronics and economies of scale make it very attractive to realize the optical functions mentioned above in silicon. The consequence of this is the emergence of silicon photonics. Silicon photonic chips have been shown to be capable replacements for electronic chips. Allowing for faster data processing and transmission with lower power consumption. However, it is not possible to have active silicon photonics components. This is due to the fact that silicon is a centrosymmetric crystal. Accordingly, it has no Pockets (linear) electro-optic effect. The use of its Kerr (second order) electro-optic effect is hampered by the generation of free carriers. Consequently, in order to achieve active functionalities, it is necessary to integrate silicon photonic devices with other materials which have a large electro-optic effect. Liquid crystals are an excellent example of such a material. They have already been successfully used for tuning silicon photonics crystals and ring resonators. Tunable liquid crystal clad silicon waveguide interconnects, phase shifters and switches and tunable liquid crystal clad high contrast gratings are yet to be investigated. This is the subject of this thesis. In this introductory chapter, the main goal of this thesis is stated. Following this, the reader is introduced to liquid crystals and silicon photonics. The chapter closes with a brief description of the current research for each of the silicon photonic components we study.

Bibliography

[1] *The International Year of Light and Light-based Technologies.* `http://www.light2015.org`. Accessed: 2014-12-12.

[2] *Silicon photonics will revolutionalize data centers in 2015.* `http://www.techrepublic.com/article/silicon-photonics-will-revolutionize-data-centers-in-2015/`. Accessed: 2015-01-29.

[3] *German Flat Panel Display Forum.* `http://www.displayforum.de/market_semenza.htm`. Accessed: 2014-12-12.

[4] *LaserFocusWorld.* `http://www.laserfocusworld.com/articles/2012/09/report-addresses-market-potential-of-silicon-photonics.html`. Accessed: 2014-12-12.

[5] M.W. Pruessner, T.H. Stievater, M.S. Ferraro, and W.S. Rabinovich. *Thermo-Optic Tuning and Switching in Silicon-On-Insulator Waveguide Fabry-Perot Microcavities.* Opt. Express, 15(12):7557–7563, 2007.

[6] Joris Van Campenhout, William M. J. Green, Solomon Assefa, and Yurii A. Vlasov. *Integrated NiSi waveguide heaters for CMOS-compatible silicon thermo-optic devices.* Opt. Lett., 35(7):1013–1015, Apr 2010.

[7] P. Dong, W. Qiang, H. Liang, R. Shafiiha, D. Feng, G. Li, J.E. Cunningham, A.V. Krishnamoorthy, and M. Asghari. *Thermally Tunable Silicon Racetrack Resonators with Ultralow Tuning Power.* Opt. Express, 18(19):20298–20304, 2010.

[8] Adil Masood, Marianna Pantouvaki, Danny Goossens, Guy Lepage, Peter Verheyen, Joris Van Campenhout, Philippe Absil, Dries Van Thourhout, and Wim Bogaerts. *Fabrication and characterization of CMOS-compatible integrated tungsten heaters for thermo-optic tuning in silicon photonics devices.* Opt. Mater. Express, 4(7):1383–1388, Jul 2014.

[9] Jie Sun, Shin-Tson Wu, and Yasuhiro Haseba. *A low voltage submillisecond-response polymer network liquid crystal spatial light modulator.* Applied Physics Letters, 104(2):–, 2014.

[10] Harry Coles and Stephen Morris. *Liquid-crystal lasers.* Nat Photon, 4(10):676–685, 10 2010.

[11] Jeroen Beeckman, Kristiaan Neyts, X. Hutsebaut, C. Cambournac, and M. Haelterman. *Time dependence of soliton formation in planar cells of nematic liquid crystals.* Quantum Electronics, IEEE Journal of, 41(5):735–740, May 2005.

[12] Gaetano Assanto and Mirosław A. Karpierz. *Nematicons: self-localised beams in nematic liquid crystals.* Liquid Crystals, 36(10-11):1161–1172, 2009.

[13] Hui Zhang, Peng Guo, Ping Chen, Shengjiang Chang, and Jinghe Yuan. *Liquid-crystal-filled photonic crystal for terahertz switch and filter*. J. Opt. Soc. Am. B, 26(1):101–106, Jan 2009.

[14] Timothy J. White, Rebecca L. Bricker, Lalgudi V. Natarajan, Vincent P. Tondiglia, Lisa Green, Quan Li, and Timothy J. Bunning. *Electrically switchable, photoaddressable cholesteric liquid crystal reflectors*. Opt. Express, 18(1):173–178, Jan 2010.

[15] Wout De Cort, Jeroen Beeckman, Richard James, F. Anibal Fernández, Roel Baets, and Kristiaan Neyts. *Tuning of silicon-on-insulator ring resonators with liquid crystal cladding using the longitudinal field component*. Opt. Lett., 34(13):2054–2056, Jul 2009.

[16] Wout De Cort, Jeroen Beeckman, Tom Claes, Kristiaan Neyts, and Roel Baets. *Wide tuning of silicon-on-insulator ring resonators with a liquid crystal cladding*. Opt. Lett., 36(19):3876–3878, Oct 2011.

[17] Sofie Lambert, Wout De Cort, Jeroen Beeckman, Kristiaan Neyts, and Roel Baets. *Trimming of silicon-on-insulator ring resonators with a polymerizable liquid crystal cladding*. Opt. Lett., 37(9):1475–1477, May 2012.

[18] Sharon Weiss, Huimin Ouyang, Jidong Zhang, and Philippe Fauchet. *Electrical and thermal modulation of silicon photonic bandgap microcavities containing liquid crystals*. Opt. Express, 13(4):1090–1097, Feb 2005.

[19] S. W. Leonard, J. P. Mondia, H. M. van Driel, O. Toader, S. John, K. Busch, A. Birner, U. Gösele, and V. Lehmann. *Tunable two-dimensional photonic crystals using liquid crystal infiltration*. Phys. Rev. B, 61:R2389–R2392, Jan 2000.

[20] Hans Desmet, Wim Bogaerts, Artur Adamski, Jeroen Beeckman, Kristiaan Neyts, and Roel Baets. *Silicon-on-insulator optical waveguides with liquid crystal cladding for switching and tuning*. volume 3, pages 430 – 431, 2003.

[21] *Entry on liquid crystals on wikipedia*. `https://en.wikipedia.org/wiki/Liquid_crystal`. Accessed: 2015-06-18.

[22] P. de Gennes and J. Prost. *The physics of liquid crystals*. Clarendon press, 1993.

[23] S. Chandrasekhar. *Liquid Crystals*. Cambridge University Press, second edition, 1992. Cambridge Books Online.

[24] *LCOS-SLM (Optical Phase Modulators) from Hamamatsu Photonics*. `http://www.hamamatsu.com/jp/en/4015.html`. Accessed: 2015-01-13.

[25] *Liquid Crystal Light Modulators from JENOPTIK AG*. `http://www.jenoptik.com/en-liquid-crystal-spatial-light-modulators`. Accessed: 2015-01-13.

[26] Andy Y.-G. Fuh, Shih-Wei Ko, Shu-Hao Huang, Yan-Yu Chen, and Tsung-Hsien Lin. *Polarization-independent liquid crystal lens based on axially symmetric photoalignment*. Opt. Express, 19(3):2294–2300, Jan 2011.

[27] Hung-Chun Lin and Yi-Hsin Lin. *An electrically tunable-focusing liquid crystal lens with a low voltage and simple electrodes*. Opt. Express, 20(3):2045–2052, Jan 2012.

[28] Harry E. Milton, Philip B. Morgan, John H. Clamp, and Helen F Gleeson. *Electronic liquid crystal contact lenses for the correction of presbyopia*. Opt. Express, 22(7):8035–8040, Apr 2014.

[29] Daniela Cupelli, Fiore Pasquale Nicoletta, Sabrina Manfredi, Marco Vivacqua, Patrizia Formoso, Giovanni De Filpo, and Giuseppe Chidichimo. *Self-adjusting smart windows based on polymer-dispersed liquid crystals*. Solar Energy Materials and Solar Cells, 93(11):2008 – 2012, 2009.

[30] Elena Ouskova, Luciano De Sio, Rafael Vergara, Timothy J. White, Nelson Tabiryan, and Timothy J. Bunning. *Ultra-fast solid state electro-optical modulator based on liquid crystal polymer and liquid crystal composites*. Applied Physics Letters, 105(23):–, 2014.

[31] I. Dierking, G. Scalia, and P. Morales. *Liquid crystal–carbon nanotube dispersions*. Journal of Applied Physics, 97(4):–, 2005.

[32] Nicolas Puech, Christophe Blanc, Eric Grelet, Camilo Zamora-Ledezma, Maryse Maugey, Cecile Zakri, Eric Anglaret, and Philippe Poulin. *Highly Ordered Carbon Nanotube Nematic Liquid Crystals*. The Journal of Physical Chemistry C, 115(8):3272–3278, 2011.

[33] J. Martz, L. Zuppiroli, and F. Nuesch. *Benzoic and Aliphatic Carboxylic Acid Monomolecular Layers on Oxidized GaAs Surface as a Tool for Two-Dimensional Photonic Crystal Infiltration*. Langmuir, 20(26):11428–11432, 2004.

[34] J.K. Doylend and A.P. Knights. *The evolution of silicon photonics as an enabling technology for optical interconnection*. Laser & Photonics Reviews, 6(4):504–525, 2012.

[35] Andrew Rickman. *The commercialization of silicon photonics*. Nat Photon, 8(8):579–582, August 2014.

[36] Shankar Kumar Selvaraja, Wim Bogaerts, Philippe Absil, Dries Van Thourhout, and Roel Baets. *Record Low-loss Hybrid Rib/Wire Waveguides for Silicon Photonic Circuits*. In Group IV Photonics, 7th International conference, Proceedings, page 3. IEEE, 2010.

[37] W. Bogaerts and S.K. Selvaraja. *Compact Single-Mode Silicon Hybrid Rib/Strip Waveguide With Adiabatic Bends*. Photonics Journal, IEEE, 3(3):422–432, June 2011.

[38] H. Tian, G. Winzer, A. Gajda, K. Petermann, B. Tillack, and L. Zimmermann. *Fabrication of low-loss SOI nano-waveguides including BEOL processes for nonlinear applications*. Journal of the European Optical Society - Rapid publications, 7(0), 2012.

[39] P. Dong, W. Qian, S. Liao, H. Liang, C.C. Kung, N.N. Feng, R. Shafiiha, J. Fong, D. Feng, A.V. krishnamoorthy, and M. Asghari. *Low Loss Shallow-Ridge Silicon Waveguides*. Opt. Express, 18(14):14474–14479, 2010.

[40] M.A. Webster, R.M. Pafchek, G. Sukumaran, and T.L. Koch. *Low-Loss Quasi-Planar Ridge Waveguides Formed on Thin Silicon-On-Insulator*. Appl. Phys. Lett., 87(23), 2005.

[41] M.A. Webster, R.M. Pafchek, A. Mitchell, and T.L. Koch. *Width Dependence of Inherent TM-Mode Lateral Leakage Loss in Silicon-On-Insulator Ridge Waveguides*. IEEE Phot. Tech. Lett., 19(6):429–431, 2007.

[42] K. Kakihara, K. Saitoh, and M. Koshiba. *Generalized simple theory for estimating lateral leakage loss behavior in Silicon-On-Insulator ridge waveguides*. J. Lightwave Tech., 27(23):5492–5499, 2009.

[43] T.G. Nguyen, R.S. Tummidi, T.L. Koch, and A. Mitchell. *Rigorous Modeling of Lateral Leakage Loss in SOI Thin-Ridge Waveguides and Couplers*. Photonics Technology Letters, IEEE, 21(7):486–488, April 2009.

[44] R. Pafchek, R. Tummidi, J. Li, M.A. Webster, E. Chen, and T.L. Koch. *Low-Loss Silicon-On-Insulator Shallow-Ridge TE and TM Waveguides Formed Using Thermal Oxidation*. Appl. Optics, 48(5):958–963, 2009.

[45] T.G. Nguyen, R.S. Tummidi, T.L. Koch, and A. Mitchell. *Lateral Leakage of TM-like Mode in Thin-ridge Silicon-On-Insulator Bent Waveguides and Ring Resonators*. Opt. Express, 18(7), 2010.

[46] M. Koshiba, K. Kakihara, and K. Saitoh. *Reduced Lateral Leakage Losses in TM-Like Modes in Silicon-On-Insulator Ridge Waveguides*. Opt. Lett., 33(17):2008–2010, 2008.

[47] N. Dalvand, T.G. Nguyen, R.S. Tummidi, T.L. Koch, and A. Mitchell. *Thin-ridge Silicon-on-Insulator Waveguides with Directional Control of Lateral Leakage Radiation*. Opt. Express, 19(6):5635–5643, 2011.

[48] N. Dalvand, T.G. Nguyen, T.L. Koch, and A. Mitchell. *Thin Shallow-Ridge Silicon-on-Insulator Waveguide Transitions and Tapers*. Photonics Technology Letters, IEEE, 25(2):163–166, Jan 2013.

[49] KoosC., VorreauP., VallaitisT., DumonP., BogaertsW., BaetsR., EsembesonB., BiaggioI., MichinobuT., DiederichF., FreudeW., and LeutholdJ. *All-optical high-speed signal processing with silicon-organic hybrid slot waveguides*. Nat Photon, 3(4):216–219, 04 2009.

[50] Juerg Leuthold, Wolfgang Freude, J-M Brosi, Roel Baets, Pieter Dumon, Ivan Biaggio, Michelle L Scimeca, Franēois Diederich, Brian Frank, and Christian Koos. *Silicon organic hybrid technology—A platform for practical nonlinear optics*. Proceedings of the IEEE, 97(7):1304–1316, 2009.

[51] Datong Chen, Harold R. Fetterman, Antao Chen, William H. Steier, Larry R. Dalton, Wenshen Wang, and Yongqiang Shi. *Demonstration of 110 GHz electro-optic polymer modulators*. Applied Physics Letters, 70(25):3335–3337, Jun 1997.

[52] C. Koos, L. Jacome, C. Poulton, J. Leuthold, and W. Freude. *Nonlinear silicon-on-insulator waveguides for all-optical signal processing*. Opt. Express, 15(10):5976–5990, May 2007.

[53] Francesco Dell'Olio and Vittorio M. Passaro. *Optical sensing by optimized silicon slot waveguides*. Opt. Express, 15(8):4977–4993, Apr 2007.

[54] Carlos A. Barrios, María José Ba nuls, Victoria González-Pedro, Kristinn B. Gylfason, Benito Sánchez, Amadeu Griol, A. Maquieira, H. Sohlström, M. Holgado, and R. Casquel. *Label-free optical biosensing with slot-waveguides*. Opt. Lett., 33(7):708–710, Apr 2008.

[55] T. Claes, J.G. Molera, K. De Vos, E. Schachtb, R. Baets, and P. Bienstman. *Label-Free Biosensing With a Slot-Waveguide-Based Ring Resonator in Silicon on Insulator*. Photonics Journal, IEEE, 1(3):197–204, Sept 2009.

[56] Michael C.Y. Huang, Y. Zhou, and Connie J. Chang-Hasnain. *A surface-emitting laser incorporating a high-index-contrast subwavelength grating*. Nat Photon, 1(2):119–122, February 2007.

[57] Ye Zhou, M.C.Y. Huang, and C.J. Chang-Hasnain. *Large Fabrication Tolerance for VCSELs Using High-Contrast Grating*. Photonics Technology Letters, IEEE, 20(6):434–436, March 2008.

[58] Michael C. Y. Huang, Ye Zhou, and Connie J. Chang-Hasnain. *Single mode high-contrast subwavelength grating vertical cavity surface emitting lasers*. Applied Physics Letters, 92(17):–, 2008.

[59] C.J. Chang-Hasnain, Ye Zhou, M. Huang, and C. Chase. *High-Contrast Grating VCSELs*. Selected Topics in Quantum Electronics, IEEE Journal of, 15(3):869–878, May 2009.

[60] Christopher Chase, Ye Zhou, and Connie J. Chang-Hasnain. *Size effect of high contrast gratings in VCSELs*. Opt. Express, 17(26):24002–24007, Dec 2009.

[61] Connie J. Chang-Hasnain and Weijian Yang. *High-contrast gratings for integrated optoelectronics*. Adv. Opt. Photon., 4(3):379–440, Sep 2012.

[62] Ye Zhou, Michael Moewe, Johannes Kern, Michael C. Huang, and Connie J. Chang-Hasnain. *Surface-normal emission of a high-Q resonator using a subwavelength high-contrast grating*. Opt. Express, 16(22):17282–17287, Oct 2008.

[63] *Asymmetric direction selective filter elements based on high-contrast gratings*, volume 8633, 2013.

[64] Gaige Zheng, Jiawei Cong, Linhua Xu, and Wei Su. *Compact polarizers with single layer high-index contrast gratings*. Infrared Physics & Technology, 67(0):408 – 412, 2014.

[65] Fanglu Lu, Forrest G. Sedgwick, Vadim Karagodsky, Christopher Chase, and Connie J. Chang-Hasnain. *Planar high-numerical-aperture low-loss focusing reflectors and lenses using subwavelength high contrast gratings*. Opt. Express, 18(12):12606–12614, Jun 2010.

[66] Annett B. Klemm, Daan Stellinga, Emiliano R. Martins, Liam Lewis, Guillaume Huyet, Liam O'Faolain, and Thomas F. Krauss. *Experimental high numerical aperture focusing with high contrast gratings*. Opt. Lett., 38(17):3410–3413, Sep 2013.

[67] Ye Zhou, Vadim Karagodsky, Bala Pesala, Forrest G. Sedgwick, and Connie J. Chang-Hasnain. *A novel ultra-low loss hollow-core waveguide using subwavelength high-contrast gratings*. Opt. Express, 17(3):1508–1517, Feb 2009.

[68] H. Huang, Y. Yue, L. Zhang, C. Chase, D. Parekh, F. Sedgwick, M.C. Wu, C.J. Chang-Hasnain, M. Tur, and A.E. Willner. *Analog Signal Transmission in a High-Contrast-Gratings-Based Hollow-Core-Waveguide*. Lightwave Technology, Journal of, 30(23):3640–3646, Dec 2012.

[69] V. Karagodsky and C.J. Chang-Hasnain. *Physics of near-wavelength high contrast gratings*. Opt. Express, 20(10), 2012.

2

Shallow-etched Silicon Waveguides

2.1 Introduction

As mentioned in the introductory chapter of this book, shallow-etched SOI waveguides [1] offer interesting possibilities for realizing devices with lateral electrical access like modulators and lasers [1, 2]. The waveguides investigated in this thesis are realized on an SOI wafer with a 220 nm thick top silicon layer sitting on a 2 μm thick buried oxide layer. The shallow-etched depth is 70 nm, so the shallow-etched part of the waveguides is 150 nm thick. The high index mismatch between the waveguide core and its cladding results in highly birefringent waveguide modes as shown in fig. 2.1. The fundamental TE-like and TM-like modes of shallow-etched waveguides typically have effective indices (n_{eff}) close to 2.7 and 1.7 respectively. As expected, the E_x and E_y electric field components are the dominant components for TE-like and TM-like modes respectively. However, the field profile of the E_x and E_z components of the TM-like mode have non-zero components far from the center of the waveguide. This is an indication of the fact that as the TM-like mode propagates along the waveguide, it leaks into the lateral slab cladding. Accordingly, the TM-like mode of shallow-etched silicon waveguides are known to exhibit lateral leakage loss.

Due to the lateral leakage loss mentioned above, shallow-etched waveguides are usually only excited with TE polarized light. It has been experimentally and theoretically demonstrated that the lateral leakage loss of the TM-like modes in shallow-etched waveguides is dependent on both the wavelength (of the light in the waveguide) and the waveguide width [2, 3].

---

[1] This chapter is partially based on the following papers:

1. Thomas Ako, Anthony Hope, Jeroen Beeckman, Wim Bogaerts and Kristiaan Neyts, ***Electrically tuneable lateral leakage loss in shallow-etched silicon waveguides.*** OPTICS EXPRESS. Vol. 23. Jan. 2015.
2. Thomas Ako, Jeroen Beeckman, Wim Bogaerts and Kristiaan Neyts, ***Tuning the lateral leakage loss of TM-like modes in shallow-etched waveguides using liquid crystals.*** APPLIED OPTICS. Vol. 53. Jan. 2014.

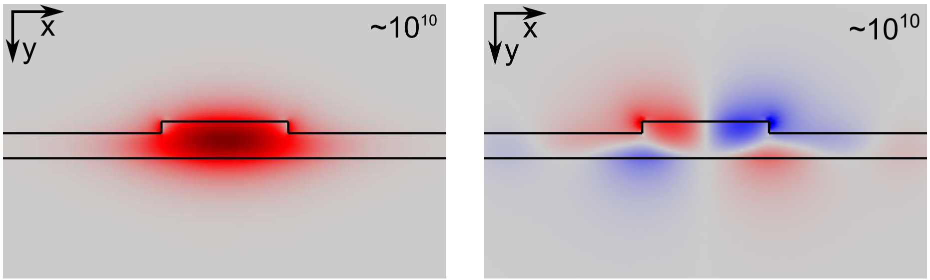

(a) TE mode, x-component of E-field (E_x) (b) TM mode, x-component of E-field (E_x)

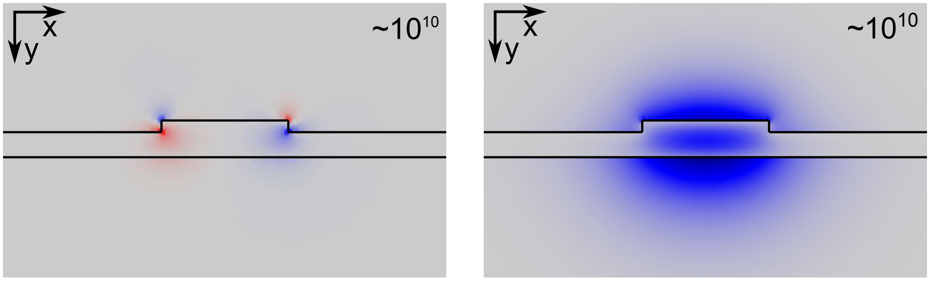

(c) TE mode, y-component of E-field (E_y) (d) TM mode, y-component of E-field (E_y)

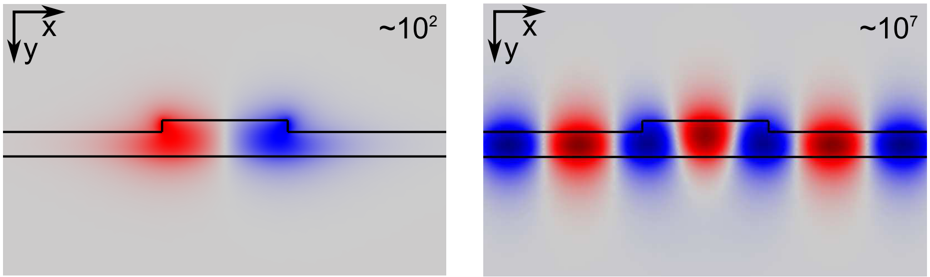

(e) TE mode, z-component of E-field (E_z) (f) TM mode, z-component of E-field (E_z)

Figure 2.1: Field profiles of all three electric field components for the fundamental TE and TM modes of a shallow-etched waveguide. The numbers in the top right corner of each figure indicate the order of magnitude of the fields which have units of Vm^{-1}.

Although this lateral leakage loss phenomenon has been studied extensively [4–9], its applications are still limited. This chapter is devoted to investigating the tunability of the lateral leakage loss phenomenon. This is achieved by integrating conventional shallow-etched waveguides with a LC upper cladding. The optical properties of the LC and hence the leakage properties of the waveguide can be varied by varying the voltage over the LC cladding. Such a scheme opens up the possibility for shallow-etched-waveguide-based tunable filters, switches and interconnects. Additionally, the light lost/radiated from the waveguide can be utilized for applications like on-chip beam forming and polarization control as well as signal routing between parallel unconnected shallow-etched waveguides.

The chapter is arranged as follows. Section 2.2 deals with the mechanism by which lateral leakage loss arises. We revisit the well-known air-clad case and then proceed to the more complicated case of an LC-clad waveguide. Section 2.3 gives details about the numerical tools used to simulate the LC cladding and the shallow-etched waveguides. Here we present an example of a simulation of an LC clad shallow-etched waveguide. In section 2.4 we discuss the design of shallow-etched waveguides with tunable lateral leakage loss. Here we confine ourselves to waveguides with experimentally realizable geometries. Section 2.5 describes the fabrication and processing steps necessary to obtain LC-clad shallow-etched waveguides. Section 2.6 gives a report of the experimentally measured leakage loss for the waveguides designed in section 2.4. Every effort is made here to identify the discrepancies between the design and actual leakage loss values. Section 2.7 explores various issues which affect the tuning performance of the waveguides. Finally, section 2.8 puts the results obtained here into perspective by comparing them with previously reported works.

2.2 Theory of lateral leakage loss

The optical fields in an SOI shallow-etched waveguide are confined in the y-direction by the index mismatch between air, silicon and silica (See fig. 2.2). In the x-direction, confinement is provided by the step discontinuity in silicon.

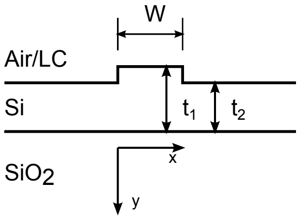

Figure 2.2: Geometry of a shallow-etched SOI waveguide, the positive z-direction is into the plane of the page.

2.2.1 Air-clad shallow-etched waveguide

The TE-like (resp. TM-like) mode has small H_x and E_z (resp. E_x and H_z) components at the waveguide boundaries [10]. Consequently, we have TE-like and TM-like modes in such waveguides; with TE-TM (and TM-TE) mode conversion occurring at the waveguide walls. Mode conversion can lead to lateral leakage loss if certain conditions are satisfied. In each case, we must examine the graph in fig. 2.3 to determine which modes are evanescent in the cladding and hence determine which mode suffers from lateral leakage loss.

For a TE-like propagating shallow-etched waveguide mode, the TE fields must necessarily be laterally evanescent in the waveguide cladding. In general, the effective index of the TM-like mode in a slab waveguide with thickness t_2 is lower than that of the corresponding (same order) TE-like mode for a slab waveguide with thickness t_1. Hence TM fields resulting from TE-TM mode conversion are evanescent. Consequently, the TE-like modes show no lateral leakage loss.

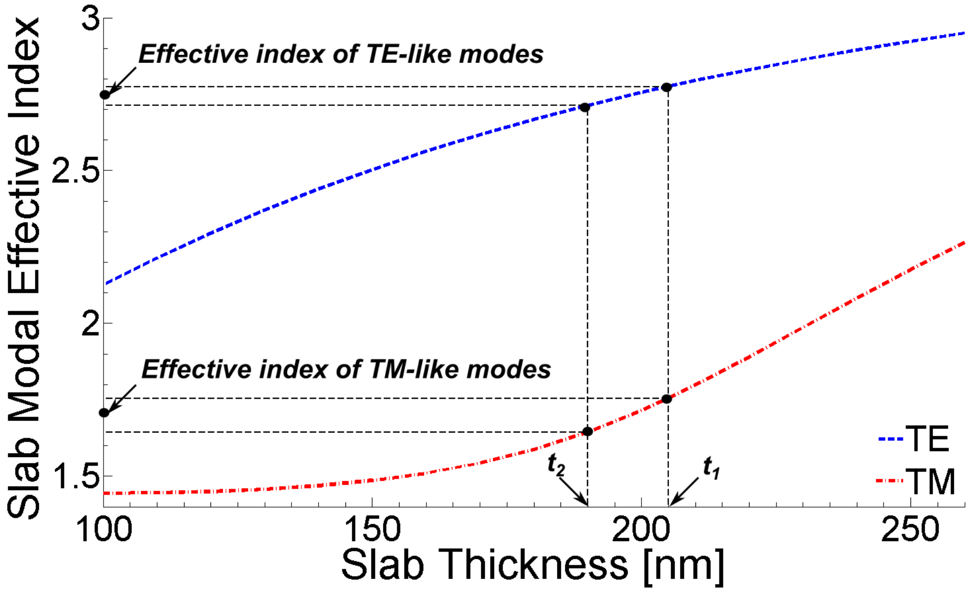

Figure 2.3: Effective index of the fundamental TE and TM modes as a function of slab thickness for an SOI slab waveguide with air upper cladding. t_1 = 205 nm, t_2 = 190 nm and the operating wavelength is 1550 nm.

For a TM-like propagating shallow-etched waveguide mode, the TM field in the cladding must be evanescent as well. However, the propagation constant of the TE mode in a slab waveguide with thickness t_2 is larger than that of the corresponding TM mode for a slab waveguide with thickness t_1. Hence TE fields which arise due to TM-TE conversion at the ridge boundary are not evanescent. These TE fields are not guided in the waveguide; they can propagate away into the side slab of the shallow-etched waveguide in any direction. Moreover they can couple into radiating slab waveguide modes and hence cause light to leak out of the waveguide if they can somehow be matched to a guided mode. Fig. 2.4(a) shows how the guided TM-like mode can be phase matched to a laterally propagating radiating TE slab mode at an angle θ in the lateral slab cladding region [3]. Consequently, the TM-like mode exhibits lateral leakage loss.

Let us consider a TM-like mode propagating in a shallow-etched waveguide. It generates transmitted and reflected TE waves at the right waveguide boundary as described above. The

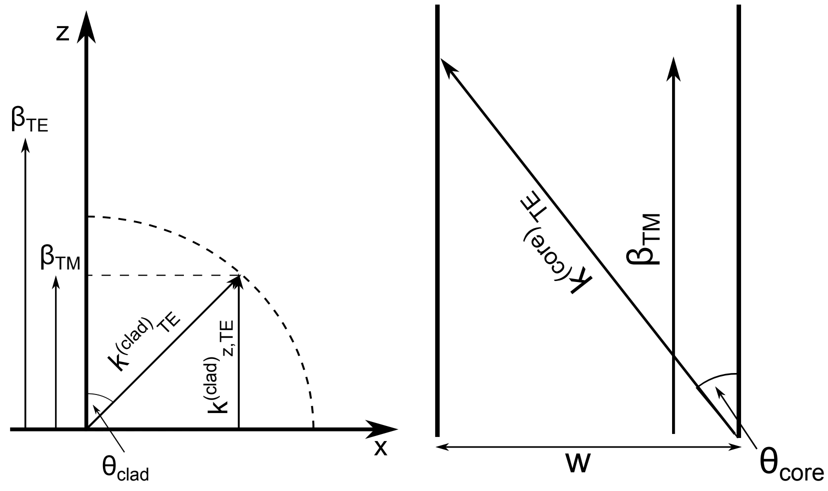

(a) k-vector diagram for air cladding, cladding.

(b) k-vector diagram for air cladding, core

Figure 2.4: k-vector diagrams for an air clad shallow-etched waveguide.

reflected and transmitted TE waves are approximately equal in magnitude and are π radians out of phase. The reflected TE wave is not guided by the waveguide, so it propagates in the core at an angle to the z-axis. The TM-like mode also generates transmitted and reflected TE waves (with a relative phase of π) at the left waveguide boundary. The TE wave which traverses the core of the waveguide combines with the TE wave transmitted at the left waveguide boundary. If the lateral phase shift accumulated by the TE wave as it propagates in the core of the waveguide is equal to an integer multiple of 2π, it will interfere destructively with the transmitted TE wave. The lateral phase shift can be deduced from fig. 2.4(b). The angle the reflected and transmitted TE waves make with the waveguide boundary in the core and cladding respectively are related by Snell's law;

$$n_{eff,TE}^{(core)} \cdot \cos(\theta_{core}) = n_{eff,TE}^{(clad)} \cdot \cos(\theta_{clad}). \tag{2.1}$$

Where $n_{eff,TE}^{(core)}$ is the effective index of the reflected TE wave which is unguided and traverses the waveguide core at an angle to the longitudinal direction. $n_{eff,TE}^{(clad)}$ is the effective index of the transmitted TE wave which radiates away into the slab cladding of the shallow-etched waveguide. The condition for destructive interference of the TE waves can be written as;

$$\kappa_x^{core} \cdot W = 2m\pi. \tag{2.2}$$

Where m is a positive integer and the lateral k-vector is given by (see fig. 2.4);

$$\kappa_x^{(core)} = \sqrt{{\kappa_{TE}^{(core)}}^2 - {\beta_{TM}}^2} \tag{2.3}$$

This indicates that the leakage loss of the TM-like mode is width dependent. Hence, we arrive at the well known expression for the resonance condition of the leakage loss of SOI shallow-etched waveguides [3].

$$W_m = \frac{m\lambda}{\sqrt{{n_{eff,TE}^{(core)}}^2 - {N_{eff,TM}}^2}} \tag{2.4}$$

Where λ is the wavelength of the light in vacuum and $N_{eff,TM}$ is the effective index of the guided TM-like waveguide mode. Consequently, we can infer that the TM mode experiences a significant lateral leakage loss as it propagates along a shallow-etched SOI waveguide except at certain waveguide widths satisfying the resonance condition (2.4). These are the so called magic widths. At these waveguide widths, the TE-like radiating waves generated at the waveguide side walls interfere destructively with each other; resulting in a drastic reduction of the leakage loss.

For a fixed wavelength, the leakage loss of the TM-like mode in a shallow-etched waveguide follows a cyclic pattern; showing minima in leakage loss occurring at equally spaced waveguide widths. The first leakage loss minimum corresponds to $m = 1$, while the second leakage loss minimum corresponds to $m = 2$ and so on. With higher m values corresponding to larger waveguide widths.

2.2.2 LC-clad shallow-etched waveguide

So far, we have discussed the mechanism for leakage loss when a shallow-etched waveguide is air-clad. We now turn our attention to the interesting problem of understanding the leakage loss behavior of such a waveguide when it is covered with LC. Since LCs are uniaxial, we expect more interesting physics [11]. The TE-like and TM-like modes of the shallow-etched waveguide can now feel different refractive indices in the upper cladding. This is equivalent to changing $n_{eff,TE}^{(core)}$ and $N_{eff,TM}$ in (2.4) from the values they had when the waveguide was air-clad. In this case the resonance condition will be satisfied for a waveguide width W_{LC} which will in general be different from W_{air}.

Which index is felt by which mode is determined by the orientation of the LC director in the upper cladding. Using the coordinate system described in fig. 2.2, there are three possibilities for orienting the LC; along the x-axis, y-axis and z-axis respectively. First, when the LC is oriented along the x-axis, the TE-like and TM-like modes feel the extraordinary (n_e) and ordinary (n_o) indices of the LC respectively in the upper cladding. Second, when the LC is oriented along the y-axis, the TE-like and TM-like modes feel an index n_o and n_e respectively in the upper cladding. Finally, when the LC is oriented along the z-axis, the TE-like and TM-like modes both feel an index n_o in the upper cladding. Similarly, the radiating TE slab waveguide mode sees different indices in the upper cladding depending on the direction in which it is propagating. First, when the LC in the cladding is oriented along the x-axis, the radiating TE slab waveguide mode feels an upper cladding index varying from n_o when it is propagating in the x-direction to n_e when it is propagating in the z-direction. When it is propagating in the x-z plane it sees an index $n_x(\alpha)$ given by;

$$n_x(\alpha) = \frac{1}{\sqrt{(\frac{\cos\alpha}{n_o})^2 + (\frac{\sin\alpha}{n_e})^2}} \tag{2.5}$$

Where α is the angle between the direction of propagation of the radiating TE slab waveguide mode and the x-axis. Second, when the LC cladding is oriented along the y-axis, the radiating TE slab waveguide mode feels an upper cladding index equal n_o independent of its direction of propagation. Finally, for LC oriented along the z-axis, the radiating TE slab waveguide mode feels an upper cladding index varying from n_e when it is propagating in the x-direction to n_o when it is propagating in the z-direction. In this case, when it is propagating in the x-z plane it sees an index $n_z(\alpha)$ given in (2.6).

$$n_z(\alpha) = \frac{1}{\sqrt{(\frac{\cos\alpha}{n_e})^2 + (\frac{\sin\alpha}{n_o})^2}} \tag{2.6}$$

Using these intuitive rules, it is possible to sketch the k-vector diagram for each of the upper cladding configurations as shown in fig. 2.5

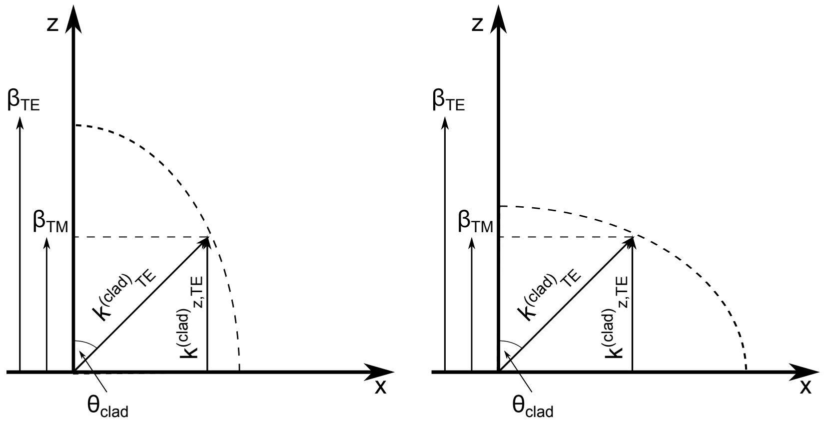

(a) LC oriented along the x-axis (b) LC oriented along the z-axis

Figure 2.5: k-vector diagram for a LC-clad shallow-etched SOI waveguide. The case with LC oriented along the y-axis is not shown since it is identical to fig. 2.4(a) except for a scaling of the respective propagation constants.

A k-vector plot of the case with LC cladding oriented along the y-axis is not shown as it is identical to that in air save for a scaling of the propagation constants due to the higher upper cladding index. In this case the radiating TE slab waveguide mode sees the same index in the upper cladding for all directions, so its tip traces out the quadrant of a circle. The two remaining cases are more interesting. In each case the tip of the radiating slab waveguide propagation vector traces the quadrant of an ellipse. This is a hallmark of the uniaxial nature of the upper cladding. For an air cladding, the radiating slab waveguide mode and the guided TM-like mode can only be phase matched at precisely one angle (θ_{clad}) given by;

$$\cos(\theta_{clad}) = \frac{N_{eff,TM}(W)}{n^{clad}_{eff,TE}} \tag{2.7}$$

When we have a uniaxial cladding, phase matching can now be achieved for a range of angles. With each angle corresponding to a given orientation of the LC in the cladding. By covering the shallow-etched waveguide with LC, we effectively increase the number of achievable magic widths (for a fixed wavelength), with each magic width corresponding to an orientation of the LC in the upper cladding. Conversely, for a shallow-etched waveguide with a fixed width, using an LC upper cladding makes it possible to tune the wavelength of minimum leakage loss (magic wavelength) over a range of wavelengths, with each wavelength within this range corresponding to a given LC orientation. The width of the wavelength range over which the magic wavelength can be tuned is proportional to the optical anisotropy ($\Delta n = n_e - n_o$) of the LC. Since the LC layer can be continuously reoriented by applying an electric field to it, we can obtain an electrically tunable device which is very attractive for the realization of TM polarized tunable photonic integrated circuits.

2.3 Modeling the lateral leakage loss of shallow-etched waveguides

All the devices studied in this thesis are modeled using the finite element method (FEM). The FEM is a numerical technique which is commonly used to obtain approximate solutions to boundary-value problems (BVP). A BVP is usually specified by a differential equation defined over a well defined domain together with boundary conditions on the boundary that encloses the domain [12]. The FEM proceeds by replacing an entire continuous domain with a number of sub-domains (usually called elements) on which the unknown solution is represented using simple interpolation functions with unknown coefficients. In this way, the solution of a problem on a large domain is approximated by a finite number of unknown coefficients. Solving a problem on the whole domain is then replaced with solving a system of algebraic equations obtained by solving the original problem in each sub-domain.

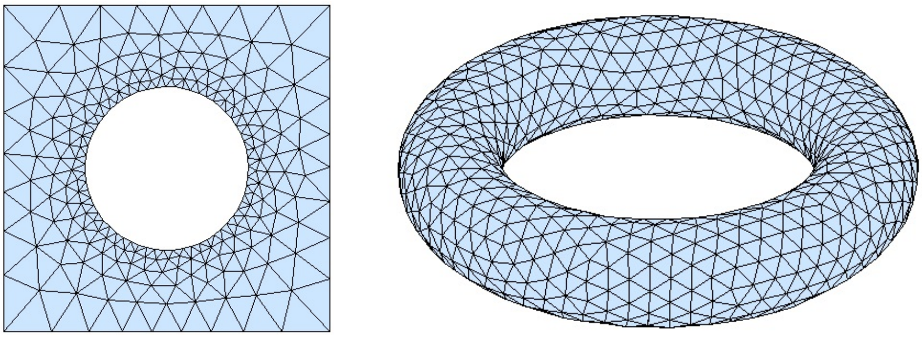
(a) (b)

Figure 2.6: Example of a two-dimensional (a) and three-dimensional (b) mesh using triangular and tetrahedral elements.

The most critical step in the FEM is the meshing of the problem domain. For two dimensional problems, rectangular or triangular (fig. 2.6(a)) mesh elements can be employed. Whereas for three-dimensional problems, rectangular block, triangular prism or tetrahedral (fig. 2.6(b)) mesh elements can be used. Using triangular and tetrahedral mesh elements, it is possible to accurately mesh curved geometries. This is a notable advantage of the FEM over other numerical methods like the finite difference time domain (FDTD) method. It is also important to note that the mesh generation step directly affects the computation time, required memory and accuracy of the final solution. If a very dense mesh is used, then the solution is accurate but memory required to store the mesh data is huge and the computation time is long. On the other hand, for a sparse mesh, the memory requirements and the computation time are small but the solution is rather inaccurate. It is thus necessary to find an optimal mesh density.

2.3.1 LC Simulation

The functionality of shallow-etched waveguides can be adapted by a LC cladding. It is thus important to accurately model the LC orientation (i.e. director) in order to better understand how a LC cladding influences the properties of shallow-etched waveguides. Even for simple one-dimensional geometries, the LC director needs to be obtained numerically. Shallow-etched waveguides have complicated three-dimensional geometries. Since they are longitudinally symmetric, the problem can be reduced to two dimensions. The LC orientation is typically modeled by minimizing the free energy of the LC layer [13].Throughout this thesis, LC behavior is modeled using a finite element based solver [14] developed by the Liquid Crystal Modeling research group at the University College of London. In what follows we briefly outline the basic principles on which the solver is based. The interested reader is referred to the PhD thesis of Richard James [15] for a more thorough treatment of the subject.

The simulation program is based on the Q-tensor ($\bar{\bar{Q}}$) formalism. Within the framework of the Landau-de Gennes theory [16] variable order effects can be taken into account by considering a tensor $\bar{\bar{Q}}$

$$\bar{\bar{Q}} = \frac{S_1}{2}(3\vec{L} \otimes \vec{L} - I) + \frac{S_2}{2}(3\vec{m} \otimes \vec{m} - I) \tag{2.8}$$

where $\otimes$ is the tensor product and I is the identity matrix. $\vec{L}$ is the unit vector along the LC director and $\vec{m}$ is a unit vector perpendicular to the director which accounts for biaxiality. S_1 and S_2 represent the order parameter along $\vec{L}$ and $\vec{m}$ respectively. Even though the Landau-de Gennes theory was originally developed to explain order parameter changes close to the clearing temperature T_c at the nematic-isotropic temperature transition, it can be extended for temperatures ($T < T_c$) within the nematic range. The Landau-de Gennes free energy then contains terms for the bulk energy, elastic energy, electric energy and surface energy. All of which are functions of $\bar{\bar{Q}}$. The elastic energy describes deformations of the LC layer. The electric energy describes the response of the LC layer to an applied electric field. The surface energy describes the conditions enforced at device boundaries through an anchoring strength. The bulk energy describes the phase of the LC layer i.e. isotropic, uniaxial or biaxial. The steady state LC orientation can be obtained by minimizing the Landau-de Gennes total free energy F^S

$$F^S = \iint_{\Omega} (f_{bulk} + f_{elastic} + f_{electric}) d\Omega + \int_{\Gamma} f_{surface} d\Gamma. \tag{2.9}$$

The Q tensor which minimizes the F^S can be obtained by solving the Euler-Lagrange equation:

$$\frac{\partial}{\partial \alpha} \frac{\partial F^S}{\partial \bar{\bar{Q}}, \alpha} - \frac{\partial F^S}{\partial \bar{\bar{Q}}} = 0. \tag{2.10}$$

Where α is an index representing the three coordinate axes x, y and z. $\bar{\bar{Q}}, \alpha$ represents the partial derivative of the Q tensor with respect to α. F^S is supplemented by a dissipation term D in order to calculate the dynamic behavior e.g. switching of the LC in response to an external electric field generated by an applied voltage. This term accounts for the dissipation of the kinetic energy by the viscous forces in the LC. The Q tensor in this case is then given by;

$$\frac{\partial}{\partial \alpha} \frac{\partial F^S}{\partial \bar{\bar{Q}}, \alpha} - \frac{\partial F^S}{\partial \bar{\bar{Q}}} - \frac{\partial D}{\partial \dot{\bar{\bar{Q}}}} = 0. \tag{2.11}$$

Where $\dot{\bar{\bar{Q}}}$ is the time derivative of $\bar{\bar{Q}}$. Once $\bar{\bar{Q}}$ is known, the LC director $\vec{L} = [L_x, L_y, L_z]$ is obtained from its eigenvalues. The optical properties of the LC layer can then be extracted by calculating the dielectric tensor ($\bar{\bar{\varepsilon}}$) at each point in the LC layer.

Several parameters must be input into the LC simulation program; these include geometrical parameters of the device containing the LC, the position of electrodes and their potential, the dielectric properties of the various types of materials included in the device and the alignment layers. Moreover, the geometry of the problem needs to be meshed. All these pre-processing steps are carried out in the commercially available CAD pre- and post-processing software package GID [17]. Using the file output from GID, the LC simulation program calculates the orientation of the LC in the device. The refractive index of the latter is then extracted as explained above. This is used as input for the modeling of LC-clad shallow-etched waveguides.

2.3.2 Simulation of shallow-etched waveguides

Through out this thesis, silicon waveguides are modeled using the commercially available FEM-based mode-solver of COMSOL Multiphysics. COMSOL models are full-vectorial and full-anisotropic i.e. the vector Maxwell's equations are solved while taking into account the full optical anisotropy of the materials concerned. This is especially important as it makes it possible to take the full optical anisotropy of the LC into account. A mesh with triangular vector elements is employed. These mesh elements automatically enforce the continuity of the tangential field components while allowing for discontinuity of the normal field components at boundaries between the materials which make up the waveguide and hence ensure spurious waveguide modes are suppressed. The maximum element size is chosen to be equal to one-tenth of the wavelength. The waveguides are always placed at the center of the simulation domain. The latter is bounded by one-wavelength thick perfectly matched layers (PMLs). Each PML domain has a refractive index identical to that of the material adjacent to it. The PMLs absorb any waves which try to leave the simulation domain and are critical for determining the imaginary part of the effective index and hence leakage loss of the modes. The waveguide modes are described by the fields;

$$\vec{E}(x, y, z, t) = \vec{E}(x, y) e^{j(\omega t - \beta z)} \tag{2.12a}$$

$$\vec{H}(x, y, z, t) = \vec{H}(x, y) e^{j(\omega t - \beta z)} \tag{2.12b}$$

With β the propagation constant of the guided modes. COMSOL formulates the Maxwell's equations into an eigenvalue problem. The eigenvalue solved for is $\Omega = -\delta_z - j\beta$, with δ_z the attenuation constant. In order to simulate a shallow-etched waveguide, we proceed as follows. First, it is necessary to specify the geometry of the waveguide. An example of such a geometry is shown in fig. 2.7. Following this, we specify the refractive index of each of the materials in the geometry.

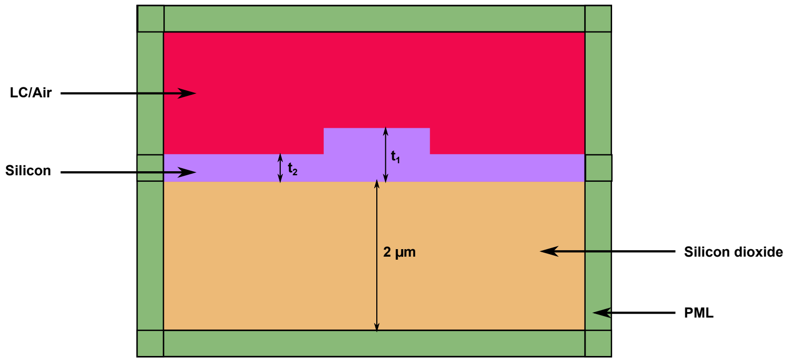

Figure 2.7: Simulation domain used in COMSOL.

The final pieces of information needed to compute the modes supported by the waveguide are the operating wavelength and the desired number of modes. The result is the effective index and field plots of the modes guided by the waveguide at the specified wavelength. The effective index contains the information we need to calculate the leakage loss. The effective index is related to the eigenvalue by;

$$n_{eff} = j \cdot \Omega / k_0. \tag{2.13}$$

With j the unit imaginary number and k_0 the freespace wavenumber. The leakage loss in dB/m is obtained from

$$\Delta_{dB/m} = 20 \cdot \delta_z \cdot \log e. \tag{2.14}$$

The width of the simulation domain has a strong impact on the leakage loss we calculate. Also, it is imperative to keep the computation time to a minimum. Consequently, it is necessary to determine the smallest simulation window width which yields accurate leakage loss results. In [11], such a determination is performed and it is found that for a 12.1μm wide simulation domain, the COMSOL simulations show excellent agreement with previously reported experiments and simulations [3–5, 7].

In order to simulate an LC clad shallow-etched waveguide, we use GID to define a geometry identical to that used in COMSOL. The domain above the waveguide is specified as a LC. The full anisotropy of the LC can be taken into account. The properties of E7 (see table 1.1) are used. The top electrode is in contact with the upper surface of the LC. The lower electrode is the silicon substrate beneath the buried oxide layer, hence we place the bottom electrode below the oxide layer. A sketch of the simulation domain for the LC simulation is shown in fig. 2.8.

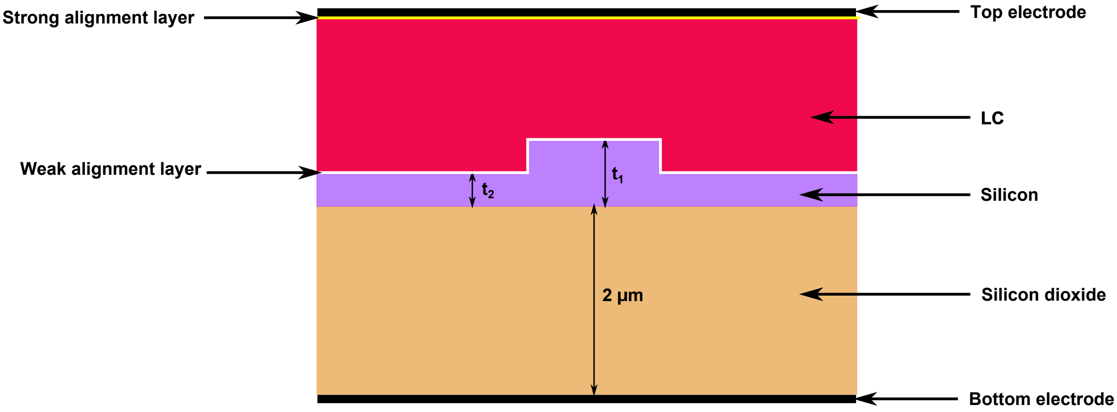

Figure 2.8: Simulation domain used in GID. The figure is not drawn to scale.

2.3.3 Simulation example

Let us now consider an example of a typical shallow-etched waveguide simulation. We simulate the air-clad shallow-etched waveguides proposed in [3]. The waveguides have a core (t_1) and shallow (t_2) thickness of 205nm and 190nm respectively. We start by considering a 710 nm wide waveguide. This is the magic width for this type of shallow-etched waveguide. We define the geometry in COMSOL and find the modes supported by this waveguide at a wavelength of 1550 nm. We find the real part of the refractive index of the fundamental TM mode to be equal to 1.68 with a leakage loss of 0 dB/cm. In order to get the full dependence of the leakage loss on the waveguide width, we vary the width of the waveguide from 0.5 μm to 2.5 μm. The result of this simulation is plotted in fig. 2.9. This is in excellent agreement with the data from [6]. In this paper, the authors demonstrate that FEM simulations of shallow-etched waveguides yield results similar to those obtained with the more accurate mode matching technique. For the LC simulation, we define a geometry identical to the one in COMSOL in GID. We start with the LC oriented parallel to the waveguide and apply a voltage to the electrodes to reorient the LC. The orientation of the LC director for an applied voltage of 0V is shown in fig. 2.10. At this voltage, the LCs are parallel to the waveguide. The TM mode in the waveguide feels an index close to n_o in the upper cladding. The real part of its effective index is 1.93 and its lateral leakage loss is 7.8 dB/cm. As the applied voltage is increased beyond the LC threshold voltage, the LCs reorient and make an angle (tilt) with the normal to the surface of the waveguide. The orientation of the LC for an applied voltage of 100V is shown in fig. 2.11. At this voltage most of the LCs away from the electrodes are reoriented with tilt angles close to 90°. The TM mode of the waveguide feels an index close to n_e in the upper cladding. The real part of its effective index and its lateral leakage loss are now 2.01 and 14.7 dB/cm respectively. We use the simulation tools described in this section to design LC-clad shallow-etched waveguides.

2.4 Design of shallow-etched waveguides with tunable leakage loss

In section 2.2, we explored the effect of the LC upper cladding on the leakage loss of shallow-etched waveguides. In this section we turn our attention to modeling such LC clad waveguides

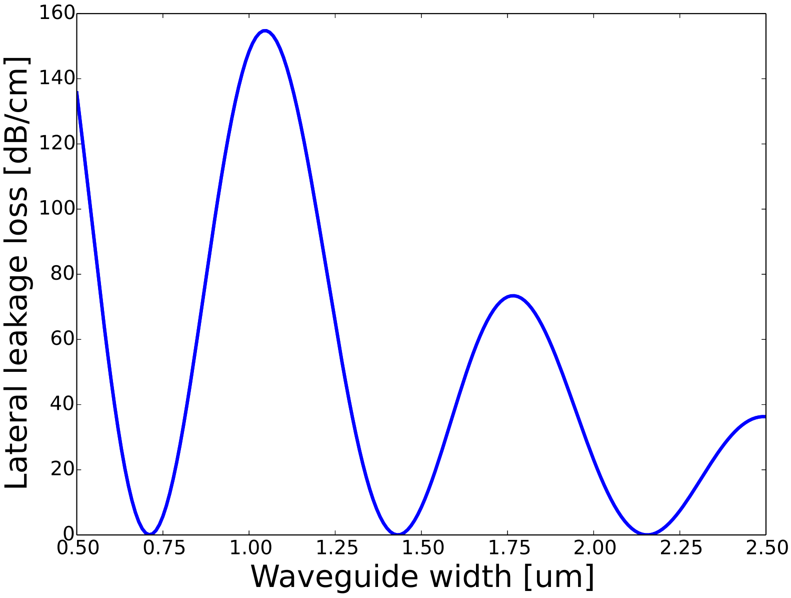

Figure 2.9: Leakage loss of the fundamental TM mode for an air clad waveguide with t_1 =205 nm, t_2 =190 nm at a wavelength of 1550 nm. The loss minima occur at 0.71 μm, 1.43 μm and 2.16 μm.

in order to guide the fabrication of a working device. Tunability will be achieved by switching the LC cladding between two extreme states. In view of implementing a device with a wide lateral leakage loss tuning range, it is desirable to have the LC upper cladding switch between two states for which the TM-like mode in the waveguide feels the smallest (n_o) and largest (n_e) possible refractive index in the upper cladding. For the TM-like mode, E_y is the main E-field component while the E_z component is stronger than the E_x component. Consequently, the TM mode will feel an increase in the cladding index if we start with LC cladding oriented along the x-axis and then reorient it to be along the y-axis. In practice though, a cladding with director initially oriented along the z-axis is more feasible. This is so because, the LC director arranges itself such that the total energy is minimized i.e. distortions in the director field are energetically unfavorable. This favors alignment parallel to the waveguide, because all surfaces are parallel to the z-axis. The final state of the LC cladding is oriented along the y-axis. The director can be reoriented by applying a voltage over the LC layer.

In order to design a useful tunable shallow-etched waveguide, we first consider the waveguide with a LC cladding whose director is oriented along the z-axis. For such a cladding, we determine the waveguide width (respectively wavelength) for which we have minimal leakage loss. For a fixed wavelength and for a chip containing several waveguides of different widths, we can then change the waveguide that has the magic width by simply switching the LC cladding so it reorients to be aligned along the y-axis. On the other hand, for a waveguide with a fixed width, the magic wavelength can be tuned. In both cases, the range of the tuning is proportional to the optical anisotropy of the LC.

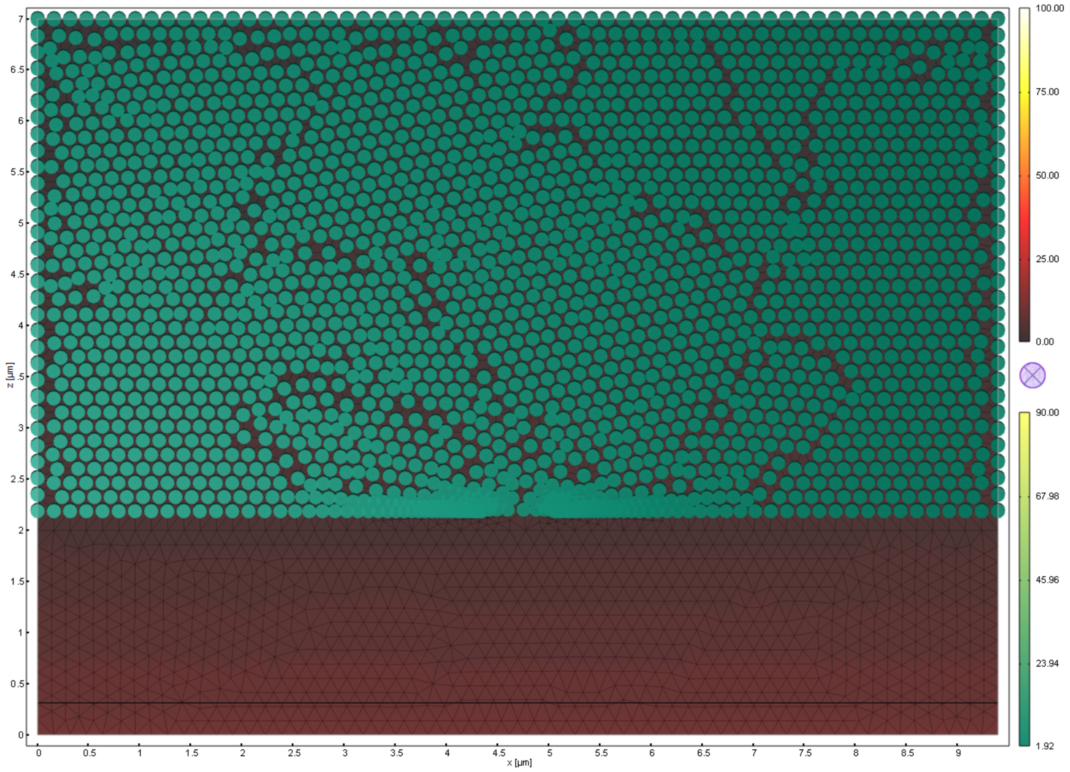

Figure 2.10: LC simulation showing the orientation of the LC cladding on a 710 nm wide shallow-etched waveguide for an applied voltage of 0 V. The upper and lower color bars are for the potential and tilt of the LC molecules. The LC directors are represented by cylinders.

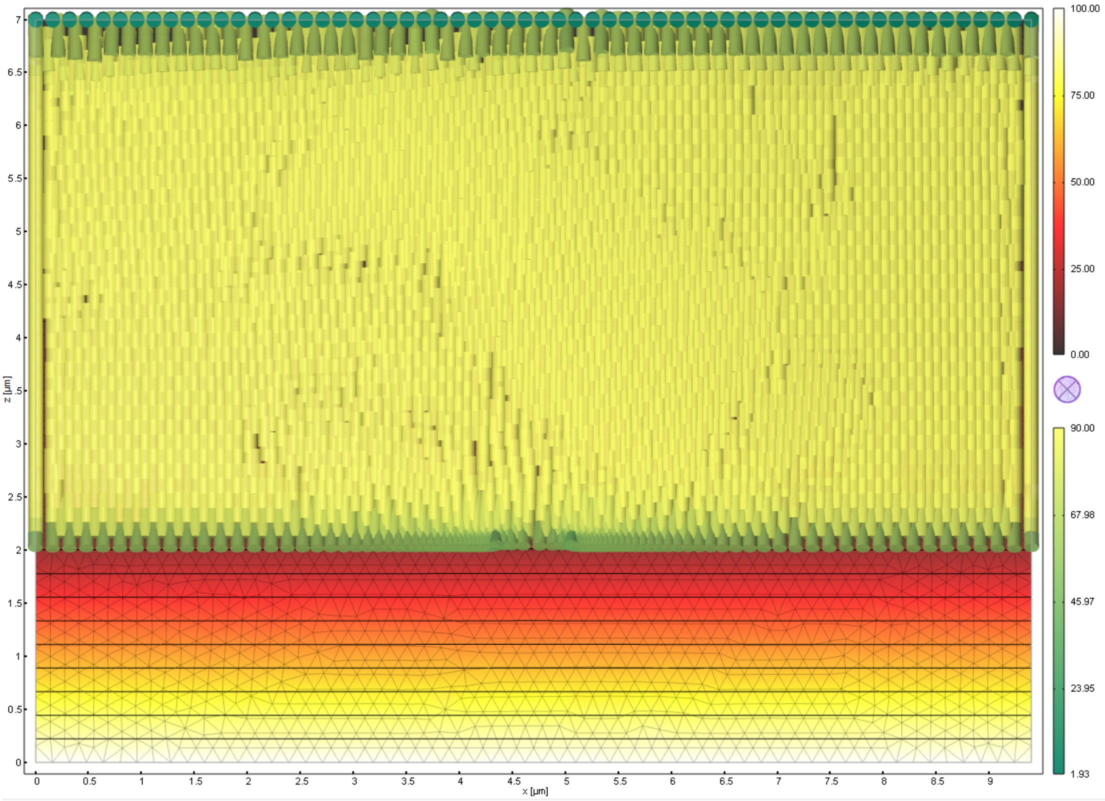

Figure 2.11: LC simulation showing the orientation of the LC cladding on a 710 nm wide shallow-etched waveguide for an applied voltage of 100 V. The upper and lower color bars are for the potential and tilt of the LC molecules. The LC directors are represented by cylinders.

The shallow-etched waveguides discussed further on in this thesis have different parameters than the ones in [3]. They have core (t_1) and slab (t_2) thickness of 220nm and 150nm respectively. These are the standard core and slab thicknesses on chips available from the ePIXfab [18] multi-project-wafer service run by IMEC. Given that the step height ($t_1 - t_2$) of the waveguides in our design is larger than in previously reported structures, we expect more leaky waveguides. The step height of the shallow-etched waveguide determines the extent of the lateral leakage loss. There are two extreme cases; $t_2 = t_1$ and $t_2 = 0$ corresponding to a slab waveguide and a rib/deep-etched waveguide respectively.

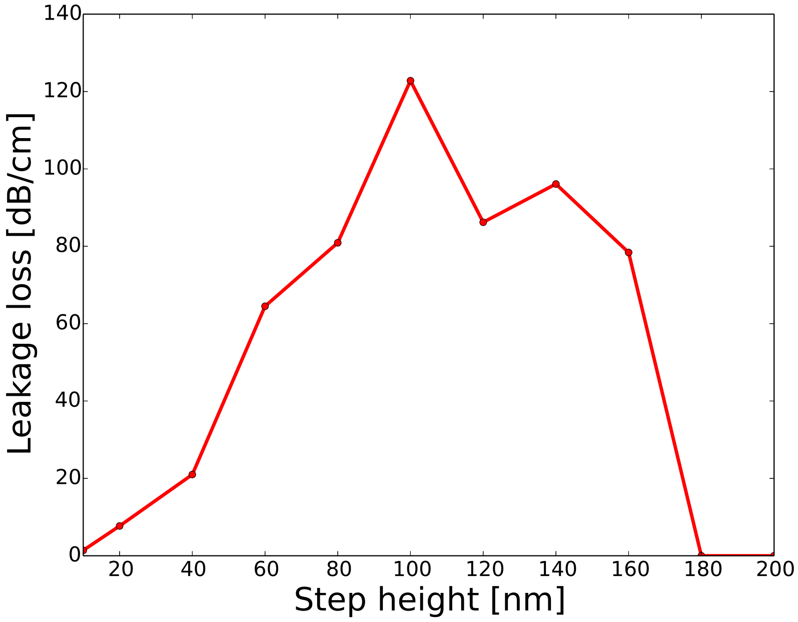

Figure 2.12: Variation of the leakage loss of the fundamental TM mode with the step height ($\Delta t = t_1 - t_2$) for an air clad 750nm wide shallow-etched waveguide with $t_1 = 220$ nm. t_2 is varied from 10 nm to 200 nm.The operating wavelength is 1550 nm.

In a slab waveguide there is no confinement in the lateral direction. The index contrast between silica, the 220nm thick active silicon layer and air provides confinement in the vertical direction. The guided modes can propagate in any direction within the active silicon layer. On the other hand, for a deep-etched waveguide, waveguide modes are confined in both the lateral and vertical directions. In the vertical direction, confinement results due to the index mismatch between silica, silicon and air whereas in the lateral direction confinement arises due to the index contrast between air and silicon. In both cases, there is no radiative mode/wave which can be phase matched to the guided modes. The lateral leakage loss phenomenon is not responsible for loss in these types of waveguides. For deep-etched waveguides, losses are typically due to scattering from the waveguide's rough side-walls. For step height values between the two extreme values, the overlap and coupling between the radiative wave in the shallow-etched slab cladding and the guided TM mode is higher. The degree of overlap and coupling increases with increasing t_2 and is optimal for $t_1 \sim 2t_2$ or $\Delta t \sim t_2$. For the latter t_2 values, the lateral leakage loss of the TM mode is increased. We illustrate this fact by simulating a 750nm wide waveguide with $t_1 = 220$nm, t_2 is varied from 10nm to 200nm. The variation of the lateral leakage loss with the step height for an operating wavelength of 1550 nm is shown in fig. 2.12. In order to get an even better picture, simulations for several wavelengths can be done. However, due to time constraints this is not done. The simulations confirm that for this waveguide width, the coupling between the fundamental TM mode and the radiative TE slab wave is optimal when Δt is close to t_2. For step heights below 10 nm and above 180 nm, we approach slab and deep-etched waveguides respectively.There is no radiative slab mode to which the guided TM mode can couple and the leakage loss is negligible. For step height values in between these two extremes, the lateral leakage loss first increases then decreases again. The waveguides we work with have a step height of 70nm, this roughly fulfils the criterion $\Delta t \sim t_2$ and ensures the waveguides exhibit a sizeable lateral leakage loss. This makes the experimental observation and tuning of the lateral leakage loss feasible.

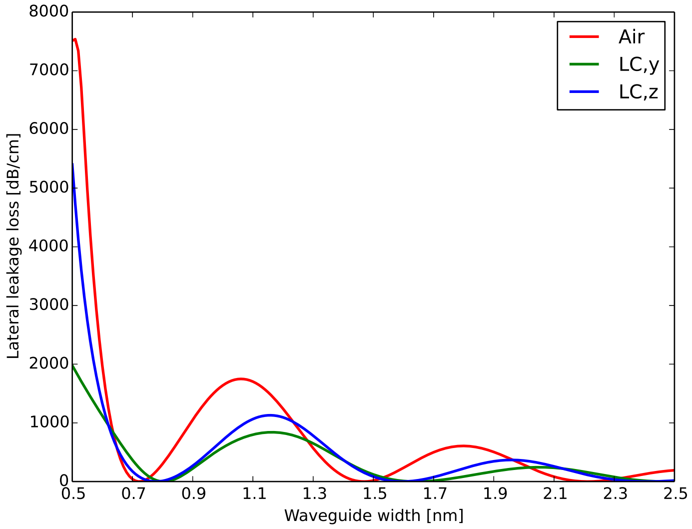

Figure 2.13: Leakage loss of the fundamental TM-like mode for a waveguide with $t_1 = 220$ nm, $t_2 = 150$ nm with various claddings for 1550 nm light. Air: the loss minima occur at 0.72 μm, 1.47 μm and 2.21 μm. LC along z: the loss minima occur at 0.78 μm, 1.60 μm and 2.41 μm. LC along y: the loss minima occur at 0.80 μm, 1.64 μm and 2.48 μm.

We proceed with investigations of the lateral leakage loss of the ePIXfab shallow-etched waveguides. The variation of the lateral leakage loss with the waveguide width for these waveguides is shown in fig. 2.13. Well-defined cyclic minima in lateral leakage loss are prominent in both fig. 2.9 and fig. 2.13 as predicted earlier. We also see a shift in magic width for LC-clad as compared to air-clad waveguides. We can also deduce three important facts about the leakage loss behavior from fig. 2.13. First, the magic width can be switched by 20 nm (from 780 nm to 800 nm) by switching the LC from being aligned along the z-axis to being aligned along the y-axis. Second, for a 780 nm wide waveguide, the leakage loss can be switched from 0 dB/cm to 19.9 dB/cm by switching the LC cladding from being aligned along the z-axis to being aligned along the y-axis. Third, for a 800 nm wide waveguide, the leakage loss can be switched from 10.8 dB/cm to 0.5 dB/cm by switching the LC cladding from being aligned along the z-axis to being aligned along the y-axis. Hence for these waveguide widths, we potentially realize a voltage tunable leakage loss switch.

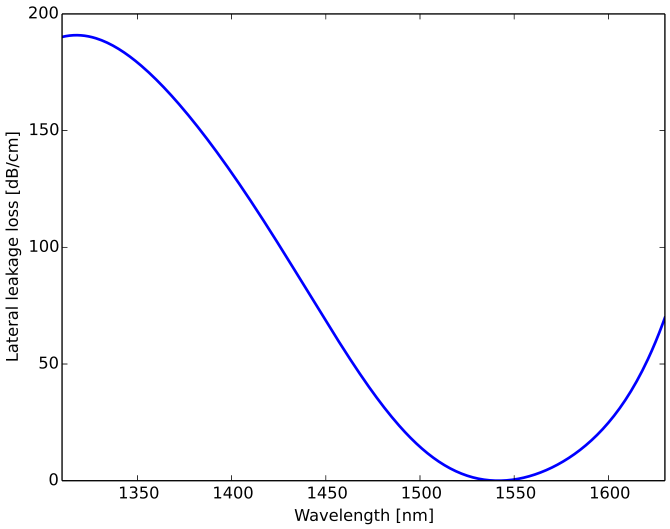

Figure 2.14: Variation of the leakage loss of the fundamental TM mode with wavelength for a 0.72 μm wide shallow-etched waveguide with t_1 =220 nm and t_2 =150 nm. The magic wavelength is 1542 nm.

On the other hand, it is also instructive to take a look at the variation of the leakage loss with the wavelength for fixed waveguide widths. As you may recall from section 2.2, there is a wavelength analogue (the magic wavelength) for the magic width. For a given shallow-etched waveguide, the TM-like mode exhibits lateral leakage loss except for certain precise wavelengths at which the loss is drastically reduced. Fig. 2.14 shows the variation of the lateral leakage loss for wavelengths between 1310 nm and 1630 nm. At the magic wavelength, the TE-like waves generated by the guided TM-like mode on each waveguide wall interfere destructively.

We follow up this initial discussion by taking a close look at the wavelength dependence of the leakage loss for air, LC along y and LC along z claddings for wavelengths between 1510 nm and 1590 nm. We are restricted to this wavelength range by the experimental setup. The wavelength dependence for an air cladding is shown in fig. 2.15. In this case the lateral leakage loss minima occur at 1526 nm, 1542 nm, and 1558 nm for 0.715 μm, 0.72 μm and 0.725 μm wide waveguides respectively. Now on to the LC clad case, the wavelength dependence for LC along y and z aligned claddings are shown in fig. 2.16 and fig. 2.17 respectively. For the LC along y cladding, the magic wavelengths are 1510 nm, 1524 nm, 1538 nm, 1552 nm and 1566 nm for 0.79 μm, 0.795 μm, 0.8 μm, 0.805 μm and 0.81 μm wide waveguides respectively. Whereas for the LC along z cladding, the magic wavelengths are 1524 nm, 1540 nm, 1558 nm, 1572 nm and 1588 nm for 0.77 μm, 0.775 μm, 0.78 μm, 0.785 μm and 0.79 μm wide waveguides

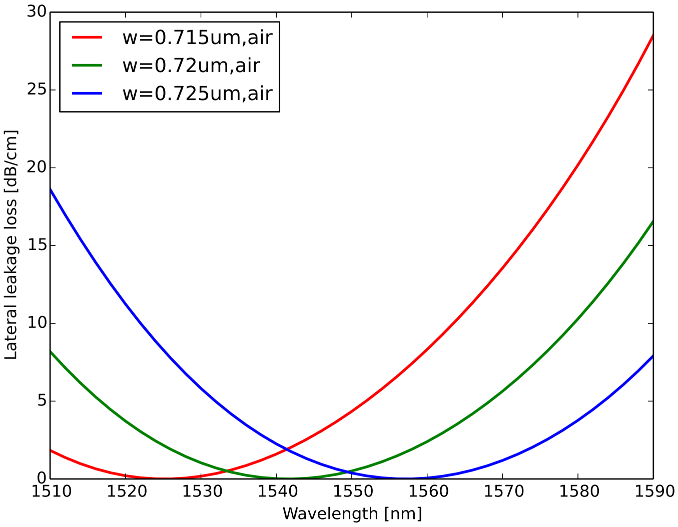

Figure 2.15: Variation of the leakage loss of the fundamental TM mode with wavelength for air clad waveguides.

respectively. From all this information, we get an idea of the range of wavelengths over which the magic wavelength can be tuned. For the 0.79 μm wide waveguide, the magic wavelength can be switched over 78 nm (from 1588 nm to 1510 nm) by switching the LC from being aligned along the z-axis to being aligned along the y-axis.

The main aim of this section was to arrive at a set of specifications for a practical device. From the analysis performed so far we can make the following conclusions. For a fixed wavelength, the first order leakage loss minimum can be adequately investigated by studying waveguides with widths ranging from 0.7 μm to 0.8 μm for all the types of cladding considered. On the other hand, for a fixed waveguide width, the wavelength window from 1510 nm to 1590 nm captures all the wavelength dependency of the first order leakage loss minimum. These two facts are the blueprint for the devices discussed later in this chapter. We design chips with waveguides which have a core (t_1) and slab (t_2) thickness of 220 nm and 150 nm respectively. Each waveguide has curved grating couplers [19] optimized for TM polarized light at each of its ends to facilitate coupling of light in and out. The period of the grating is 1050 nm and its fill factor is 50%. The mask design of shallow-etched waveguide devices was performed using the IPKISS parametric design framework [20] and fabricated by IMEC through the ePIXfab multi-project-wafer service [18].

In order to tune the lateral leakage loss in the waveguides it is necessary to integrate the chip on which the waveguides are defined into a LC cell. All the steps required to achieve this are described in the next section.

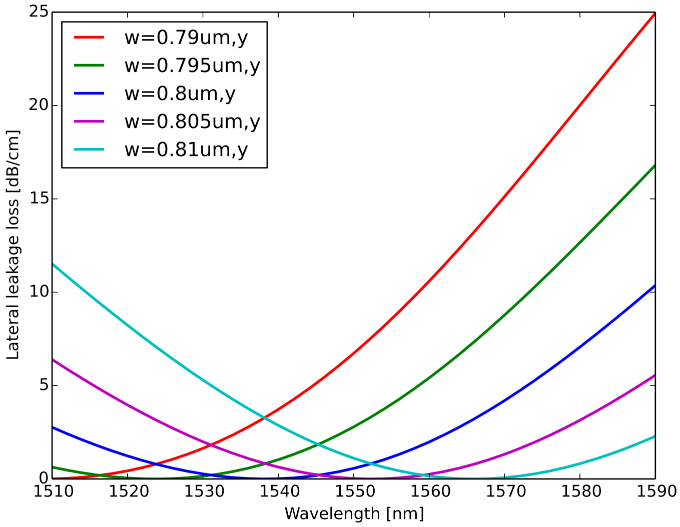

Figure 2.16: Variation of the leakage loss of the fundamental TM mode with wavelength for waveguides with LC cladding oriented along the y-axis.

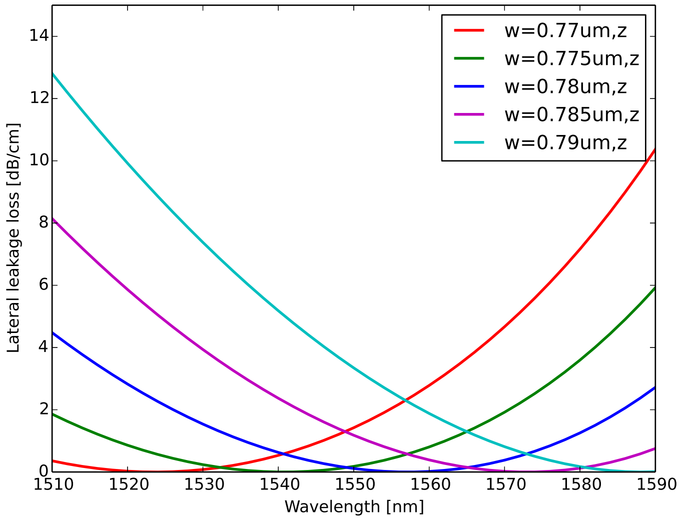

Figure 2.17: Variation of the leakage loss of the fundamental TM mode with wavelength for waveguides with LC cladding oriented along the z-axis.

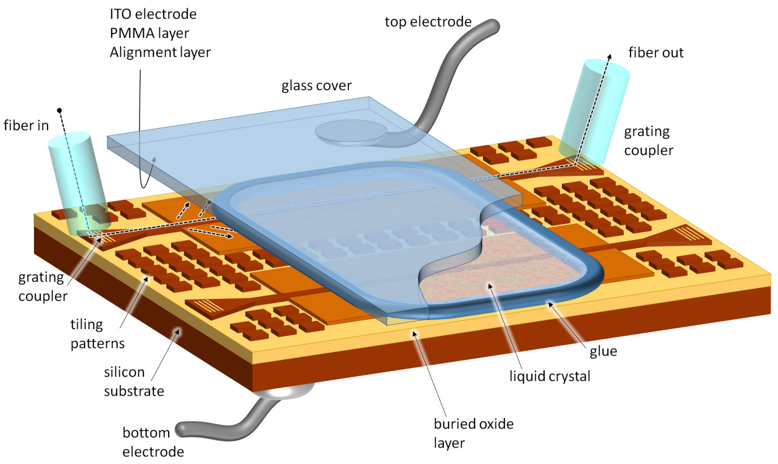

Figure 2.18: Schematic of an SOI chip with shallow-etched waveguides integrated into a LC cell.

2.5 Fabrication of LC-clad shallow-etched waveguides

This section deals with the technological processes necessary to obtain tunable LC-clad shallow-etched waveguides. We fabricate LC cells similar to those which are commonly used in the display industry [21]. The cell makes it possible to have a layer of LC on the SOI chip containing the shallow-etched waveguides we wish to tune. It also makes it possible to apply a voltage over the LC layer. Tunability is achieved when the LC reorients in response to the applied voltage. The optical properties of the LC layer are critical to the performance of our hybrid SOI-LC devices. It is desirable to have a LC layer with a uniform director distribution. Such a layer is optically uniaxial, with one preferred axis (the c-axis). This uniformity can be achieved by treating the surfaces in contact with the LC, forcing them to align in a uniform manner.

2.5.1 Fabrication of LC-clad shallow-etched waveguide devices

In a conventional LC cell, the LC layer is sandwiched between two glass plates. The glass plates are held together by UV curable glue containing spherical spacer balls. The spacer balls determine the separation between the glass plates. The glass plates are coated with a transparent conductive 30 nm thick layer of indium tin oxide (ITO). The ITO makes it possible to apply a voltage over the cell. In our test cells, the lower glass plate is replaced by an SOI chip. The silicon substrate functions as the bottom electrode in our cells. The cells are manually assembled in the clean room of Ghent University in Zwijnaarde. Some dexterity and experience is required in order to obtain good cells. All the steps involved in assembling the cells are listed below.

- **Cutting the glass plates:** The glass plates used are obtained from delta technologies [22]. They have an area of 2.5 cm x 2.5 cm and are 1.1 mm thick. The largest dimension of the silicon waveguides and HCGs we investigate is of the order of a few millimeters. In order to facilitate the characterization of the LC-clad device, it is necessary to cut the glass plate to the correct size. The cutting is done by hand with a diamond tipped pen and a ruler.

- **Cleaning the glass plates:** The LC layer in the finished cells will only be a few micrometers thick. A tiny spec of dust or dirt could ruin our cells. Consequently, the glass plates used in making the cells need to be thoroughly cleaned. The cleaning is done by successively immersing the glass plates in a 5% solution of detergent in deionized water, acetone and isopropanol. In each case the solution is contained in a beaker and placed in an ultrasonic bath for 15 minutes. The glass plates are subsequently thoroughly rinsed with deionized water. Following this, the glass plates are dried in a convection oven for 2 hours at a temperature of 105°C.

- **Spin coating the layer of PMMA:** The ITO layer on the top glass plate can cause optical losses by absorbing the evanescent tail of light guided on the SOI chip. In order to avoid this, we spin coat a layer of polymethyl methacrylate (PMMA) onto the ITO on the glass plates. This prevents optical losses in the ITO but also means we need to apply a higher voltage to reorient the LC. We use a solution made of 11 weight percent PMMA dissolved in anisole from Microchem [23]. The solution is spincoated at 2500 rotations per minute (rpm) for 90 seconds. The spin coated glass plate is pre baked at 180°C for 90 seconds on a hot plate. Following this, it is post baked in the convection oven at 95°C for 30 minutes. This results in a PMMA layer with a thickness of about 2.5 μm as confirmed by measuring the Fabry-Perot fringes in a photo-spectrometer.

- **Spin coating the alignment layer:** We use a solution made of 1 weight percent nylon dissolved in 2,2,2-trichloroethylene as the alignment layer. The solution is spun onto the glass plate at 3500 rpm for 45 seconds. The spin coated glass plates are baked in a convection oven for 4 hours at a temperature of 180°C.

- **Rubbing the glass plates:** The alignment layer on the glass plates needs to be rubbed in order to preferentially align the LC which will come in contact with it. This is done by rubbing the spin coated glass plate with a piece of soft cloth. This treatment makes sure the LC molecules align themselves in a planar manner and in the direction of the rubbing with a pre-tilt of 2° with the substrate's surface. As mentioned before, good alignment is critical for the performance of our devices. The quality of the alignment in the cell can be checked later with a polarization microscope.

- **Sealing the cells:** Following all the processing steps performed on the glass plates described above, we also clean the SOI chip with acetone, then isopropanol and rinse it off using deionized water. The SOI chip and the glass plate are held together by a mixture of UV curable glue and silica spacer balls. The spacer balls determine the spacing between the chip and the glass plate and hence the thickness of our LC cell. We experiment with spacer balls with different diameters and find spacer balls with a diameter of 5.6 μm to be optimal for our cells. The glue mixture is deposited onto the chip using a computer controlled glue dispenser. The glue dispenser makes it possible to deposit the glue in a rectangular outline, with two windows left to facilitate filling with LC.

- **Soldering wires:** In order to easily apply a voltage over the LC layer in the cell, thin electrical wires are soldered onto the ITO on the top glass plate and the underside of the SOI chip using an ultrasonic soldering machine.

- **Filling the cell:** In order to fill the cell with LC, a drop of it is placed close to the entrance of the cell. The LC material is sucked into the cell by capillary action. For cells thinner than 6 μm, filling the cell in air leads to the formation of air bubbles. In order to avoid this, the cell has to be filled in a vacuum cloak. A schematic of the finished cell is shown in fig.2.18.

2.5.2 Investigation of the alignment in the fabricated cells

In display applications, the alignment of the LC in the device is very important. This is also the case for the LC-clad SOI devices investigated in this thesis. If we have excellent alignment, the LC layer would have a uniform director distribution. It is effectively a uniaxial layer with c-axis oriented in a manner determined by the surface alignment conditions. As mentioned above the nylon alignment layer yields planar alignment on a surface with a pre-tilt of 2°. Applying a voltage to the planar aligned LC, causes it to reorient uniformly. The result is a uniform LC layer with a director oriented such that it makes an angle with the normal to the surface. Since the bottom plate (the SOI chip) in each of our cells is opaque to visible light, we use a polarization microscope working in reflection mode to investigate the alignment of LCs in our devices.

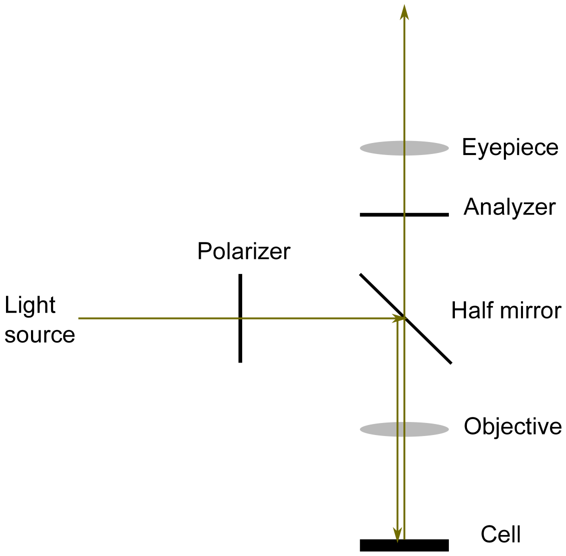

Figure 2.19: Schematic representation of the path followed by light in a polarization microscope in reflection mode.

A Nikon Eclipse E400 polarization microscope is used to inspect the alignment in our cells. The microscope has two polarizers. The first one (the polarizer) polarizes light before it hits the sample under observation, whereas the second one (also known as the analyzer) analyzes the light coming from the sample under observation. Both polarizers can be rotated independently, the most interesting configuration for studying LCs is crossed polarizers. In this configuration, the polarizer and analyzer are oriented so that they make an angle of 90° with each other. The path followed by light in the microscope when it works in reflection mode is shown in fig. 2.19. Light from a halogen lamp passes through the polarizer. The light after the polarizer is linearly polarized in the direction parallel to the axis of the polarizer. The light then reaches a half-silvered (50/50) mirror and part of it is reflected down to the cell. The light reflected from the cell passes through the half-silvered mirror and hits the analyzer before finally getting into the eyepiece where it can be comfortably observed.

When observing a sample which has no way of modifying the polarization state of the light incident on it under crossed polarizers, the image we see of the sample is dark. However, when a LC layer is observed under crossed polarizers, the image is not always dark since the LC layer can change the polarization state of the light. The transmission through the analyzer is a function of the birefringence ($\Delta n = n_e - n_o$) of the LC, thickness (d), wavelength of incident light and the angle (ϕ) the director makes with the polarizer. For a uniform LC layer with no twist, this can be expressed mathematically as;

$$T = \frac{1}{2} sin^2(2\phi) sin^2(\frac{2\pi(n_{eff} - n_o)d}{\lambda}) \tag{2.15}$$

with

$$n_{eff} = \frac{1}{\sqrt{(\frac{\cos\alpha}{n_e})^2 + (\frac{\sin\alpha}{n_o})^2}} \tag{2.16}$$

where α is the angle between the LC director and the surface of the chip. If some twist is present in the cell, polarization rotation may occur if $d >> \lambda$. This is known as the Mauguin regime. In this regime the cell should appear dark. However, for our cells we have transmission of light under crossed polarizers indicating that we are not in the Mauguin regime. For a planar aligned cell, whenever the LC director and the polarizer are not parallel, there is always some transmission through the cell with maximum transmission for $\phi = 45^\circ$. A change in the angle ϕ corresponds to rotating the cell in the microscope and keeping the polarizer and analyzer crossed. When a voltage larger than the LC threshold voltage is applied, the LC director reorients and we observe a change in transmission. For very high applied voltages, the LC molecules are aligned vertically. The c-axis is normal to both the polarizer and analyzer, the LC layer has no effect on the polarization state of the light incident on the cell. The transmission is zero.

We now consider how this applies to our cells. We start by making sure the rubbing direction in the cell is parallel to the polarizer of the microscope. We recall that only the top glass plate has an alignment layer. The rubbing direction of the alignment layer is parallel to the waveguides on the chip. For 0 V$_{rms}$ (fig.2.20), the LCs align themselves parallel to the rubbing direction close to the top glass plate. Close to the chip, the LCs find it more energetically favorable to follow the alignment enforced by the top glass plate [24]. They align themselves parallel to the waveguides. Since the polarizer is parallel to the rubbing direction, no light can make it through the analyzer. Hence the area close to the waveguides is dark. There are periodic patterning structures at a distance of about 5 μm on either side of the waveguides. These structures are periodic 70 nm deep grooves etched into the 220 nm thick active silicon layer on the SOI chip. The LC molecules inside the grating grooves tend to align vertically, whereas next to the grooves they tend to align themselves in a planar direction. This difference in alignment over the periodic structure causes defects to form over them. In these areas the polarization state of the light transmitted by the polarizer can be modified. Hence, there is some transmission through the analyzer. Accordingly, areas with the periodic structures in between the waveguides look bright. The other bright areas/spots in fig. 2.20 are mis-alignments in the LC layer due to imperfections.

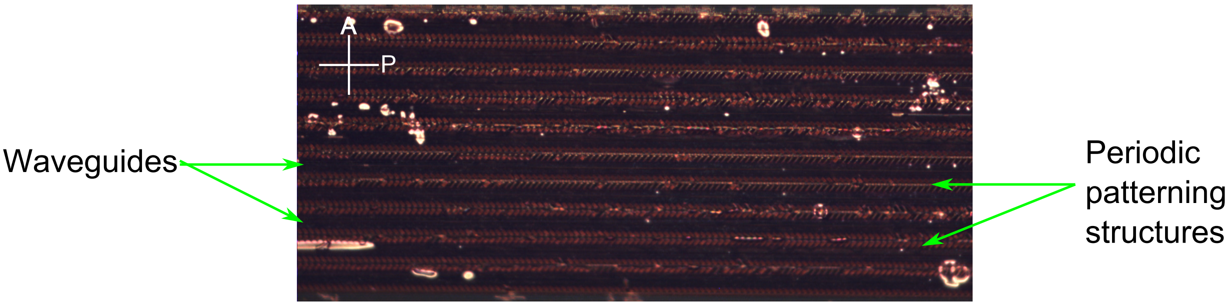

Figure 2.20: LC cell with shallow-etched waveguides under crossed polarizers in reflection mode. The applied voltage is 0 V$_{rms}$. A: Analyzer. P: Polarizer. The waveguides are parallel to the polarizer.

Once the applied voltage over the LC layer is equal to the Fréederickz threshold voltage, the LC starts switching. Due to the PMMA layer included in the cell, the voltage drop over the LC layer is only a fraction of the applied voltage. Consequently, the LC starts switching at a higher applied voltage than would be the case if the PMMA layer was absent. Fig. 2.21 shows the onset of switching in the LC layer. As the LC switches, it can now change the polarization state of the light from the polarizer. Consequently, the LC layer should get brighter with increasing voltages. Notice that the switching is more pronounced above the periodic side structures.

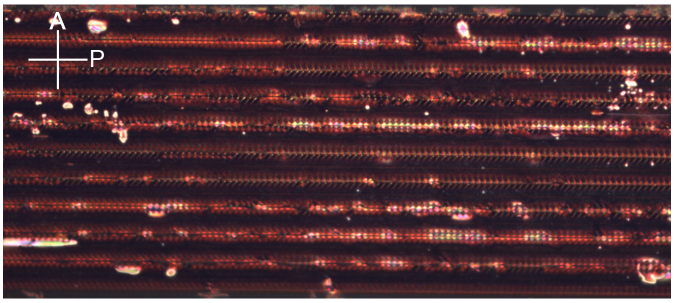

Figure 2.21: LC cell with shallow-etched waveguides under crossed polarizers in reflection mode. The applied voltage is 27 V$_{rms}$. At this voltage, the LC molecules just start switching.

For higher applied voltages, the LC switches further and the whole picture looks brighter.

2.6 Measurements

This section gives details about the measurement of the lateral leakage loss of the shallow-etched waveguides fabricated previously. A picture of the chip in the measurement setup is shown in fig.2.23. The cell is held in place by a vacuum chuck so that the waveguides are horizontal and fixed. In order to couple light in and out of a waveguide, optical fibers inclined at an angle of 10° with the vertical are placed close to the grating couplers at each end. One of the optical fibers is connected to a tunable laser source while the other one is connected to an optical power meter. With this set-up we can measure the total loss of the shallow-etched waveguide and

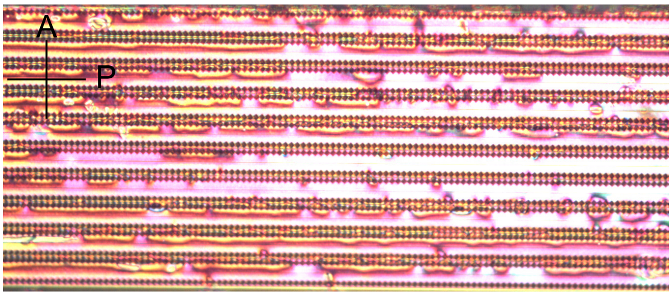

Figure 2.22: LC cell with shallow-etched waveguides under crossed polarizers in reflection mode. The applied voltage is 54 V$_{rms}$.

grating couplers. This measurement is corrected for the contribution of the grating couplers by subtracting the transmission of a short deep-etched waveguide with identical grating couplers at each of its ends. For the LC clad waveguides, part of the waveguide is still air clad. We can extract the loss of the LC clad part by using the following formula;

$$Loss_{LC} = \frac{Loss_{Total} - D_{Air}Loss_{Air}}{D_{LC}} \tag{2.17}$$

where $Loss_{Total}$, $Loss_{Air}$ and $Loss_{LC}$ are the loss for the whole, air clad part and LC clad part of the waveguide respectively. L_{Air} and L_{LC} are the fraction of the waveguide length which is air and LC clad respectively.

2.6.1 Mask designs

In the design phase described in section 2.4, we don't take into account the feasibility of a leakage loss measurement. The experimental characterization of the leakage loss of the shallow-etched waveguides designed during this PhD turned out to be quite challenging. The TE waves generated as the TM mode propagates in the waveguide can make it difficult to measure the lateral leakage loss of the waveguide. The input to and output from the shallow-etched waveguides and the structures around them can generate reflections and extra losses which make it difficult to isolate the lateral leakage loss. Three mask designs were necessary to obtain a chip with acceptable performance. The main idea is to have a silicon chip with straight shallow-etched waveguides and curved grating couplers at each end for coupling light into/out of the waveguides. Given that there are typically several possible sources of loss in integrated photonic components, it is necessary to carefully design the mask so that leakage loss can be extracted. The schematics of the main building block in each of the three mask designs produced are shown in fig. 2.24.

The widths of the waveguides are not drawn to scale. In the initial mask design (fig.2.24(a)), light is coupled into/out of the shallow-etched waveguides through single mode deep-etched waveguides. The transition from deep-etched to shallow-etched waveguides is made using an adiabatic taper. A typical measurement of the loss of this type of waveguide structure is shown in fig. 2.25. The waveguide loss shows several peaks indicating various interferences. It does not exhibit the expected dependence on the waveguide width. Moreover, the loss plotted here is for a structure with a 500 μm long shallow-etched part. The loss in dB/cm is a factor of twenty greater

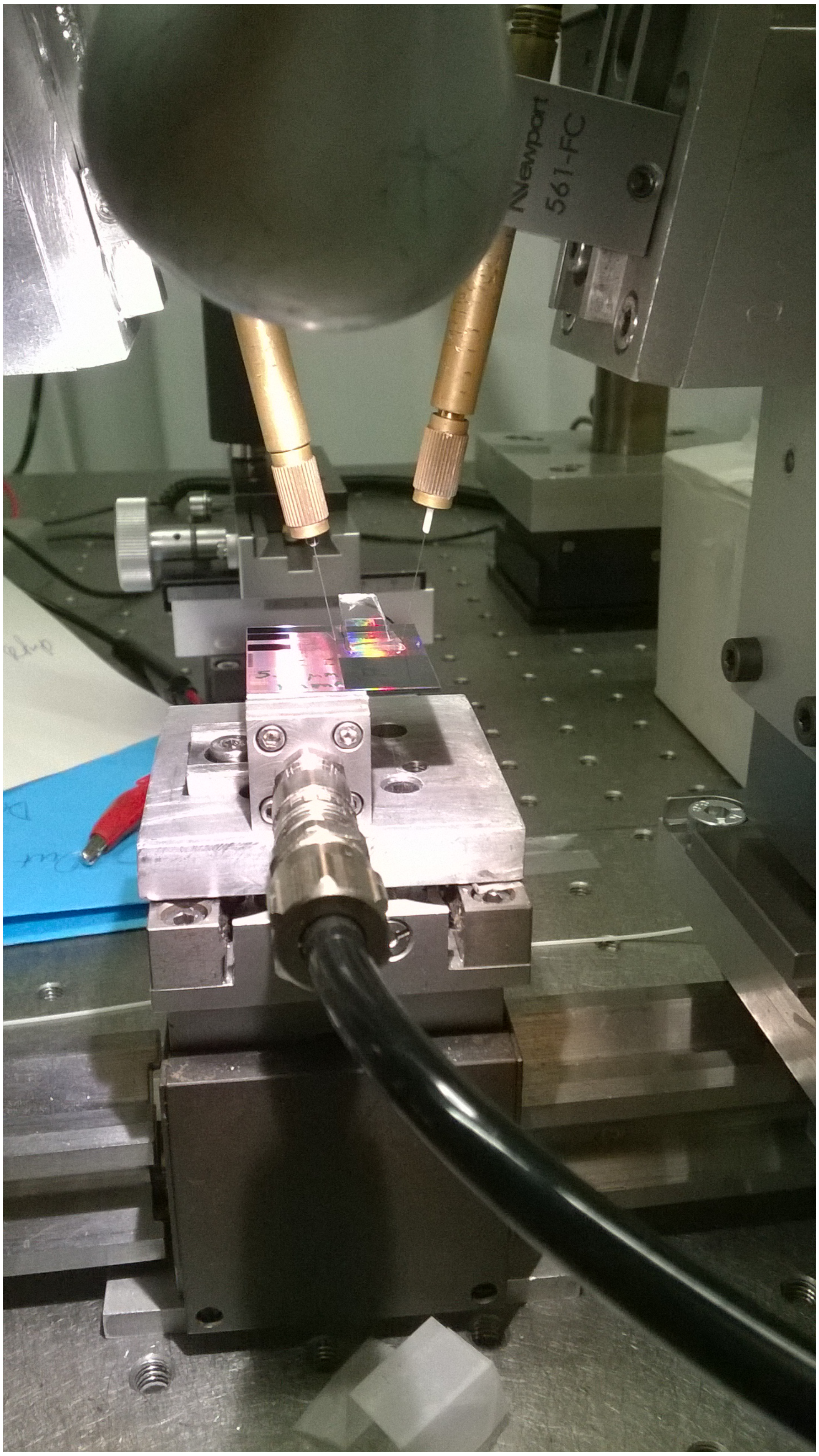

Figure 2.23: Picture of an LC cell showing the top glass plate used for aligning the LC. The optical fibers used for coupling light into and out of the waveguides are also shown.

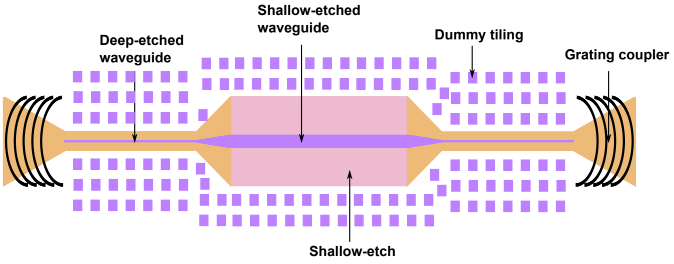

(a) First design

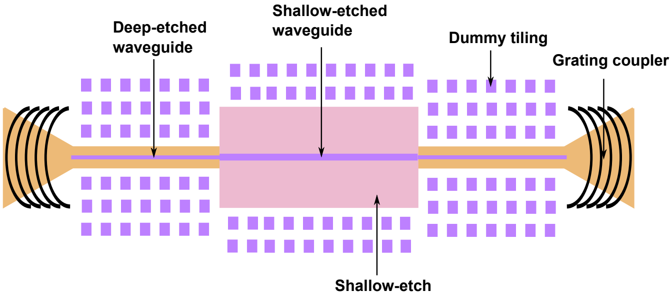

(b) Second design

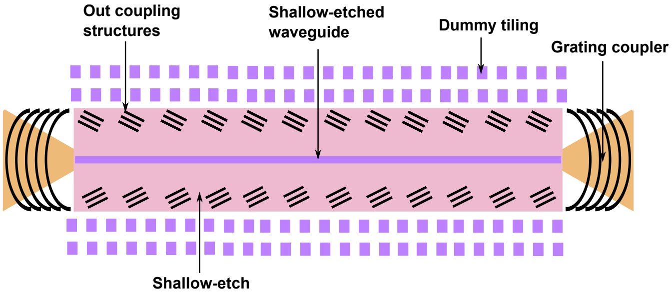

(c) Third (final) design

Figure 2.24: Disposition of shallow-etched waveguides on the chips we designed. The structures are not drawn to scale.

than the loss shown in fig. 2.25. The leakage loss behaviour of the shallow-etched waveguides can not be characterized with this chip. Careful analysis of the measurement data revealed that the peaks in fig. 2.25 arise from reflections and losses in the design. There are many sources of loss and reflections in this design. However, since the single mode deep-etched waveguides are known to have very low losses [25], the taper is probably the biggest source of loss.

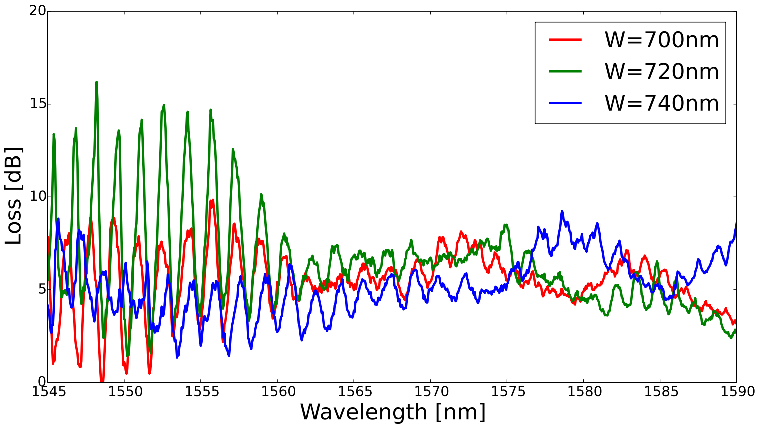

Figure 2.25: Loss as a function of wavelength for 500 μm long air-clad shallow-etched waveguides in a chip realized with mask design one. The structure of the waveguides in this design is shown in fig. 2.24(a)

Accordingly, in the second design attempt, the deep-etched and shallow-etched waveguides are butt-coupled in order to eliminate the negative effects of the taper. In order to ensure optimal coupling at the interface between the two types of waveguide, mode-matching simulations are performed to determine the optimal deep-etched waveguide width corresponding to a given shallow-etched waveguide width. The simulations indicate that the width of the deep-etched waveguide needs to be comparable to that of the shallow-etched waveguide. Since, we investigate shallow-etched waveguides with widths between 700 nm and 800 nm, the deep-etched waveguides are not single mode anymore. A loss measurement of the waveguides in a chip realized with mask design two is shown in fig. 2.26. The loss is still high, but design two is not as lossy as design one. The curves exhibit several peaks revealing the presence of interferences. The interference results from reflections from the surroundings of the shallow-etched waveguide. As the TM polarized light propagates along the shallow-etched waveguide, the TE waves which leak from it radiate away at an angle with the longitudinal direction. These radiated TE waves are (partially) reflected by the boundary of the shallow-etch on either side of the shallow-etched waveguide. Since this TE radiation is not guided by the shallow-etched waveguide, its reflection traverses the latter and gets (partially) reflected by the other shallow-etch boundary and so on. Additionally, the transition from shallow-etched to deep-etched causes even more reflections for the leaky TE radiation. At the grating coupler, we detect a mixture of the TM polarized light guided by the waveguide and the TE polarized light which has undergone multiple interferences and reflections. It is not possible to extract the leakage loss of the shallow-etched waveguides from such a complicated signal. Consequently, a third mask design is necessary. In mask design three, grating couplers directly couple light to and out of the shallow-etched waveguides, this ensures we have no unwanted reflections in the longitudinal direction. In order to ensure that the TE radiation leaking out of the shallow-etched waveguide does not 'contaminate' the TM signal we intend to measure, out-coupling structures are defined on either side of the waveguides. They serve to couple TE radiation leaking from the waveguide away from the chip in the vertical direction. Chips realized according to mask design three yield the best leakage loss results. All results presented in the rest of this chapter are for such chips.

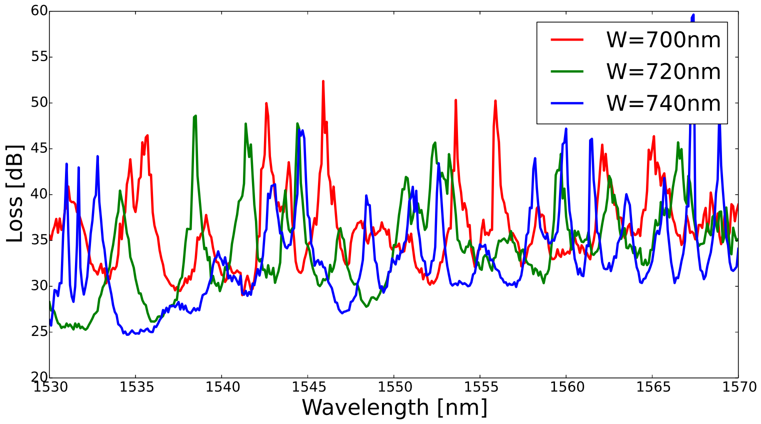

Figure 2.26: Loss as a function of wavelength for 0.5 mm long air-clad shallow-etched waveguides in a chip realized with mask design two. The structure of the waveguides in this design is shown in fig. 2.24(b)

2.6.2 Tunable lateral leakage loss

This section is devoted to the measurement of the loss of the shallow-etched waveguides in the final design presented above. We endeavor to minimize all other sources of loss in the set-up. Assuming these other losses are negligible, the loss we measure is then equal to the lateral leakage loss in the waveguide. We first take a look at the simpler case of air-clad shallow-etched waveguides. The results of the loss measurements and simulations for some air clad waveguides are displayed in fig. 2.27.

We observe excellent agreement between experiment and simulation. The measurement results presented here agree with previous theoretical and experimental results [3–5, 8, 11]. This confirms that the waveguides we designed exhibit lateral leakage loss as expected. There is however a discrepancy between the designed waveguide width (W_D) and the waveguide width (W) on the chip. Fig. 2.27 suggests that the waveguides designed to be 680 nm, 700 nm and 720 nm wide are actually 710 nm, 730 nm and 755 nm wide. This is confirmed by SEM imaging of the chip.

We now turn our attention to LC clad waveguides. The LC cell is fabricated such that the LC molecules in the cladding are initially oriented along the waveguides (z-axis). In this case, the TM-like mode feels a voltage dependent index in the upper cladding given by;

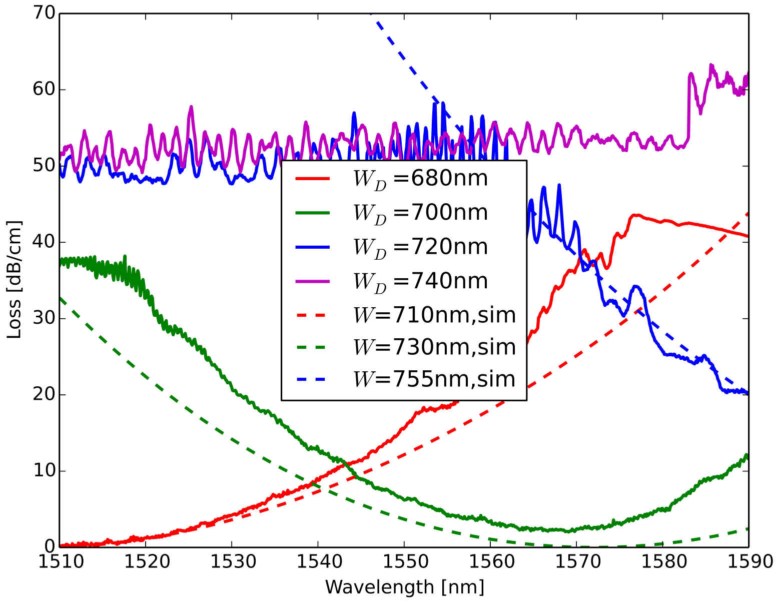

Figure 2.27: Loss as a function of wavelength for air-clad shallow-etched waveguides. Solid and dashed curves are for experimental and simulation data respectively.

$$n_{clad} = \frac{1}{\sqrt{(\frac{\cos\gamma}{n_o})^2 + (\frac{\sin\gamma}{n_e})^2}} \tag{2.18}$$

with γ the angle the LC director makes with the z-axis. For low voltages, γ is close to zero and n_{clad} is close to n_o. On the other hand, for high applied voltages, γ is close to 90° and hence n_{clad} is close to n_e. When we have an LC cladding, the wavelength at which the minimum in leakage loss occurs shifts to shorter wavelengths compared to the air-clad case. This is the case because for an LC clad waveguide $n^{(core)}_{eff,TE}$ and $N_{eff,TM}$ both increase. Even though the increase in $N_{eff,TM}$ is greater than that in $n^{(core)}_{eff,TE}$, the latter is still greater than the former. Consequently, for a fixed waveguide width, the numerator in (2.4) decreases resulting in the resonance condition being fulfilled at a shorter wavelength. Fig. 2.28 compares the loss as a function of the wavelength for air and LC clad (oriented along the z-axis, 0 V_{rms}) waveguides. As expected, the leakage loss is preserved for the LC clad case. The W_D =740 nm waveguide is interesting because its loss minimum falls well within the wavelength window we constrain ourselves to. The other waveguides have their loss minima at shorter (W_D =720 nm) and longer (W_D =780 nm) wavelengths respectively.

We also compare the loss of the LC clad waveguides with the model developed earlier for designing the waveguides. We find excellent agreement between simulation and experiment as shown in fig. 2.29. We once more notice a discrepancy between the design (W_D) and on-chip (W) waveguide width. The waveguides designed to be 720 nm and 740 nm wide are actually

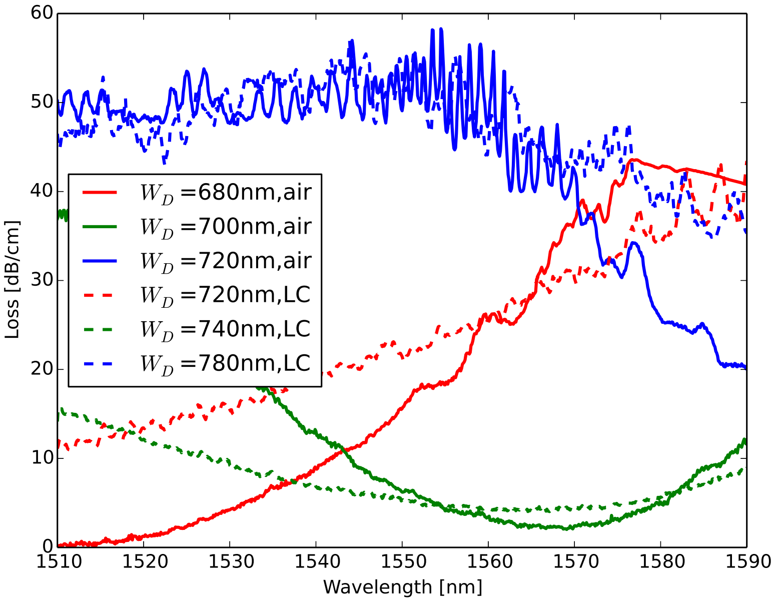

Figure 2.28: Loss as a function of the wavelength for air and LC (0 V_{rms}) clad shallow-etched waveguides. Solid and dashed curves are for air and LC cladding (oriented along the z-axis) respectively.

755 nm and 785 nm wide respectively. In order to determine the range of wavelengths over which the loss minimum can be tuned, we model the waveguides with an LC cladding oriented along the y (high applied voltage) and z (zero applied voltage) axes respectively. We perform simulations following the procedure explained in section 2.3.2. The 5.6 μm thick LC cladding layer is modeled as a uniaxial layer with c-axis along the z (green dashed curve) and y (black dashed curve) axes respectively. The extraordinary and ordinary refractive indices used are those of the common LC E7 ($n_e = 1.697$ and $n_o = 1.5024$ at 1550 nm [26]). We then deduce that it is theoretically possible to switch the position of the loss minimum by more than 70 nm by reorienting the LCs in the cladding from being aligned along the z-axis to being aligned along the y-axis. We achieve this reorientation by applying a voltage over the LC cladding of the waveguide. We apply a sinusoidal voltage at a frequency of 1 KHz with zero offset to the cell. We ramp the amplitude of the voltage up in steps of 13 V$_{rms}$ from 0 V$_{rms}$ to 201 V$_{rms}$. For each voltage step, we measure the loss as a function of wavelength. All these measurements are collected and displayed together for the W =785 nm waveguide in fig. 2.30. We observe that the loss minimum shifts to shorter wavelengths with increasing voltage as expected. We measure a shift of 39.5 nm, from 1564 nm at 0 V$_{rms}$to 1524.5 nm at 201 V$_{rms}$. On the other hand, we notice that the shift in wavelength is accompanied by an increase in loss of just over 8 dB/cm for an increase in voltage of 201 V$_{rms}$.

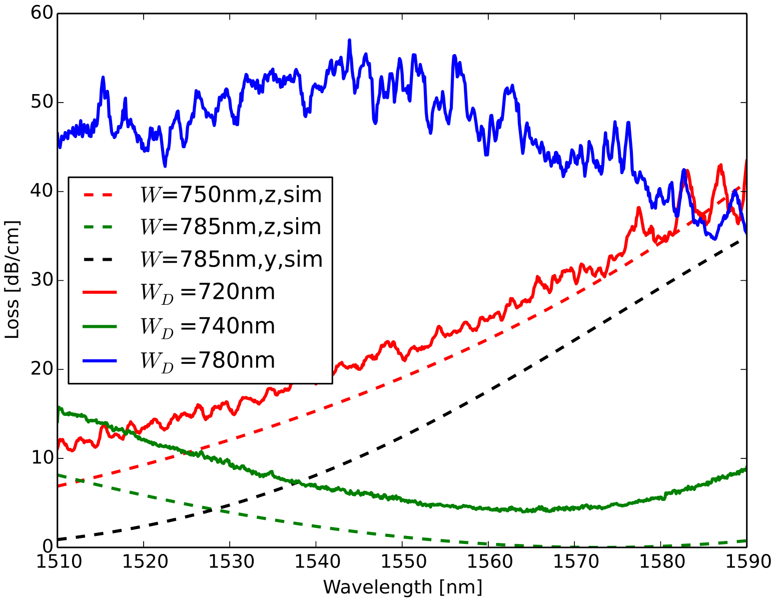

Figure 2.29: Loss as a function of the wavelength for LC (0 V) clad shallow-etched waveguides. Solid and dashed curves are for experimental and simulation data respectively. All the experimental data is for an LC cladding layer oriented along the z-axis.

For a fixed wavelength, it is also possible to increase or decrease the loss with increasing applied voltage. The extent of this decrease or increase can be extracted from fig. 2.30. We

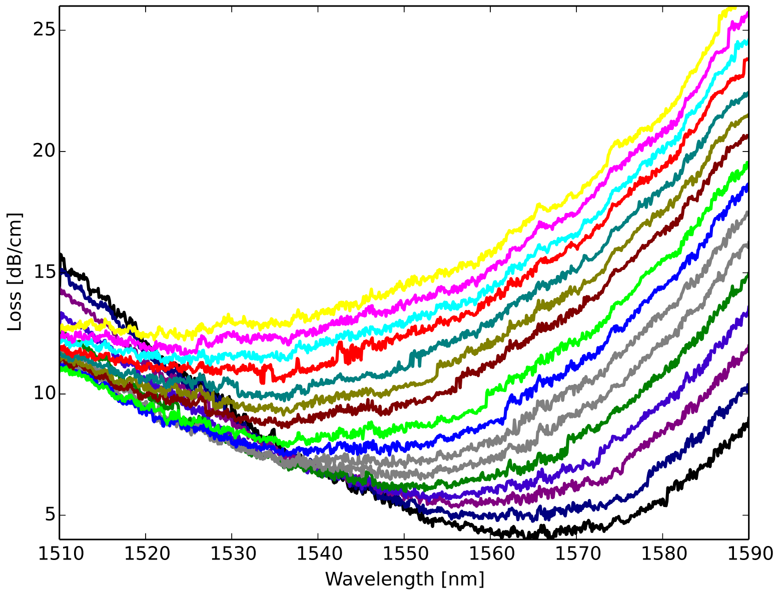

Figure 2.30: Loss as a function of the wavelength for a W =785 nm LC clad shallow-etched waveguide. The applied voltage increases from 0 V_{rms} (black curve) to 201 V_{rms} (yellow curve).

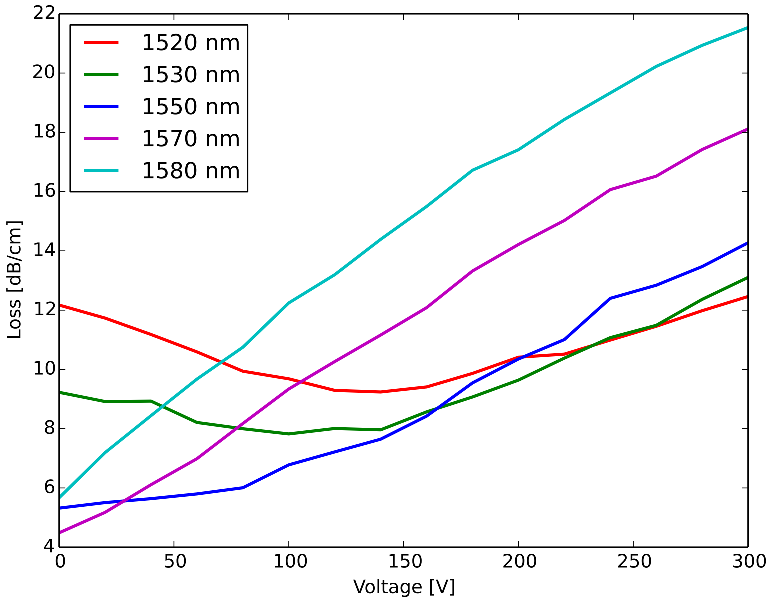

Figure 2.31: Loss as a function of the applied voltage for a W =785 nm LC clad shallow-etched waveguide.

choose five different wavelengths for which we collect the loss with increasing applied voltage. The result is plotted in fig. 2.31. For the wavelengths 1520 nm and 1530 nm we expect the loss to decrease continuously with increasing applied voltage. This is not the case, the loss we measure initially decreases with increasing applied voltage. For higher voltages, the loss increases again. For example at a wavelength of 1520 nm, the loss decreases from 12.2 dB/cm at 0 V$_{rms}$ to 9.2 dB/cm at 94 V$_{rms}$, it then starts increasing again attaining 12.5 dB/cm at 201 V$_{rms}$. This is mainly due to the increased loss for higher applied voltages. On the other hand, for 1550 nm, 1570 nm and 1580 nm, the loss increases continuously with increasing applied voltage. For example, we measure an increase in loss of 13.6 dB/cm (from 4.5 dB/cm at 0 V$_{rms}$ to 18.1 dB/cm at 201 V$_{rms}$) and 15.8 dB/cm (from 5.7 dB/cm at 0 V$_{rms}$ to 21.5 dB/cm at 201 V$_{rms}$) for 1570 nm and 1580 nm respectively.

2.7 Issues affecting optimal leakage tuning

This section addresses issues which affect the optimal tuning performance of the LC-clad shallow-etched waveguides. First, we take a closer look at the actual voltage drop over the LC layer in the device. Second, we explain why in addition to shifting to shorter wavelengths with increasing applied voltage, the loss at the magic wavelength increases as well. Finally, we consider the effect the switching of the LC has on the leakage loss of the LC-clad shallow-etched waveguides.

	1 V	100 V
V_{silica}	0.2	29.1
V_{LC}	0.4	16.2
V_{PMMA}	0.4	54.6

Table 2.1: Voltage drop over the dielectric layers in the LC cell for given applied voltages.

2.7.1 Magnitude of the applied voltage

The voltages applied to the cell are quite high. Such high voltages are necessary because the LC cells we fabricate have the silicon substrate as the lower electrode. With three dielectric layers i.e. silica, LC and PMMA sandwiched between two electrodes. When we apply a voltage to the cell, if we neglect the 220 nm thick layer of silicon in which the waveguides are defined, we essentially have a parallel plate capacitor with three different dielectrics. In such a device, the voltage drop over each layer is inversely proportional to its dielectric permittivity. The dielectric permittivity of silica and PMMA in the KHz range is equal to 3.9 [27] and 2.6 [28]. For the LC, the extraordinary and ordinary dielectric permittivity in the KHz range is equal to 19.6 and 5.1 [?]. For low applied voltages, the LC molecules are oriented along the z-axis and the dielectric permittivity is 5.1, whereas for high applied voltages, the LC molecules are more or less oriented along the y-axis and their dielectric permittivity is equal 19.6. Accordingly, the voltage drop over the LC layer is only a fraction of the total voltage applied to the cell. The voltage applied to the cell and the voltage drops across each dielectric layer are related as follows;

$$V = V_{silica} + V_{LC} + V_{PMMA} = \int_{0\mu m}^{2\mu m} \frac{D_o}{\varepsilon_{silica}} dy + \int_{2\mu m}^{7.6\mu m} \frac{D_o}{\varepsilon_{LC}} dy + \int_{7.6\mu m}^{10.1\mu m} \frac{D_o}{\varepsilon_{PMMA}} dy \tag{2.19}$$

with V_{silica}, V_{LC} and V_{PMMA} the voltage drop over the silica (oxide), LC and PMMA layers. D_o is the dielectric field in in each of the layers inside the capacitor. ε_{silica}, ε_{LC}, and ε_{PMMA} is the dielectric permittivity of the silica, LC and PMMA respectively. Using (2.18) we can calculate the respective voltage drops for any applied voltage. We tabulate the results of such a calculation in table 2.1. For low voltages, the voltage drop over the LC is about 40% of the total applied voltage. For high applied voltages, the voltage drop over the LC is only 16% of the total applied voltage. Tuning can be achieved with lower applied voltages by appropriately placing the electrodes in the cell. Since shallow-etched waveguides are suited to lateral electrical access, lower applied voltages can be used for tuning if we contact the waveguide so that it functions as the bottom electrode of the LC cell. In addition to top-bottom LC switching, in-plane switching can be achieved by appropriately contacting electrodes in the slab cladding on either side of the waveguide core.

2.7.2 Increase in loss with increasing applied voltage

This sub-section is devoted to determining why the loss of the LC clad waveguide increases with increasing applied voltage. In addition to filling the cell, LC also extends outside it, and covers the part of the waveguide there (see fig. 2.32). When a voltage is applied to the cell, the LC in the cell reorients while the LC outside doesn't. We recall that on the chip surface, the LCs find it energetically favorable to align their long axes parallel to the waveguides (i.e. along the z-axis). Even though the LC layer shown in both pictures in fig. 2.32 is not that uniform, close to the waveguides we have a more or less uniform LC layer. If we assume that the part of the waveguide which is not under the glass plate is completely covered with LC, then the loss we measure for the waveguide when a voltage is applied to the LC cladding can be written in a manner similar to (2.17) as follows;

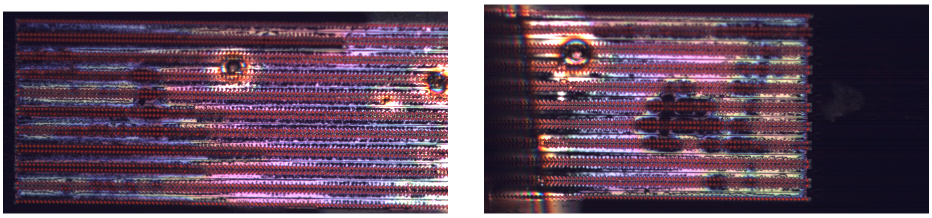
(a) Part of waveguides to the left of the cell (b) Part of waveguides to the right of the cell

Figure 2.32: Part of the waveguides outside the cell is also covered with LC.

$$Loss_{total} = 0.3Loss_{novoltage} + 0.7Loss_{voltage} \tag{2.20}$$

i.e. when a voltage is applied over the cell, the total loss we measure is a weighted sum of the loss over the part of the waveguide inside the cell (with the LC reoriented) and loss over the part of the waveguide outside the cell (with the LC still roughly pointing along the z-axis). In order to model the leakage loss of the waveguide for increasing applied voltage, we model the LC cladding as a uniaxial layer with extraordinary index n_{clad} and ordinary index n_o. The increase in applied voltage is simulated by varying the angle γ in (2.18) from 0° to 70° in steps of 10°. The leakage loss as a function of the wavelength for increasing γ is plotted in fig. 2.33.

The loss minima shift to shorter wavelengths with increasing voltage (i.e. increasing γ). There is no overall increase in leakage loss since in the simulation we assume the director of LC layer matches precise values of γ all over the waveguide. Now if we apply (2.20) to the simulation results plotted in fig. 2.33 we get the plot shown in fig. 2.34

This new plot is qualitatively equivalent to fig. 2.30. As the loss curve shifts to shorter wavelengths with increasing applied voltage, the loss increases as well. This indicates that the LC switching of the leakage loss is probably greater than what we reported in section 2.6. Fig. 2.30 and fig. 2.34 only correspond qualitatively because equation 2.20 is an approximation. Since the glass plate for the LC cell is hand-cut, its length is most likely not equal to 7 mm i.e. the part of the waveguides covered by reoriented LC is not always equal to 70 % of its total length. In addition to this uncertainty in the length of the glass plate, there is a (about 0.25 mm long) patch of UV curable polymer/glue covering the waveguides (and holding the glass plate in place) at each end of the glass plate. The glue (NOA 65) we use has a refractive index of 1.524, so it has roughly the same effect as the un-oriented LC outside the cell. All these mean the factors 0.3 and 0.7 in eq. 2.20 are only indicative values. Furthermore, the refractive indices of the nylon (30 nm thick and n = 1.53) and PMMA (2.5 μm thick and n = 1.498) layers above the LC as well as the imperfections at their interface are not included in the simulation. Since

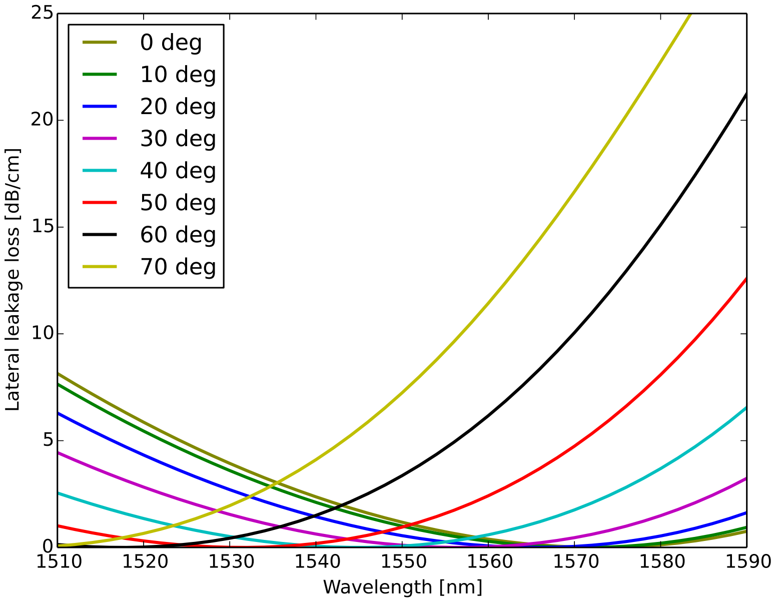

Figure 2.33: Loss as a function of the tilt angle in the LC cladding for a W =785 nm shallow-etched waveguide. The LC is initially oriented along the z-axis ($\gamma = 0°$).

these contribute to the losses measured experimentally but were not taken into account explicitly in the simulation, we can't get an exact quantitative match between the simulated and measured loss curves.

2.7.3 Liquid crystal switching

The dynamics of the LC switching has a tremendous effect on the loss we measure. The defects in the LC cladding cause scattering of light in the cladding. The scattering increases the coupling between the unguided TE polarized radiative slab mode and the guided TM mode. This enhances the loss in the waveguide and renders the measurement of leakage loss difficult. When we apply a voltage to the cell, the defects created above the side gratings propagate through the cell. This occurs because when a voltage is applied to the cell, the LCs always reorient themselves such that their elastic energy is minimized. Typically, defects can propagate over a distance comparable to the thickness of the cell. In our cell, this means that they can reach the waveguides and increase the scattering close to them. Given that the loss we measure for an air and LC cladding at zero applied voltage are comparable. This increase with scattering due to propagating defects in the LC cell contributes to the experimentally observed increase in loss with increasing applied voltage. This increase in loss can be mitigated by increasing the separation between the waveguides and the side grating. This increase in separation has no effect on the side gratings' ability to prevent radiated TE fields from being reflected back to the waveguide.

In addition to the defects, for intermediate applied voltages, the LCs can minimize their energy in a myriad of ways. This is true even for uniformly aligned areas of the LC cladding.

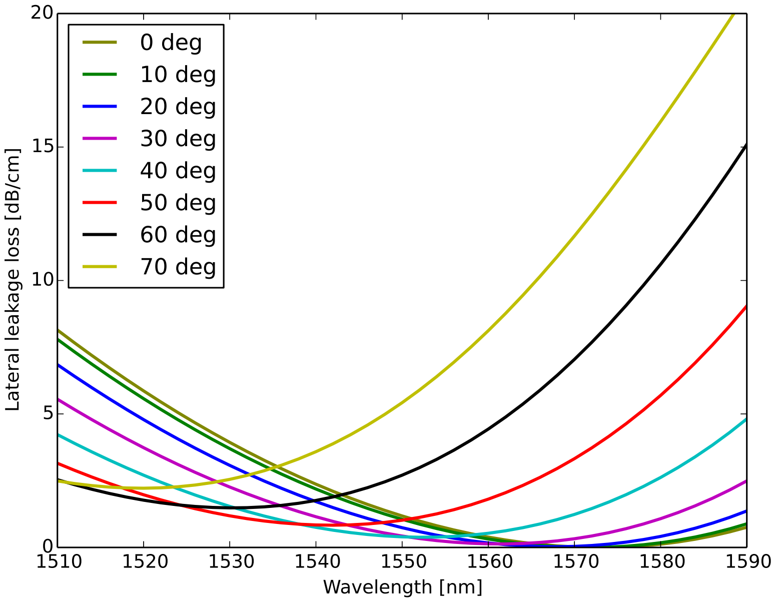

Figure 2.34: Mimicking the experimentally measured loss as a function of the applied voltage for a 785 nm wide LC clad shallow-etched waveguide. The LC is initially oriented along the z-axis.

The LCs do not only tilt in response to an applied voltage, they also twist to some extent. The LCs can have a slight left or right hand twist; both are energetically identical. This twisting is yet another source of scattering in the LC cladding layer.

2.8 Discussion

We also consider how well the tuning demonstrated here compares with previously reported results. The leakage loss tuning demonstrated here is for straight shallow-etched waveguides. Using long straight waveguides makes the assembly (by hand) of the LC cells easier. More compact designs can be obtained by curling the waveguides up in spirals. In such a scenario, avoiding the formation of domains in the LC upper cladding will be quite challenging. The side gratings would be especially handy in coupling light out/away from the chip in the vertical direction, preventing leaky TE radiation generated in one section of the spiral from interacting with the guided TM signal in adjacent parts of the spiral. These out-coupling structures need to be placed sufficiently far from the waveguide core, so that inhomogeneities in LC alignment caused by the former don't propagate to the latter and cause scattering.

It is also very important to assess how the loss measured here compares to previously reported results. [29, 30] report shallow-etched waveguides with propagation losses of 0.3 dB/cm and 0.03 dB/cm respectively for TE polarized light for wavelengths close to 1550 nm. These losses are for 2 μm and 3 μm wide shallow-etched waveguides respectively. These waveguides are relatively wide and the propagation loss of the wider waveguide is lower since the waveguide mode seldom interacts with the side walls. We work with TM polarized light and measure a loss minimum of 0.3 dB/cm for a 710 nm wide waveguide at a wavelength of 1510 nm. Such loss performance is comparable with that of the wider shallow-etched waveguides and mentioned earlier and results from the fact that the waveguide width is close to a magic width. For LC clad shallow-etched waveguides, we observe a deterioration of the loss performance. The minimum in loss is now close to 4.5 dB/cm for a 785 nm wide waveguide at a wavelength of 1570 nm. This loss can be varied (reversibly) by about 15 dB/cm (i.e. loss maximum beyond 20 dB/cm) by switching the LC. Investigations of the tuning the loss of a waveguide are not widely reported in the literature, emphasis is usually placed on obtaining waveguides with minimal losses [25, 31–35]. [36] propose an interesting method for designing low-loss shallow-etched waveguides in lithium niobate by exploiting the latter's anisotropic properties. The reduction of the propagation loss of deep-etched and slot waveguides with layers of titanium dioxide is reported in [37]. However, the magnitude of the loss reduction is only consequential for narrow waveguides. For example the propagation loss of the TE mode in a 230 nm wide waveguide can be reduced from above 50 dB/cm to 5.7 dB/cm (at 1550 nm) by covering it with a 50 nm thick layer of titanium dioxide. In contrast, for a 450 nm wide waveguide the titanium dioxide layer has no effect on the propagation loss. This is understandable since the waveguide mode is less strongly confined in the narrower waveguide. The weaker confinement means the covering layer can have a tremendous effect on the loss of the waveguide. Given the mechanism by which lateral leakage loss occurs in shallow-etched waveguides, it is expected that the addition of a dielectric layer covering to such waveguides will result in a change in leakage loss. A straightforward method for doing this would be to cover the waveguide with silica. The work presented in this thesis goes a step further than this. By using a LC covering on the waveguide, the leakage properties of the waveguide can be modified in a reversible manner by applying a low frequency (sinusoidal) voltage. In this way we demonstrate tunable lateral leakage loss and show that the transmission of the shallow-etched waveguide can be switched by about 15 dB/cm. Given that a lot of time was spent iterating through various designs to get reliable experimental measurements of the lateral leakage loss, there was no time to perform in depth measurements of the switching time of the device. However, we expect switching times of a few millisecond given the typical relaxation time of LCs. These results compare well with other results of waveguides covered with a smart fluid. Typical examples of this include the tuning of the modes in optical fibers with long-period grating [38, 39] as well as on-chip tuning by electrowetting [40, 41]. The latter case is especially interesting as it is a configuration similar to the case we consider here. In these examples on-chip micro ring resonators are tuned by changing the wetting properties of a fluid inside a microfluidic channel by application of a voltage. In [41] the extinction of the transmission can be changed by over 30 dB for wavelengths close to 1557 nm for an applied voltage of 285 V_{rms}. This is more than twice that achieved in our case. However, the maximum in transmission (corresponding to the minimum in leakage loss or magic width) can only be switched (between voltage-on and voltage-off) by about 0.5 nm whereas in our case we achieve switching of the transmission maximum over a 40 nm wide wavelength range. The switching of the on-chip device with electrowetting is in the sub-millisecond (hundreds of microseconds) regime, meaning it is more advantageous (from a dynamic response point of view) than our LC clad waveguides.

2.9 Conclusion

Shallow-etched SOI waveguides are a type of waveguide in which light is confined in the lateral and vertical direction. While confinement in the vertical direction is due to the refractive index mismatch between air, silicon and silica, lateral confinement arises due to the difference between the thickness of the waveguide's core and slab cladding. These waveguides are especially useful for applications requiring lateral electrical access to a waveguide. Despite their interesting geometry and usefulness, these waveguides exhibit high losses for the TM polarization. For a fixed wavelength, there exists a waveguide width at which this loss is minimal. Conversely, for a waveguide with a fixed width, there exists a wavelength at which the leakage loss is minimal.

The mechanism by which leakage loss arises in these waveguides has been explained. We start off with the well known case for an air-clad waveguide. We move on to the more complex case of a LC clad waveguide. We analyze the new physics which arises as a result of having such a cladding and conclude that it opens up the possibility of tuning the leakage loss by applying a voltage over it. We then embark on designing waveguides suitable for observing this tunable leakage loss and arrive at a set of waveguides with the appropriate parameters for tunable leakage loss around the 1550 nm telecommunication wavelength. Following this, we experimentally characterize the waveguides designed earlier and confirm that it is indeed possible to tune the leakage loss. We then determine the tuning range and round up by discussing practical issues which can improve the performance of the device we propose here.

Bibliography

[1] M.A. Webster, R.M. Pafchek, G. Sukumaran, and T.L. Koch. *Low-Loss Quasi-Planar Ridge Waveguides Formed on Thin Silicon-On-Insulator*. Appl. Phys. Lett., 87(23), 2005.

[2] R. Pafchek, R. Tummidi, J. Li, M.A. Webster, E. Chen, and T.L. Koch. *Low-Loss Silicon-On-Insulator Shallow-Ridge TE and TM Waveguides Formed Using Thermal Oxidation*. Appl. Optics, 48(5):958–963, 2009.

[3] M.A. Webster, R.M. Pafchek, A. Mitchell, and T.L. Koch. *Width Dependence of Inherent TM-Mode Lateral Leakage Loss in Silicon-On-Insulator Ridge Waveguides*. IEEE Phot. Tech. Lett., 19(6):429–431, 2007.

[4] M. Koshiba, K. Kakihara, and K. Saitoh. *Reduced Lateral Leakage Losses in TM-Like Modes in Silicon-On-Insulator Ridge Waveguides*. Opt. Lett., 33(17):2008–2010, 2008.

[5] K. Kakihara, K. Saitoh, and M. Koshiba. *Generalized simple theory for estimating lateral leakage loss behavior in Silicon-On-Insulator ridge waveguides*. J. Lightwave Tech., 27(23):5492–5499, 2009.

[6] T.G. Nguyen, R.S. Tummidi, T.L. Koch, and A. Mitchell. *Rigorous Modeling of Lateral Leakage Loss in SOI Thin-Ridge Waveguides and Couplers*. Photonics Technology Letters, IEEE, 21(7):486–488, April 2009.

[7] T.G. Nguyen, R.S. Tummidi, T.L. Koch, and A. Mitchell. *Lateral Leakage of TM-like Mode in Thin-ridge Silicon-On-Insulator Bent Waveguides and Ring Resonators*. Opt. Express, 18(7), 2010.

[8] N. Dalvand, T.G. Nguyen, R.S. Tummidi, T.L. Koch, and A. Mitchell. *Thin-ridge Silicon-on-Insulator Waveguides with Directional Control of Lateral Leakage Radiation*. Opt. Express, 19(6):5635–5643, 2011.

[9] N. Dalvand, T.G. Nguyen, T.L. Koch, and A. Mitchell. *Thin Shallow-Ridge Silicon-on-Insulator Waveguide Transitions and Tapers*. Photonics Technology Letters, IEEE, 25(2):163–166, Jan 2013.

[10] A.A. Oliner, S.T. Peng, T.I. Hsu, and A. Sanchez. *Guidance and Leakage Properties of a Class of Open Dielectric Waveguides: Part II-New Physical Effects*. IEEE Trans.Microw. Theory and Tech., 29(9):855–869, sep 1981.

[11] T. Ako, J. Beeckman, W. Bogaerts, and K. Neyts. *Tuning the lateral leakage loss of TM-like modes in shallow-etched waveguides using liquid crystals*. Appl. Optics, 53(2):214–220, jan 2014.

[12] Jianming Jin. *The Finite Element Method in Electromagnetics*. John Wiley & Sons, Inc., 2002.

[13] F. A. Fernandez, S. E. Day, P. Trwoga, H. F. Deng, and R. James. *Three-Dimensional Modelling of Liquid Crystal Display Cells using Finite Elements*. Molecular Crystals and Liquid Crystals, 375(1):291–299, 2002.

[14] R. James, Eero Willman, F.A. Fernandez, and S.E. Day. *Finite-element modeling of liquid-crystal hydrodynamics with a variable degree of order*. Electron Devices, IEEE Transactions on, 53(7):1575–1582, July 2006.

[15] Richard James. *Modelling of high resolution liquid crystal devices*. PhD thesis, University College London, 2006.

[16] P. de Gennes and J. Prost. *The physics of liquid crystals*. Clarendon press, 1993.

[17] *GID The personal pre and post processor*. `http://www.gidhome.com/`. Accessed: 2015-01-12.

[18] *ePIXfab*. `http://www.epixfab.eu`. Accessed: 2014-11-12.

[19] Dirk Taillaert, Peter Bienstman, and Roel Baets. *Compact efficient broadband grating coupler for silicon-on-insulator waveguides*. Opt. Lett., 29(23):2749–2751, Dec 2004.

[20] *IPKISS parametric design framework*. `http://www.ipkiss.org`. Accessed: 2014-11-12.

[21] J. Beeckman, K. Neyts, and P. Vanbrabant. *Liquid-Crystal Photonic Applications*. Opt. Engineering, 50(17), 2011.

[22] *Product data sheet*. `http://www.delta-technologies.com/products.asp?C=1`. Accessed: 2014-10-28.

[23] *Nano PMMA and copolymer data sheet*. `http://www.microchem.com/pdf/PMMA_Data_Sheet.pdf`. Accessed: 2014-10-28.

[24] Hans Desmet, Kristiaan Neyts, and R. Baets. *Modeling nematic liquid crystals in the neighborhood of edges*. Journal of Applied Physics, 98(12):123517–123517–6, Dec 2005.

[25] Shankar Kumar Selvaraja, Wim Bogaerts, Philippe Absil, Dries Van Thourhout, and Roel Baets. *Record Low-loss Hybrid Rib/Wire Waveguides for Silicon Photonic Circuits*. In Group IV Photonics, 7th International conference, Proceedings, page 3. IEEE, 2010.

[26] Jun Li, Shin-Tson Wu, Stefano Brugioni, Riccardo Meucci, and Sandro Faetti. *Infrared refractive indices of liquid crystals*. Journal of Applied Physics, 97(7):–, 2005.

[27] P.R. Gray, P.J. Hurst, S.H. Lewis, and R.G. Meyer. *Analysis and Design of Analog Integrated Circuits*. Wiley, New York, 5th edition, 2009.

[28] *Dielectric permittivity of PMMA*. `http://www.mit.edu/~6.777/matprops/pmma.htm`. Accessed: 2014-10-28.

[29] P. Dong, W. Qian, S. Liao, H. Liang, C.C. Kung, N.N. Feng, R. Shafiiha, J. Fong, D. Feng, A.V. krishnamoorthy, and M. Asghari. *Low Loss Shallow-Ridge Silicon Waveguides*. Opt. Express, 18(14):14474–14479, 2010.

[30] Guoliang Li, Jin Yao, Hiren Thacker, Attila Mekis, Xuezhe Zheng, Ivan Shubin, Ying Luo, Jin hyoung Lee, Kannan Raj, John E. Cunningham, and Ashok V. Krishnamoorthy. *Ultralow-loss, high-density SOI optical waveguide routing for macrochip interconnects*. Opt. Express, 20(11):12035–12039, May 2012.

[31] H. Tian, G. Winzer, A. Gajda, K. Petermann, B. Tillack, and L. Zimmermann. *Fabrication of low-loss SOI nano-waveguides including BEOL processes for nonlinear applications*. Journal of the European Optical Society - Rapid publications, 7(0), 2012.

[32] Jaime Cardenas, Carl B. Poitras, Jacob T. Robinson, Kyle Preston, Long Chen, and Michal Lipson. *Low loss etchless silicon photonic waveguides*. Opt. Express, 17(6):4752–4757, Mar 2009.

[33] D.A.P. Bulla, Wei-Tang Li, C. Charles, R. Boswell, A. Ankiewicz, and J.D. Love. *Low-loss silica-based optical film waveguides deposited by helicon-activated reactive evaporation*. Lightwave Technology, Journal of, 23(3):1302–1307, March 2005.

[34] Yurii Vlasov and Sharee McNab. *Losses in single-mode silicon-on-insulator strip waveguides and bends*. Opt. Express, 12(8):1622–1631, Apr 2004.

[35] A Layadi, A Vonsovici, R Orobtchouk, D Pascal, and A Koster. *Low-loss optical waveguide on standard SOI/SIMOX substrate*. Optics Communications, 146(1,Äì6):31 – 33, 1998.

[36] Emi Saitoh, Yuki Kawaguchi, Kunimasa Saitoh, and Masanori Koshiba. *A design method of lithium niobate on insulator ridge waveguides without leakage loss*. Opt. Express, 19(17):15833–15842, Aug 2011.

[37] T. Alasaarela, D. Korn, L. Alloatti, A. Säynätjoki, A. Tervonen, R. Palmer, J. Leuthold, W. Freude, and S. Honkanen. *Reduced propagation loss in silicon strip and slot waveguides coated by atomic layer deposition*. Opt. Express, 19(12):11529–11538, Jun 2011.

[38] Bharat R. Acharya, Tom Krupenkin, Siddharth Ramachandran, Z. Wang, C. C. Huang, and John A. Rogers. *Tunable optical fiber devices based on broadband long-period gratings and pumped microfluidics*. Applied Physics Letters, 83(24):4912–4914, 2003.

[39] J. Hsieh, P. Mach, F. Cattaneo, S. Yang, T. Krupenkine, K. Baldwin, and J.A. Rogers. *Tunable microfluidic optical-fiber devices based on electrowetting pumps and plastic microchannels*. Photonics Technology Letters, IEEE, 15(1):81–83, Jan 2003.

[40] Yoav Zuta, Ilya Goykhman, Boris Desiatov, and Uriel Levy. *On-chip switching of a silicon nitride micro-ring resonator based on digital microfluidics platform*. Opt. Express, 18(24):24762–24769, Nov 2010.

[41] Romi Shamai and Uriel Levy. *On chip tunable micro ring resonator actuated by electrowetting*. Opt. Express, 17(2):1116–1125, Jan 2009.

3

Deep-etched Silicon Waveguides

3.1 Introduction

Deep-etched silicon-on-insulator waveguides are the basic building block of photonic integrated circuits. They are central to components like ring resonators [1], de-multiplexers [2], on-chip beam steerers [3, 4] and spectral filters [5] etc. Most of these components are passive, with fixed functionalities. However, in view of realizing smart photonic integrated circuits with reconfigurable optical switches/interconnects and on-chip tunable spectral filters, it is interesting to have tunable silicon waveguides. In [6, 7], the authors demonstrate on-chip spectral filtering. They achieve this by tuning LC-clad silicon-on-insulator micro-ring resonators with a voltage (applied over the LC). In this chapter, we investigate the possibility of using LC-clad deep-etched silicon waveguides as reconfigurable switches.

3.2 Waveguide modes

Deep-etched waveguides support both transverse electric (TE) and transverse magnetic (TM) polarized modes. Here we only consider waveguides which support the fundamental TE and TM modes. Due to the strong index contrast that exists between the waveguide core and its cladding, these waveguide modes are birefringent with distinct effective indices for the TE and TM modes. Even though the E_x and E_y are the dominant electric field components of the TE and TM mode respectively, the other electric field components also have a considerable magnitude (see fig. 3.1). Despite the fact that the modes are guided, there is some light extending beyond the core of the waveguide. Consequently, when a deep-etched waveguide is clad with LC, the LC interacts with the modes of the waveguide and the orientation of the LC director determines the manner in which the effective indices of the waveguide modes change.

We now consider how the LC cladding affects the waveguide modes. The LC director can be oriented along the x, y and z axes respectively. When the director is oriented along the x-

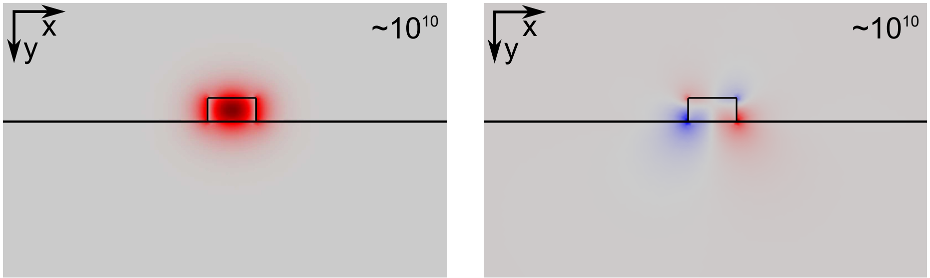

(a) TE mode, x-component of E-field (E_x) (b) TM mode, x-component of E-field (E_x)

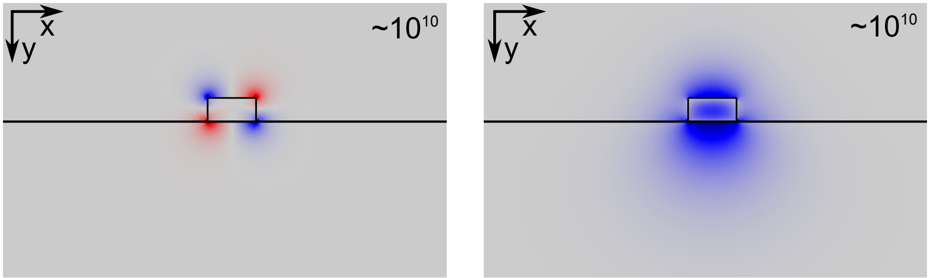

(c) TE mode, y-component of E-field (E_y) (d) TM mode, y-component of E-field (E_y)

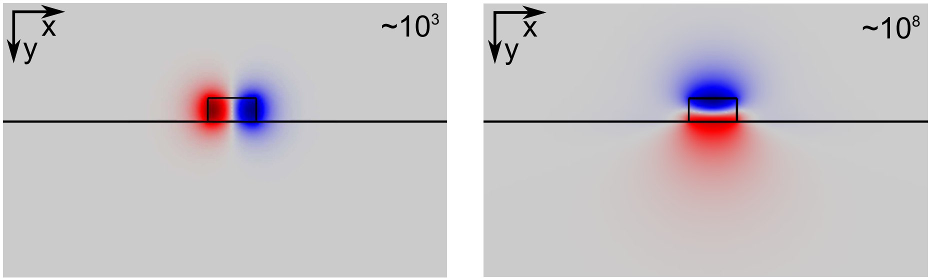

(e) TE mode, z-component of E-field (E_z) (f) TM mode, z-component of E-field (E_z)

Figure 3.1: Field profiles of all three electric field components for the fundamental TE and TM modes in a deep-etched waveguide. The numbers in the inset indicate the order of magnitude of the fields which have units of V/m.

axis, the modes feel an index n_e along the x-axis and n_o along the y and z axes. Next, when the director is oriented along the y-axis, the modes feel an index n_e along the y-axis and n_o along the x and z axes. Finally, when the director is oriented along the z-axis, the modes feel an index n_e along the z-axis and n_o along the x and y axes. Compared to air-clad waveguides, the modes of LC-clad waveguides have higher effective indices. Since E_x is the dominant electric field component for the TE mode, the LC interacts with the mode strongly when its director is oriented along the x-axis. For the other two orientations (y and z axes), the interaction between the mode and the LC cladding is not strong. As such, if the orientation of the director can be varied, from being aligned along the x-axis to being aligned along either the y or z axes, the TE waveguide mode can be tuned. On the other hand, E_y is the dominant electric field component for the TM mode. Consequently, the LC interacts with the mode strongly when its director is oriented along the y-axis. For the other two orientations (x and z axes), the LC cladding does not interact strongly with the TM mode. The director is typically reoriented by applying a voltage over the LC.

Reorienting the director from being oriented along the x-axis to being oriented along either the z-axis or the y-axis (for tuning the TE mode) should lead to similar tuning performance. However, in practical devices the LC director usually prefers to be aligned along waveguides [8]. Consequently, the designs considered further on are for director reorientation from the z-axis to the y-axis.

3.3 Tuning a conventional deep-etched waveguide

Commonly used deep-etched waveguides are 450 nm wide and 220 nm high [5].They are passive and only support the fundamental TE and TM modes. The modes have fixed effective indices. However, when the waveguide has an LC cladding, the effective indices of the waveguide modes can be continuously tuned. In this section, we perform simulations that demonstrate how the modes in such a deep-etched waveguide can be tuned by reorienting the director of the LC cladding. Following the method described in section 2.3, we use the LC simulation program and COMSOL multiphysics to simulate the LC orientation and the modes of the waveguide respectively. We start our analysis with the air-clad waveguide. The geometry used for obtaining the waveguide modes for an air-cladding is shown in fig. 3.2.

We obtain TE and TM modes with effective indices of 2.271 and 1.540 respectively. We now turn our attention to the LC-clad waveguide. As mentioned above, we only consider the case where the LC director is initially oriented along the z-axis and is subsequently reoriented in the y-z plane by applying a voltage over the LC cladding. We use the parameters of the LC E7. The geometry used for the LC simulation is shown in fig. 3.3. At the alignment layers, we specify a pre-tilt of 2° for the LC. In a typical device, there is no alignment layer on the surface of the chip. We take the alignment of the LC at the chip surface into account by considering weak anchoring at the surface. The anchoring energy is critical in determining the extent of the reorientation of the director close to the waveguide. As such we compare how different anchoring energies affect the tuning of the waveguide modes. The evolution of the effective index of the TE mode with the applied voltage is shown in fig. 3.4.

The TE mode always feels an index n_o in the LC cladding.The simulation of the air-clad waveguide reveals that for the TE mode, the E_z component is much smaller (6 orders of magnitude) than the E_x and E_y components. Consequently, as the director reorients from being

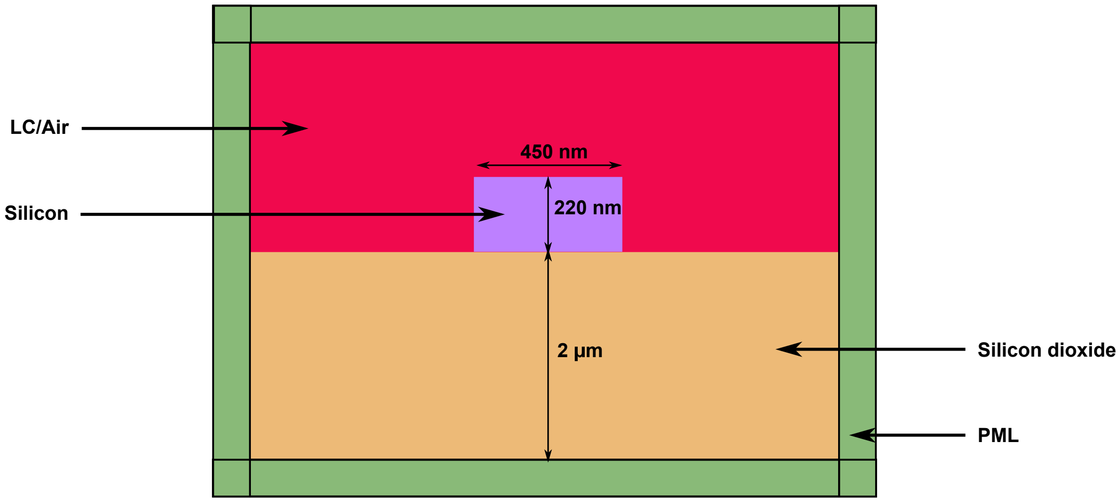

Figure 3.2: Simulation domain used in COMSOL.

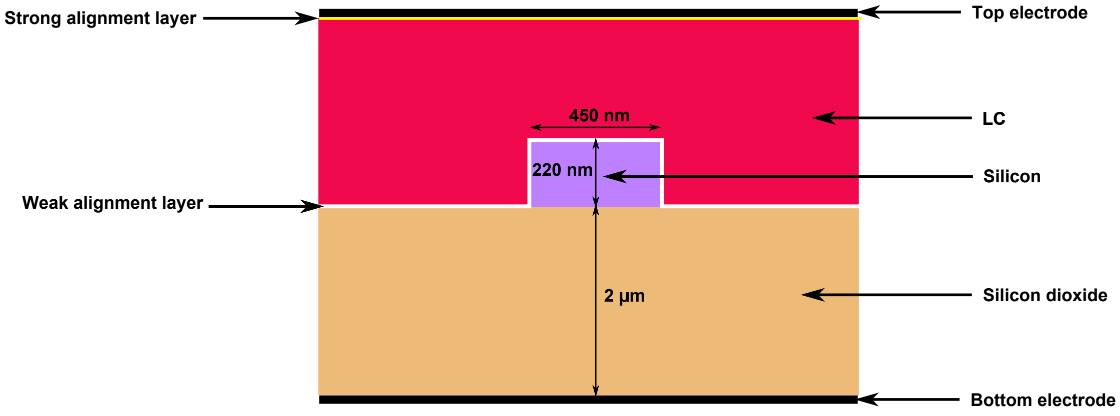

Figure 3.3: Geometry used for the LC simulation.

along the z-axis to being along the y-axis, the interaction between the LC and the weaker E_z component decreases. This is accompanied by an increase in the interaction between the LC and the stronger E_y component. Therefore as the voltage over the LC is increased, the director reorients, the index felt by the TE mode in the cladding increases and the effective index of the waveguide mode increases. We observe that the anchoring energy can have a drastic impact on the variation of the effective index. Lower anchoring energy means the LC director can reorient more easily, achieving a larger reorientation for a given applied voltage (compared to higher anchoring energy). For the lower anchoring energy (10^{-5} Jm^{-2}) the effective index increases faster and saturates at 37.5 V. For an anchoring energy of 10^{-4} Jm^{-2} the change in effective index is approximately linear and does not saturate.

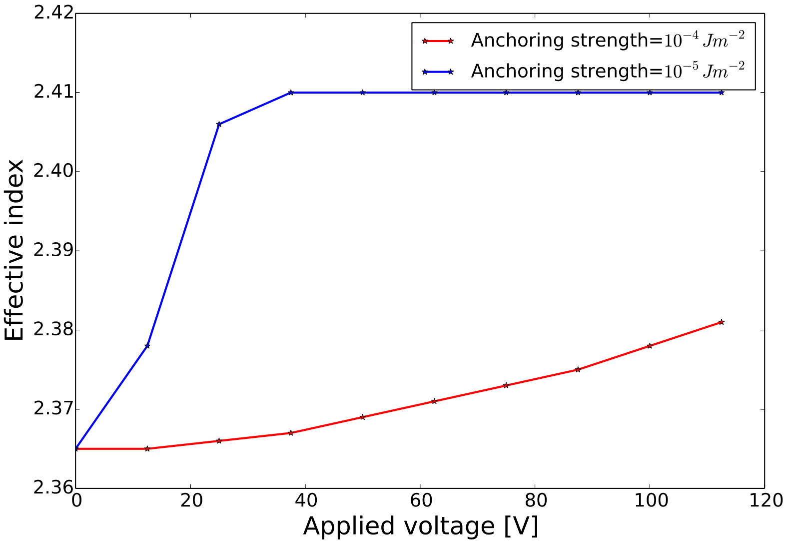

Figure 3.4: Variation of the effective index of the TE mode as a function of the applied voltage.

The variation of the effective index of the TM mode as a function of the applied voltage is shown in fig. 3.5. For the TM mode, when the LC is oriented along the z-axis, the E_y and E_z components feel an index n_o and n_e respectively in the cladding. As the applied voltage is increased, the director reorients (in the y-z plane) so it makes an angle with the z-axis. In this case the E_y and E_z components feel a weighted average of n_o and n_e. For the E_y (respectively E_z) component, the value of this weighted average increases (respectively decreases) with applied voltage from n_o (respectively n_e) for no voltage to n_e (respectively n_o) for high applied voltages. Hence as the voltage increases, the effective index of the TM mode increases. This increase in effective index is larger than that for the TE mode due to the relative magnitude and spatial variation of the E_y and E_z components in both cases.

We also observe a saturation in the increase of the effective index for the TM mode for a lower anchoring energy (10^{-5} Jm^{-2}). For an anchoring energy of 10^{-4} Jm^{-2}, the increase in effective index is more gradual. Experimental tests performed on silicon chips (reported in Chapter 2) reveal that the scenario with an anchoring energy of 10^{-4} Jm^{-2} is realistic. We use this anchoring energy for the rest of this chapter. The simulations performed so far indicate (as expected) that the interaction between the waveguide modes and the LC cladding increases with increasing voltage. Consequently, if the waveguide is narrow enough that there is more light in the cladding, the loss of the waveguide modes can be increased by increasing the index in the cladding i.e. by reorienting the LC director from being aligned along the z-axis to being aligned along the y-axis. This is investigated in the next section.

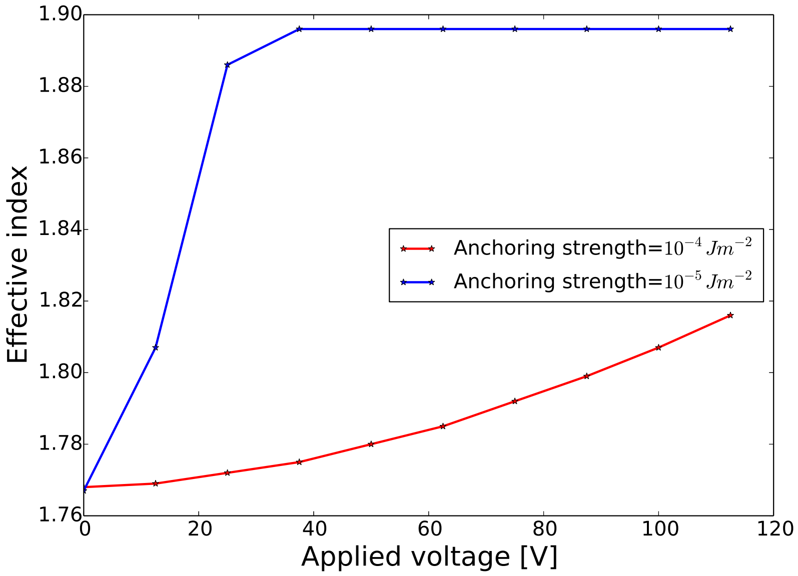

Figure 3.5: Variation of the effective index of the TM mode as a function of the applied voltage.

3.4 Narrow deep-etched waveguides

In this section we investigate deep-etched waveguides with different widths and aim to drive the waveguide modes into cut-off by increasing their loss. The width of the waveguides considered are narrower than 450 nm. Air-clad Waveguides which are narrower than 300 nm don't support any guided modes. In contrast, 280 nm wide LC-clad waveguides support the fundamental TE and TM modes. However, the waveguide is not yet narrow enough that the loss of its modes can be increased by applied voltage. As the waveguide width is decreased further, we expect to find a waveguide whose modes exhibit an increase in loss with increasing applied voltage. For a 220 nm wide LC-clad waveguide, the effective index of the waveguide modes increase with increasing applied voltage. The loss of the waveguide modes does not increase with increasing applied voltage for voltages below 200 V. For a voltage of 300 V, the loss of the TM mode in this waveguide is equal to 1.27 dB/cm.

On the other hand, the 200 nm wide waveguide is a good example of a waveguide with excellent loss tuning for applied voltages under 200 V. The variation of the loss of the waveguide modes as a function of the applied voltage is shown in fig. 3.6. The TE mode is found to be slightly lossier than the TM mode. This is expected since at a width and height of 200 nm and

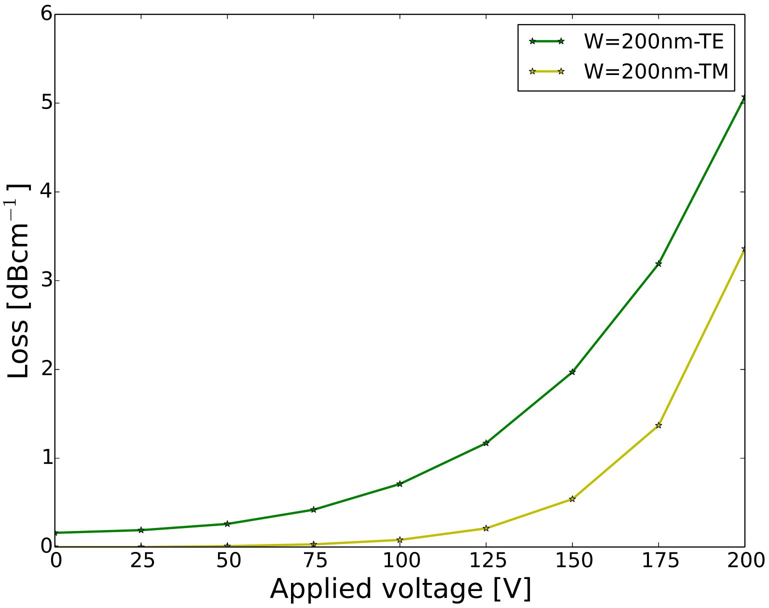

Figure 3.6: Variation of the loss of the fundamental TE and TM modes as a function of the applied voltage for a 200 nm wide waveguide.

220 nm respectively, the TM mode is now more tightly confined to the waveguide core than the TE mode. By increasing the applied voltage from 0 V to 200 V, the loss of the TE mode can be increased from 0.2 dB/cm to 5 dB/cm whereas that of the TM mode is increased from 0 dB/cm to 3.4 dB/cm.For this width we obtain a voltage tunable switch for both waveguide modes. For a narrower waveguide, we expect the loss tuning to be even more pronounced. In order to confirm this we take a look at the variation of the loss of the waveguide modes in an LC-clad 180 nm wide waveguide as a function of the applied voltage. This is shown in fig. 3.7. For this width the increase in the loss of the TE and TM modes is 20 times and 80 times larger than the previous case ($W = 200$ nm) respectively. The TE mode is way lossier than the TM mode, it is already in cut-off, with a loss of 56 dB/cm, for no applied voltage. On the other hand, the loss of the TM mode can be increased from 0.4 dB/cm to 52.4 dB/cm by increasing the applied voltage from 0 V to 200 V.

3.5 Conclusion

Deep-etched silicon waveguides are the basic building block of various photonic integrated circuits. The high index contrast that exists between the waveguide core and its cladding, makes it possible to have sub-micron devices with tight bends. The deep-etched waveguides used in integrated photonic devices are typically 450 nm wide and 220 nm high. Such a waveguide supports the fundamental TE and TM modes with distinct effective indices. We show that when such a waveguide is LC-clad, the effective indices of its modes can be tuned by

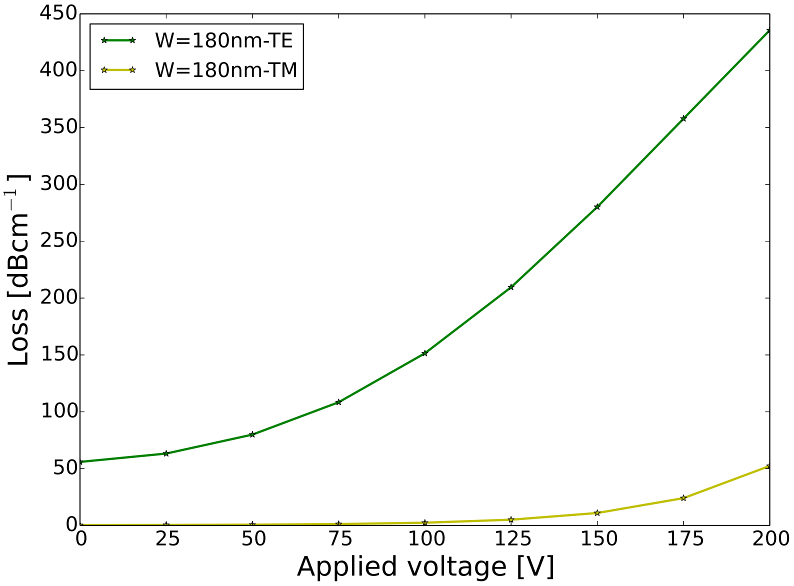

Figure 3.7: Variation of the loss of the fundamental TE and TM modes as a function of the applied voltage for a 180 nm wide waveguide.

reorienting the director of the LC. The tuning of the waveguide modes can be used to obtain devices with voltage controlled cut-off. This is only possible for waveguides which are narrow, with a considerable amount of light in the cladding, ensuring the interaction between the waveguide mode and the LC cladding is enhanced. This increased interaction results in an increased loss for the waveguide mode. The simulations we perform show that for a 200 nm wide waveguide the loss of the TE and TM modes is increased by 5 dB/cm and 3.3 dB/cm respectively by increasing the voltage applied over the LC from 0 V to 200 V. We also show that for a 180 nm wide waveguide, the TE mode is useless since its loss exceeds 50 dB/cm for no applied voltage. However, for the TM mode the loss can be increased by 50 dB/cm by increasing the applied voltage from 0 V to 200 V. The simulations of loss tuning of narrow waveguides reported in this chapter are comparable to those reported by [9]. In the latter work, the authors experimentally demonstrate that 220 nm high narrow deep-etched waveguides do exhibit propagation losses comparable to the values obtained in our simulations. For example the TE mode of a 180 nm wide waveguide is shown to have a loss of 52 dB/cm. They proceed to show that this propagation loss can be controlled by depositing layers of amorphous titanium dioxide (TiO_2) onto the waveguide by atomic layer deposition. For this waveguide and for the TE mode, 20nm, 30nm and 50 nm thick TiO_2 layers deposited on the it result in propagation losses of 64 dB/cm, 68 dB/cm and 58 dB/cm respectively. However, our simulation results for the TE mode in a 200 nm wide waveguide do not match the experimentally reported values in [9]. The device proposed here is better since the loss can be controlled reversibly and dynamically with an applied voltage. The speed of the change in loss is determined by the LC switching and is expected to be in the millisecond range.

Bibliography

[1] P. De Heyn, D. Vermeulen, D. Van Thourhout, and G. Roelkens. *Silicon-on-Insulator All-Pass Microring Resonators Using a Polarization Rotating Coupling Section.* Photonics Technology Letters, IEEE, 24(14):1176–1178, July 2012.

[2] Dazeng Feng, Wei Qian, Hong Liang, Cheng-Chih Kung, J. Fong, B.J. Luff, and M. Asghari. *Fabrication Insensitive Echelle Grating in Silicon-on-Insulator Platform.* Photonics Technology Letters, IEEE, 23(5):284–286, March 2011.

[3] Karel Van Acoleyen, Wim Bogaerts, Jana Jágerská, Nicolas Le Thomas, Romuald Houdré, and Roel Baets. *Off-chip beam steering with a one-dimensional optical phased array on silicon-on-insulator.* Opt. Lett., 34(9):1477–1479, May 2009.

[4] K. Van Acoleyen, W. Bogaerts, and R. Baets. *Two-Dimensional Dispersive Off-Chip Beam Scanner Fabricated on Silicon-On-Insulator.* Photonics Technology Letters, IEEE, 23(17):1270–1272, Sept 2011.

[5] W. Bogaerts, S.K. Selvaraja, P. Dumon, J. Brouckaert, K. De Vos, D. Van Thourhout, and R. Baets. *Silicon-on-Insulator Spectral Filters Fabricated With CMOS Technology.* Selected Topics in Quantum Electronics, IEEE Journal of, 16(1):33–44, Jan 2010.

[6] Wout De Cort, Jeroen Beeckman, Tom Claes, Kristiaan Neyts, and Roel Baets. *Wide tuning of silicon-on-insulator ring resonators with a liquid crystal cladding.* Opt. Lett., 36(19):3876–3878, Oct 2011.

[7] Wout De Cort, Jeroen Beeckman, Richard James, F. Anibal Fernández, Roel Baets, and Kristiaan Neyts. *Tuning of silicon-on-insulator ring resonators with liquid crystal cladding using the longitudinal field component.* Opt. Lett., 34(13):2054–2056, Jul 2009.

[8] Hans Desmet, Wim Bogaerts, Artur Adamski, Jeroen Beeckman, Kristiaan Neyts, and Roel Baets. *Silicon-on-insulator optical waveguides with liquid crystal cladding for switching and tuning.* volume 3, pages 430 – 431, 2003.

[9] T. Alasaarela, D. Korn, L. Alloatti, A. Säynätjoki, A. Tervonen, R. Palmer, J. Leuthold, W. Freude, and S. Honkanen. *Reduced propagation loss in silicon strip and slot waveguides coated by atomic layer deposition.* Opt. Express, 19(12):11529–11538, Jun 2011.

4

Slot Silicon Waveguides

4.1 Introduction

This chapter is based on the master thesis work of Mr. Yufei Xing [1]. Efficient low-loss on-chip phase shifters are important components necessary for future photonic integrated circuits built on the SOI platform. Previous attempts at realizing phase shifters or modulators in SOI employed the thermo-optic effect of silicon [1]. However, we recall from the opening chapter of this book that thermo-optic silicon devices have a limited speed and tuning range and require a constant power supply. An alternative method involves inducing a phase change by modulating the density of free carriers [2]. Although this approach yields fast modulation, it has its drawbacks; high power consumption and constant current flow or long device lengths depending on the biasing scheme used.

The preceding two chapters discuss the use of an LC upper cladding to modulate the loss of shallow-etched and deep-etched silicon. In both cases, in addition to modulating the loss, the switching of the LC also induces a phase change since it causes a change in the effective index of the waveguide modes. However, since most of the light is confined in the waveguide core, the waveguide modes do not fully 'feel' the index change that occurs in the LC. In contrast to the other waveguides investigated so far in this thesis, the dominant field component (E_x) of

---

[1] This chapter is partially based on the following papers:

1. Yufei Xing, Thomas Ako, John George, Dietmar Korn, Hui Yu, Peter Verheyen, Marianna Pantouvaki, Guy Lepage, Philippe Absil, Christian Koos, Juerg Leuthold, Jeroen Beeckman, Wim Bogaerts, ***Digitally controlled phase shifter using a silicon slot waveguide with liquid crystal infiltration.*** IEEE PHOTONICS TECHNOLOGY LETTERS Vol. 27. Jun. 2015.
2. Yufei Xing, Thomas Ako, John George, Dietmar Korn, Hui Yu, Peter Verheyen, Marianna Pantouvaki, Guy Lepage, Philippe Absil, Christian Koos, Juerg Leuthold, Jeroen Beeckman, Wim Bogaerts, ***Direct digital control of an efficient silicon+liquid crystal phase shifter.*** 11th International Conference on Group IV Photonics (GFP), France, p.43-44 (2014).

the TE mode in slot waveguides is concentrated in air rather than silicon (see fig. 4.1). We recall that this is a consequence of the fact that the E_x component experiences large discontinuities at the boundaries between the slot and the silicon arms/rails. Consequently, the waveguide mode 'feels' the full change in refractive index that occurs in any material that fills up the slot. When this filling material is an LC, then the effective index of the waveguide modes can be tuned by reorienting the LC with a low applied voltage. Compared to the other types of waveguides considered earlier in this thesis, the change in effective index is larger for slot waveguides. In order to further motivate this point, we compare simulations of the refractive index change that occurs in various types of LC clad waveguides studied in this thesis. First, we consider the change in the effective index of the fundamental TE mode in a conventional 450 nm wide, 220 nm high LC clad deep-etched waveguide. The reorientation of the LC varies from being aligned along (V_{low}) the waveguide to being aligned perpendicularly (V_{high}) to the waveguide's top surface. Second, we consider the change in the effective index of the fundamental TM mode in a 780 nm wide ($t_1 = 220$ nm, $t_2 = 150$ nm) shallow-etched waveguide. The reorientation of the LC once more varies from being aligned along (V_{low}) the waveguide to being aligned perpendicularly (V_{high}) to the waveguide's top surface. Finally, we consider a slot waveguide with 221 nm wide, 220 nm high arms. The silicon (for connection to electrodes in a real device) on the outer side of each arm is only 55 nm high. The slot gap is 110 nm wide and the LC reorients from being parallel (V_{low}) to being perpendicular (V_{high}) to the slot side walls respectively. In all three cases, the operating wavelength is 1550 nm. The various effective indices are put together in table 4.1. We note that the change in effective index of the slot waveguide is 80 $\%$ and 6 times larger than that in shallow-etched and deep-etched waveguides respectively. The larger change in effective index means for equal device lengths, there is a larger retardation between the signal at V_{high} and that at V_{low} for a slot waveguide. A device in which these two signals interact actively should constitute an excellent phase shifter. As such, an LC infiltrated slot waveguide used in a Mach-Zhender interferometer (MZI) configuration is an efficient phase shifter. Such a device has been shown to have outstanding performance with low power consumption and a voltage-length product of only $V_{\pi} \cdot L = 0.085$ Vmm [3]. In what follows, we explore a similar phase shifter made of LC infiltrated slot waveguides arranged in a MZI configuration and show that our device performs better with a voltage-length product of $V_{\pi} \cdot L = 0.022$ Vmm. The device's design and fabrication as well as characterization are explained. We then proceed further to compare its performance with related works and conclude with perspectives for future work.

	V_{low}	V_{high}	Δn_{eff}
deep-etched (TE)	2.379	2.366	0.013
shallow-etched (TM)	2.036	1.988	0.048
slot (TE)	2.053	1.967	0.086

Table 4.1: Comparison of the change in effective index for various types of LC clad waveguides. The operating wavelength is 1550 nm and the LC E7 ($n_o = 1.5024$, $n_e = 1.697$) is used.

4.2 Design and fabrication of the device

In order to ensure low operating voltages, the slot waveguides are not etched completely on their outer side. A thin silicon strip is used to connect the arms of the slot waveguide to electrodes. Accordingly, instead of having a voltage drop over a large area, a voltage drop is only present over the slot. Since the slot is narrow ($\sim$ 150 nm), the electric field in the slot can be very high even for low voltages. This means the LC filling the slot can be switched fully for small applied voltages. Following design at the Karlsruhe Institute of Technology, the waveguides are fabricated at IMEC. They are defined on a silicon wafer with a 2 μm thick box oxide (silicon dioxide) layer and a 220 nm thick active silicon layer. The arms of the waveguide are 220 nm high. On the outer side, the silicon is etched so that it is only 70 nm thick. This 70 nm thick rail of silicon connects the slot waveguide rails to the electrodes. The whole structure of the waveguides is covered with a 1 μm thick silicon dioxide top cladding. The slot is accessed by locally etching (dry etch + buffered HF etch) away the silicon dioxide cladding. This opens up the slot but also results in an undercut of the buried oxide layer under the waveguide. A scanning electron micrograph (SEM) picture of the geometry of the fabricated waveguide without LC is shown in fig. 4.1.

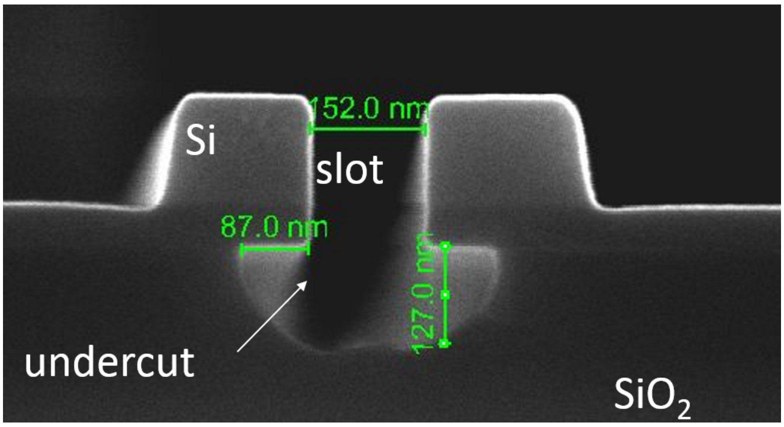

Figure 4.1: SEM picture of the fabricated strip loaded slot waveguide. The undercut resulting from the etching to open up the slot is clearly visible.

In keeping with the treatment in chapters 2 and 3, the finite element based mode solver of COMSOL multiphysics is used to simulate the modes of the waveguide whereas the LC orientation is simulated using another finite element based solver based on the Q-tensor formalism. The E_x component of the fundamental TE mode of the LC clad waveguide is shown in fig. 4.2. The optical properties of the LC E7 ($n_o = 1.5024$, $n_e = 1.697$) are used in the simulation. As expected, the field intensity is very high inside the slot, ensuring the waveguide mode feels the full change in the refractive index of the LC.

We then proceed with the simulation of the LC orientation inside the slot. This is important to determine the voltage at which we have complete reorientation of the LC. The elastic ($K_{11} = 12$ pN, $K_{22} = 9$ pN, 19.5 pN) and dielectric ($\varepsilon_{\|} = 19.6$, $\varepsilon_{\perp} = 5.1$) constants of E7 are the most important inputs in this step. We start with the 0V case; in this state the LCs find it energetically favourable to be are oriented parallel to the slot sidewalls [4]. The simulation result for this case

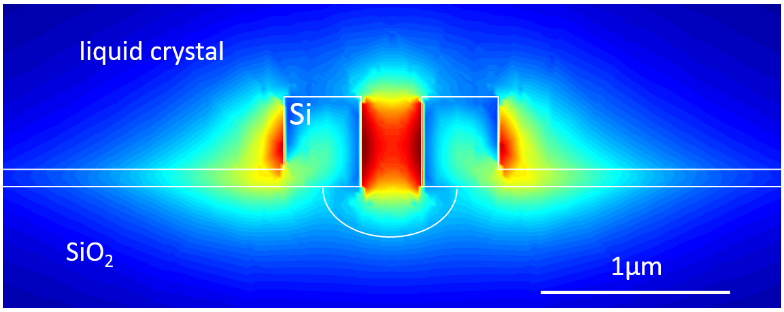

Figure 4.2: E_x component of the TE mode of the slot waveguide. We note the high field intensity inside the slot.

is shown in fig. 4.3.

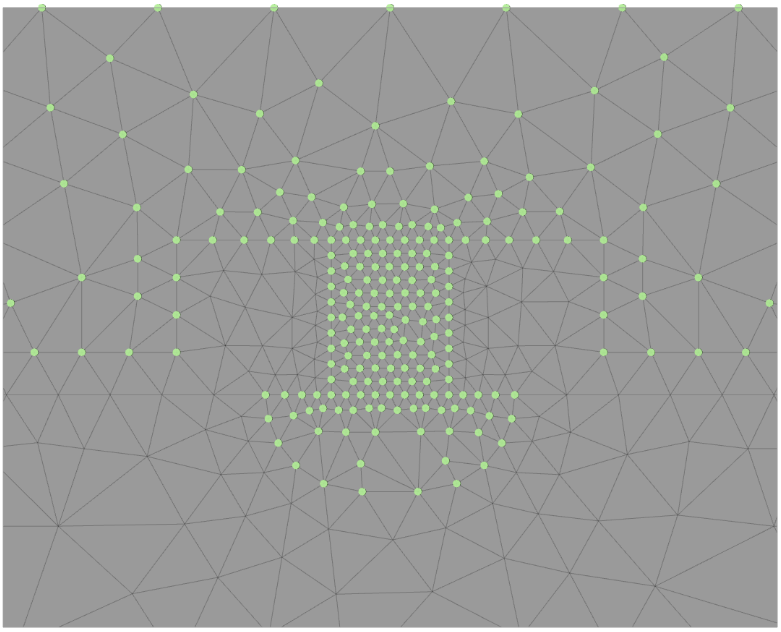

Figure 4.3: Orientation of the LC inside the slot and undercut for 0V.

It is found that the LC is already fully reoriented for an applied voltage of 2V as shown in fig. 4.4. The reorientation and hence change in the effective index (Δn_{eff}) of the waveguide mode is strongly dependent on the anchoring energy of the LC at the slot waveguide side walls. The anchoring energy of a surface determines the ease with which the LC reorients in response to an applied voltage. Fig. 4.5 shows how the effective index of the TE waveguide mode varies with the applied voltage for three types of anchoring. For weaker anchoring the increase in n_{eff} is sharp and saturates for voltages as low as 2.5V. For strong anchoring we have a more gradual increase in n_{eff}. The overall increase in n_{eff} is about 0.05.

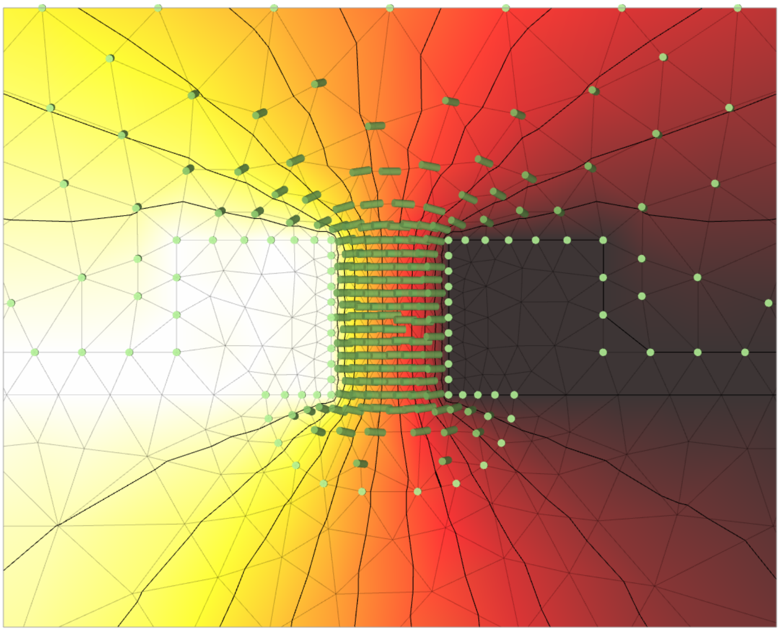

Figure 4.4: Orientation of the LC inside the slot and undercut for 2V. The background colour is the electric potential.

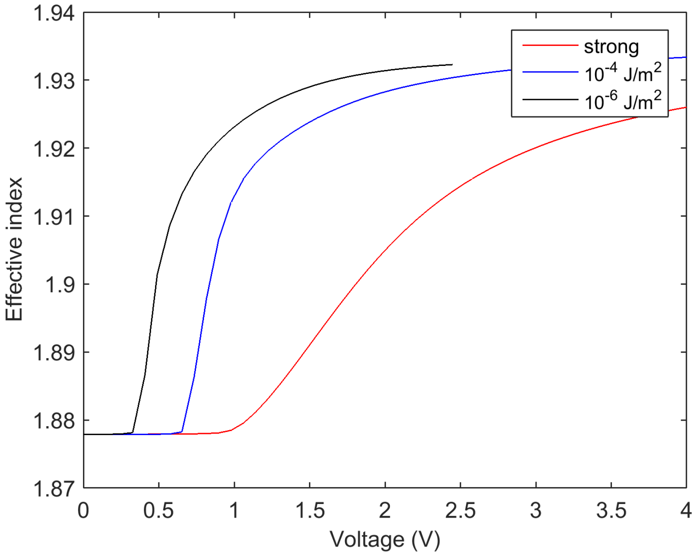

Figure 4.5: Variation of the effective index of the fundamental TE mode with the applied voltage over the LC for various anchoring strengths. For weaker anchoring strengths, the effective index increases faster and saturates.

4.3 Characterization results

The finished phase shifters are experimentally characterized in the INTEC laboratories at UGent. Grating couplers are used to couple light into and out of the slot waveguides. Light is brought to the chip through optical fibers placed close to the grating couplers. A drop of LC is deposited close to the waveguides, the LC automatically fills up the slot by capillary action. We do not directly check if the slot is completely filled or not. However, the measurement results indirectly indicate that this is the case. Electrical probes are used to contact the arms of the slot waveguide in order to bias the LC. Each arm of the MZI is a phase shifter made of an LC clad slot waveguide; one arm is kept at ground, while a voltage is applied over the other arm. In order to avoid charge separation in the LC, it is driven by an AC voltage. The AC voltage has a frequency varying between 30 KHz and 1 MHz; within this frequency range the LC can still respond to the driving signal.

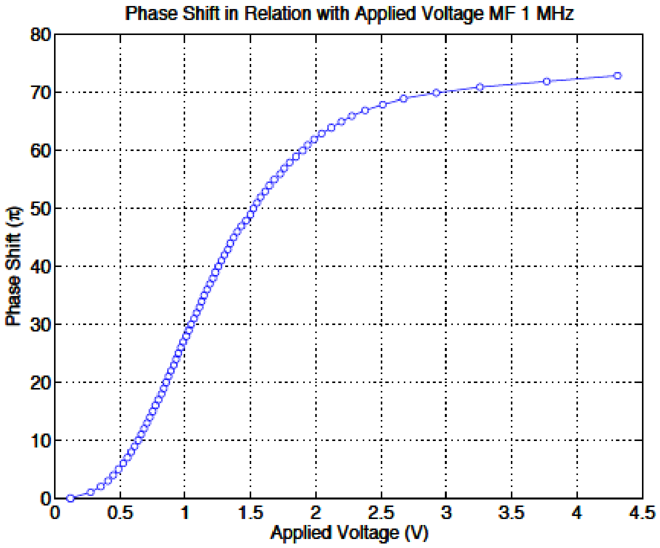

Figure 4.6: Variation of the phase shift with the applied voltage for our 1mm long phase shifter. Overall, we achieve a phase shift of 73π for an applied voltage of 5V.

The on-chip insertion loss of the phase shifter is -11 ± 1 1dB and the loss of the 1mm long phase shifter is estimated to be equal to -10 ± 1 dB. We sweep the AC voltage from 0V to 5V for a period of 0.5 seconds and observe the resulting intensity modulation of the signal from the output of the MZI. We extract the phase response by counting the number of peaks (corresponding to $0 \cdot \pi$ phase difference) and troughs (corresponding to $1 \cdot \pi$ phase difference). The phase shift increases with increasing applied voltage and saturates around 5V, indicating that the LC is completely reoriented at this voltage. Overall a phase shift of 73π is achieved for an applied AC voltage varying from 0V to 5V. The variation of the phase shift (in multiples of π) with the applied voltage is shown in fig. 4.6.

It is also interesting to look at the phase modulation efficiency of our device. This is the π phase shift per unit volt plotted as a function of voltage. This is plotted in fig. 4.7. The

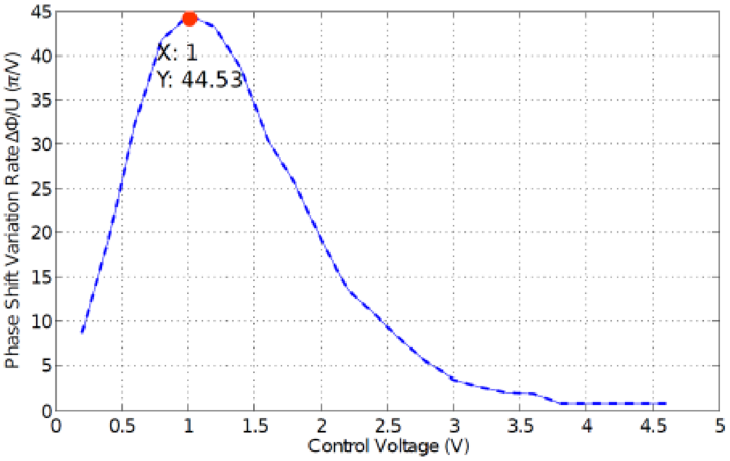

Figure 4.7: Modulation efficiency of our phase shifter as a function of the applied voltage.

maximal modulation efficiency is equal to 44.5 π/V and occurs at an applied voltage of 1V. This corresponds to a voltage-length product of $V_\pi \cdot L = 0.022$ Vmm. This is a factor of 4 better than the result of [3] where a maximal modulation efficiency of 20 π/V occurring at 1.3V and corresponding to a voltage-length product of $V_\pi \cdot L = 0.085$ Vmm is reported. This difference is down to the fact that the slot in [3] is not completely opened up, so part of the concentrated field of the waveguide mode in the slot does not 'feel' the refractive index of the LC. Consequently, the change in effective index and hence maximal modulation efficiency and voltage-length product are not as pronounced as in our case.

Two important figures of merit which need to be determined for our device are its speed and power consumption. Measurements reveal that the speed of our phase shifter is in the millisecond range as expected for LC devices [5], with switch-on and switch-off times in the range 1.4 ms and 2.5 ms. Tricks like overdriving [6] can be used to speed up the LC switching and reduce the switching time to the sub-millisecond regime but this results in a device which is difficult to control. On the other hand, the power consumption of the device is quite difficult to measure. The LC filled slot is essentially a capacitor; i.e. a dielectric (the LC) sandwiched between two conducting plates (the arms of the slot waveguide). The power consumption can be deduced by determining the power consumed by the charging of this capacitor. Following this approach, an upper limit of 2 nW is obtained for the power consumption.

Finally, given the excellent modulation efficiency obtained at low voltages, digital control of the phase shifter is investigated. Pulse width modulation (PWM) and frequency modulation (FM) are studied. It is found out that the phase shift is roughly linearly dependent on the pulse duration cycle (PWM) and the carrier frequency (FM) respectively. This indicates that digital control is an alternative control scheme for the device.

4.4 Discussion

The phase shifter presented here exhibits a record voltage-length product for a device based on silicon slot waveguides. There are other approaches used to achieve integrated on-chip phase shifters. For example, [7] report a 200 μm long silicon p-i-n modulator with a $V_\pi \cdot L = 0.36$ Vmm. Though, compact this device is less performant hence our proposal represents a step forward albeit for a longer device. Other approaches involve the use of slotted photonic crystal waveguides [8, 9], these type of devices are compact (sub 100 μm length) have low operating voltages ($\sim$ 1V). However, photonic crystal devices require advanced fabrication facilities. The only drawback of our device is its length. However in applications where only a limited number of multiples of π phase shift is required, a device identical to ours but shorter in length should provide an effective solution. For this shorter slot waveguide phase shifter, the phase shift response can be improved by using an LC with a larger optical anisotropy ($\Delta n = n_e - n_o$) than the one used here.

4.5 Conclusion

In this chapter, we have introduced LC clad silicon slot waveguides as a viable platform for on-chip photonic phase shifters. We have outlined the design and fabrication of the device and emphasized the key results derived from the experimental characterization carried out to test it. We record an excellent voltage-length product of $V_\pi \cdot L = 0.022$ Vmm; better than any previously reported figure for slot waveguide based phase shifters. The response time is typical of LC devices (millisecond range) and the power consumption is very low ($\sim$ nW).

Bibliography

[1] Joris Van Campenhout, William M. J. Green, Solomon Assefa, and Yurii A. Vlasov. *Integrated NiSi waveguide heaters for CMOS-compatible silicon thermo-optic devices*. Opt. Lett., 35(7):1013–1015, Apr 2010.

[2] Ansheng Liu, Richard Jones, Ling Liao, Dean Samara-Rubio, Doron Rubin, Oded Cohen, Remus Nicolaescu, and Mario Paniccia. *A high-speed silicon optical modulator based on a metal-oxide-semiconductor capacitor*. Nature, 427(6975):615–618, 02 2004.

[3] Joerg Pfeifle, Luca Alloatti, Wolfgang Freude, Juerg Leuthold, and Christian Koos. *Silicon-organic hybrid phase shifter based on a slot waveguide with a liquid-crystal cladding*. Opt. Express, 20(14):15359–15376, Jul 2012.

[4] Hans Desmet, Wim Bogaerts, Artur Adamski, Jeroen Beeckman, Kristiaan Neyts, and Roel Baets. *Silicon-on-insulator optical waveguides with liquid crystal cladding for switching and tuning*. volume 3, pages 430 – 431, 2003.

[5] Scott R. Davis, Scott D. Rommel, George Farca, and Michael H. Anderson. *A new electro-optic waveguide architecture and the unprecedented devices it enables*, 2008.

[6] Gregor Thalhammer, Richard W. Bowman, Gordon D. Love, Miles J. Padgett, and Monika Ritsch-Marte. *Speeding up liquid crystal SLMs using overdrive with phase change reduction*. Opt. Express, 21(2):1779–1797, Jan 2013.

[7] William M. Green, Michael J. Rooks, Lidija Sekaric, and Yurii A. Vlasov. *Ultra-compact, low RF power, 10 Gb/s siliconMach-Zehnder modulator*. Opt. Express, 15(25):17106–17113, Dec 2007.

[8] Jan-Michael Brosi, Christian Koos, Lucio C. Andreani, Michael Waldow, Juerg Leuthold, and Wolfgang Freude. *High-speed low-voltage electro-optic modulator with a polymer-infiltrated silicon photonic crystal waveguide*. Opt. Express, 16(6):4177–4191, Mar 2008.

[9] Jan Hendrik Wülbern, Jan Hampe, Alexander Petrov, Manfred Eich, Jingdong Luo, Alex K.-Y. Jen, Andrea Di Falco, Thomas F. Krauss, and J°rgen Bruns. *Electro-optic modulation in slotted resonant photonic crystal heterostructures*. Applied Physics Letters, 94(24):–, 2009.

5

Silicon High Contrast Gratings

5.1 Introduction

The propagation of light in periodic media results in interesting and useful phenomena. One of the most prominent examples of an application of these phenomena is a diffraction grating. A diffraction grating is an optical element which has a periodic variation of the refractive index. The periodicity of the refractive index can be one, two or three dimensional. When light is incident on a diffraction grating, its phase and amplitude are modulated by the periodicity of the latter. According to the Huygens-Fresnel principle, each point on the surface of a diffraction grating acts as a source when a plane wave is incident on it. Spherical waves emanating from each of these points then interfere with each other to form a diffraction pattern. Because of this property, diffraction gratings are usually used as dispersive elements in applications where it is necessary to filter certain wavelengths. Examples include spectrometers [1, 2], Bragg mirrors [3, 4], distributed feedback (DFB) lasers [5], distributed Bragg reflection (DBR) lasers [6, 7], fiber Bragg gratings [8, 9] and acousto-optic filters [10, 11].

Since the diffraction pattern is formed by interference of light coming from the sources in a grating, it exhibits maxima and minima. Incident and diffracted light waves are related by the well known grating equation;

$$\Lambda(\sin(\theta_{d,m}) - \sin(\theta_i)) = m\lambda. \tag{5.1}$$

Where Λ is the periodicity of the grating, $\theta_{d,m}$ is the angle of diffraction for the order m, θ_i is the incidence angle, m is an integer denoting the order of the diffraction, and λ is the wavelength of the light. Direct transmission through (or specular reflection from) the grating is the zero-order and corresponds to $m = 0$. The other orders (negative and positive m) correspond to diffraction on either side of the zero-order beam. All the angles mentioned above are with respect to the normal to the surface of the grating (see fig.5.1). Going back to (5.1), it is possible to deduce the necessary and sufficient condition for diffraction to occur for normal incidence.

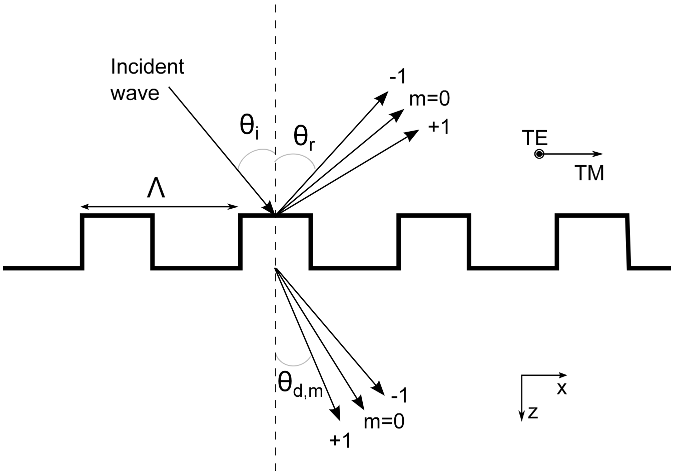

Figure 5.1: Sketch of a diffraction grating.

$$|\sin(\theta_{d,m})| < 1 \Longleftrightarrow \left| m\frac{\lambda}{\Lambda} \right| < 1 \tag{5.2}$$

From (5.2) it follows that the ratio of the wavelength of the incident light to the grating periodicity determines whether we have diffraction or not. Accordingly, we can deduce two main regimes of operation for diffraction gratings. These are the diffraction regime ($\Lambda >> \lambda$) and the deep sub-wavelength regime ($\Lambda << \lambda$).

An important example of a periodic layered device is the Bragg reflector. Fig.5.2 shows a Bragg reflector made up of alternating layers of high (n_H) and low (n_L) index materials. The spectral properties of a Bragg reflector are explained by the Bragg equation which is given by;

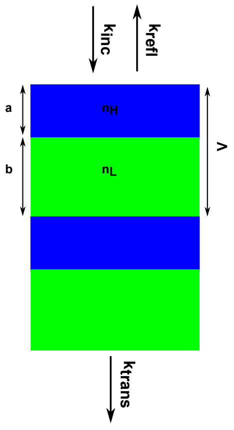

Figure 5.2: Sketch of a Bragg reflector.

$$m\frac{\lambda_B}{\bar{n}} = 2\Lambda \sin(\gamma) \tag{5.3}$$

With λ_B the Bragg wavelength, $\bar{n}$ the average refractive index over a single period Λ;

$$\bar{n} = \frac{a \cdot n_H + b \cdot n_L}{\Lambda} \tag{5.4}$$

a and b represent the thickness of the high and low index layers respectively. γ is the angle between the k-vector of the incident light beam and surface of the reflecting layers of the Bragg reflector. In a Bragg reflector the thickness of each layer is equal to a quarter of the design wavelength (λ) i.e.

$$a = \frac{\lambda}{4n_H} \tag{5.5a}$$

$$b = \frac{\lambda}{4n_L} \tag{5.5b}$$

When a plane wave is normally incident on a Bragg reflector, a reflection occurs at each interface between the different materials in it. The optical path length difference between reflections from each layer within one period is equal to half the wavelength. Additionally, the reflection coefficient for reflection at the interface of the different layers within one period have alternating signs. This causes constructive interference for all the reflected contributions from each period. Fig.5.3 shows the spectrum of an AlAs/GaAs Bragg reflector designed for a reflection centered at 1064 nm. As the number of periods is increased, the maximum reflection and the bandwidth of maximum reflection both increase.

This is expected since increasing the number of periods means we have an increase in the amount of reflected contributions. This is shown by the red, green and blue curves in fig.5.3. On the other hand, the yellow curve in fig.5.3 shows the spectrum for a Bragg reflector with a higher index contrast ($n_H = 3.49$ and $n_L = 2.75$) between the layers in each period. For a fixed number of periods, the bandwidth of high reflection can be increased (respectively decreased) by increasing (respectively decreasing) the index contrast between the layers in each period. These observations can be understood in terms of the diffraction efficiency of the Bragg reflector. Since the diffraction efficiency increases with increasing index contrast, a Bragg reflector with a higher index contrast achieves a given reflection with fewer periods. Analogously, a Bragg reflector with a lower index contrast can only achieve the same reflection if it has more periods. Consequently, high contrast Bragg reflectors are potentially more attractive for photonic applications due to their broadband high reflectivity. However, such gratings are usually obtained by epitaxial growth. Hence, the refractive index contrast between layers cannot be high due to lattice matching constraints. A grating with a strained lattice structure is more susceptible to the formation of lattice defects [12, 13]. Lattice defects destroy the symmetry of the layers and result in sub-optimal grating performance. In order to minimize lattice mismatch, materials with similar lattice constants (and hence low index contrast) are used in epitaxial growth of Bragg reflectors. Consequently, in applications where Bragg reflectors are employed e.g. as reflectors for VCSELs [14, 15], 40 to 50 periods need to be used. This results in a thick (5 μm) reflector which is challenging to manufacture and has a negative impact on the thermal relaxation of the VCSEL.

Given recent advances in nano-fabrication techniques, work has been carried out on a new type of grating capable of replacing Bragg reflectors. This is the so called high contrast grating

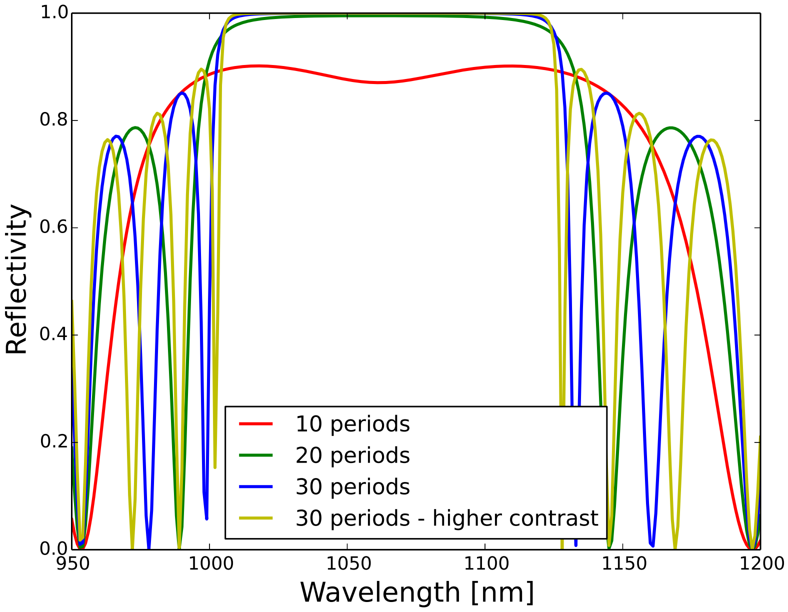

Figure 5.3: Reflection spectrum of an AlAs/GaAs Bragg reflector (red, green and blue curves) designed for 1064nm for an increasing number of periods. $n(GaAs) = 3.49$, $n(AlAs) = 2.95$, $a = 76$nm and $b = 90$nm. The yellow curve is for a Bragg reflector with higher index contrast ($\Delta n = 3.49 - 2.75$) between the layers in each period.

(HCG). HCGs are thin (hundreds of nanometers) gratings characterized by a high index contrast between the grating and its surroundings. In addition to broadband reflectivity (see fig.5.5), they also exhibit many properties which are of interest for photonics like narrow-band high quality resonances as well as polarization selectivity. They have already been used to replace DBRs in VCSELs. In this thesis, we study HCGs realized on the SOI platform. Such a HCG is depicted in the fig.5.4. The high index grating bars are made out of silicon and sit on a layer of silicon dioxide. This chapter is devoted to investigating the tunability of LC-clad HCGs.

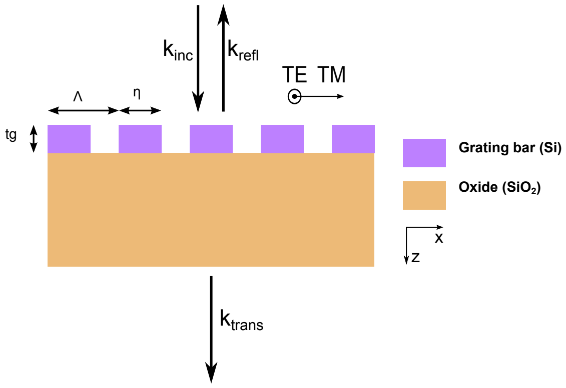

Figure 5.4: Sketch of a silicon HCG featuring its period (Λ), thickness (t_g) and fill factor(η). The drawing is not drawn to scale.

The chapter is arranged as follows, we start with an exploration of the physical origins of the novel properties of HCGs in section 5.2. In this section we also discuss the effect an LC cladding has on the properties of a conventional HCG. In section 5.3 we take a look at how to model HCGs. We use the finite element based multiphysics software package COMSOL Multiphysics to model the reflectivity of the HCGs. We model LC-clad HCGs by combining the LC simulation program introduced in section 2.3 and COMSOL. In section 5.4, we move on to explaining the practical details involved in designing air and LC-clad HCGs. In section 5.5 we briefly outline the fabrication steps necessary to obtain a HCG with an LC cladding. Finally, section 5.6 gives details about the reflectivity measurements of the fabricated HCGs. We compare the reflectivity measurements with simulations and deduce practical issues which must be taken into account to ensure optimal reflective performance.

5.2 Physics of broadband high reflection and high quality resonances

5.2.1 Air-clad HCG

The refractive index of the grating bars of a HCG is typically in the range $n_{bar} = 2.8 \sim 3.5$ whereas the index of the surrounding medium is usually air or some other low index material like silicon dioxide. A HCG is characterized by specific geometric parameters: period (Λ), thickness (t_g), and fill factor (η). The grating period is smaller than the wavelength in air ($\Lambda < \lambda$) but larger than the wavelength inside the grating bars ($\Lambda > \lambda/n_{bar}$). Accordingly, HCGs operate in

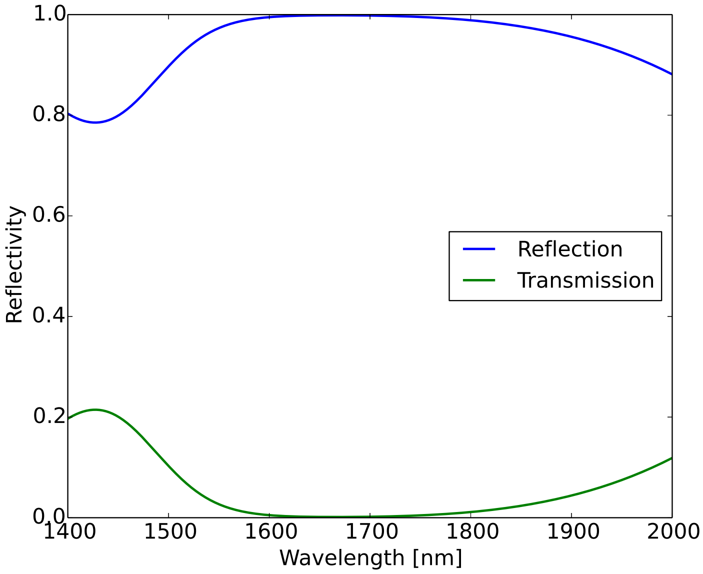

Figure 5.5: Simulation results for a HCG with broadband high reflectivity for TM polarized normally incident light using COMSOL multiphysics. The HCG has the following parameters; Λ =772 nm, t_g =1494 nm and $\eta = 70\%$.

the near-wavelength regime and are as such referred to as near-wavelength gratings. From (5.2) it follows that the near-wavelength regime is an intermediate regime between the diffraction ($\Lambda >> \lambda$) and sub-wavelength ($\Lambda << \lambda$) regimes. A grating operating in the diffraction regime has a low reflectivity since it mainly supports diffraction orders in the forward direction. Conversely, a grating operating in the sub-wavelength regime operates as a quasi-uniform layer.

The grating bars form a periodic waveguide array along the z direction. When a plane wave is incident on this waveguide array, a few waveguide array mode are excited. The number of excited modes and their nature depends on the incident wavelength, the polarization of the light and the grating parameters. The large index contrast and the near-wavelength dimensions of the grating mean there is a wide wavelength range within which exactly two waveguide array modes (the lowest order ones) have real propagation constants (i.e. carry energy) in the z direction [16–18].This is the so called dual-mode regime. In this regime, the other higher order waveguide array modes are in cut-off. As they propagate through the grating, the waveguide array modes accumulate a phase.They propagate from the grating input plane ($z = 0$) in the positive z-direction until they reach the grating output plane ($z = t_g$) where they reflect back up. They then propagate in the negative z-direction until they reach the grating input plane where they once more reflect back and so on. Due to the large index mismatch that exists between the grating and its surroundings, the two waveguide array modes couple to each other in addition to reflecting back to themselves. This does not contradict the orthogonality of the waveguide array modes since the reflection involves interaction with the modes of the regions adjacent to the grating region. Even though the waveguide array modes can couple to the the grating's surroundings (i.e. reflection(at $z = 0$) and transmission ($z = t_g$)), the near-wavelength period of the grating ensures only the zeroth diffraction order carries energy in reflection and transmission. Both are plane waves above and below the HCG respectively. A HCG derives its novel properties from its geometric parameters i.e. thickness, fill factor and period. However, the thickness is the most critical design parameter since it determines the phase accumulated by and the 'interference' of the waveguide array modes.

- **Broadband High Reflectivity:** An HCG exhibits high reflection if its thickness is such that the two waveguide array modes 'interfere' destructively at the grating output ($z = t_g$) plane. Destructive interference means the spatial overlap of both modes is zero at the grating output plane. Consequently, there can be no power coupled to the zeroth transmissive diffraction order and any light incident on the HCG is fully reflected. When this destructive interference condition is fulfilled for two relatively close wavelengths, there is a broadband reflection between both wavelengths.
- **High Quality Resonances:** An HCG exhibits high quality resonances if its thickness is such that the two waveguide array modes 'interfere' constructively at both the input and output grating planes. This results in a build up of energy inside the HCG. It functions as a high quality resonator.

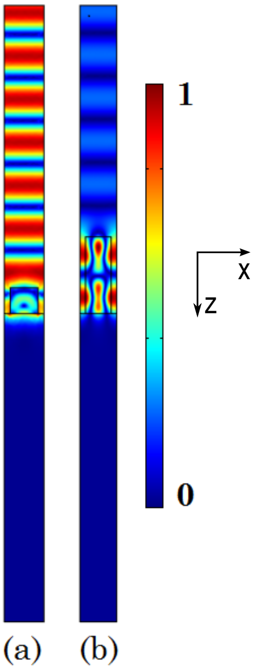

Figure 5.6: Electric field norm in a HCG for normally incident TM and TE polarized light. The color bar shows normalized field values. (a) HCG parameters: Λ =772 nm, t_g =502 nm and $\eta = 77\%$. The HCG bars have an index of 3.2137 and are in air. Field profile at λ =1680 nm. (b) HCG parameters: Λ =716 nm, t_g =1494 nm and $\eta = 70\%$. The HCG bars have an index of 3.48 and are in air. Field profile at λ =1680 nm.

Fig. 5.6 shows the electric field profile in a HCG for normally incident TM ((a)) and TE ((b)) polarized infrared light. For the TM case the field plot is done for a wavelength within the bandwidth of broadband high reflection whereas for the TE case it is done for a wavelength at which we have a high quality resonance. For TM polarization we observe that there is a higher intensity outside the HCG than inside it. On the other hand, for the TE case, we observe that the light is almost completely concentrated in the grating region, with very little light outside the HCG.

5.2.2 LC-clad HCG

In the previous section the origin of the striking reflective properties of air-clad HCGs was examined. We now turn our attention to understanding the properties of LC-clad HCGs. When an LC covers the upper part of a HCG, it infiltrates the space between the high index bars. The LC director can have many inhomogeneous orientations, the most interesting one are otientation perpendicular (x-axis), parallel (y-axis) or normal (z-axis) to the high index bars. These are depicted in fig.5.7. For x aligned LC, TM and TE polarized normally incident light feel the extraordinary (n_e) and ordinary (n_o) refractive index of the LC respectively. For y aligned LC, TM and TE polarized incident light feel n_o and n_e respectively. For z aligned LC, both polarizations feel n_o.

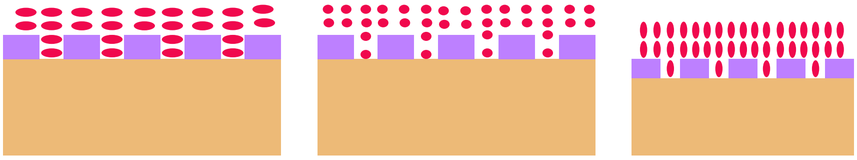

(a) LC along the x-axis (b) LC along the y-axis (c) LC along the z-axis

Figure 5.7: Various possibilities for orienting LCs above the HCG. The red ellipses denote LC molecules. The drawing is not to scale.

When a HCG has an LC cladding, incident light accumulates phase in the LC layer as well as in the HCG structure itself. Since the LC is anisotropic, this phase depends on the orientation of the LC director with respect to the polarization of the incident light. Even though the LC has a higher refractive index than air, the index contrast with respect to the HCG region is still high. As such, the Waveguide array modes propagating inside the HCG still encounter an abrupt refractive index change at the entry and exit surfaces of the HCG. Consequently, the waveguide array modes still reflect back into the HCG region and couple to each other as well. In this configuration, the phase accumulated by the waveguide array modes as they travel through the HCG now depends on the orientation of the LC as well as on its Λ, t_g and η. The Fabry-Perot resonance conditions responsible for the novel behavior of the HCG are now fulfilled for different wavelengths compared to the air-clad case. The broadband high reflectivity and high quality resonances are shifted to different wavelengths. Since the refractive index of the LC can be varied by reorienting the LC director, the reflective properties of an LC-clad HCG are tunable. Typically, the reorientation is achieved by applying a small voltage over the LC. The wavelength range of this tuning is proportional to the optical anisotropy ($\Delta n = n_e - n_o$) of the LC covering the HCG. Furthermore, since the LC is anisotropic, the tunability of the LC-clad

HCG is polarization selective. Tunable reflection of TM polarized incident light is achieved by reorienting the LC from being along the x-axis to being along the z-axis and vice-versa. On the other hand, tunable reflection of TE polarized incident light is achieved by reorienting the LC from being along the y-axis to being along the z-axis and vice-versa.

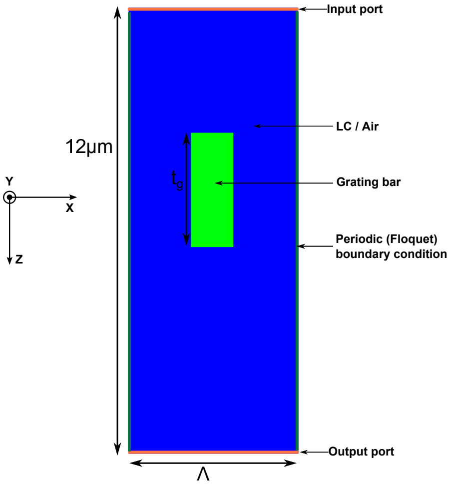

Figure 5.8: Simulation domain used for simulating the response of a HCG (in air) to normally incident TE (parallel to the high index bars) polarized light. The HCG has the following parameters; $\Lambda = 716$nm, $t_g = 1494$nm and $\eta = 70\%$.

Even though it is possible to tune both the TM polarized broadband high reflectivity and TE polarized high quality resonance of LC-clad HCGs, in practical situations, it is easier to achieve the latter than the former. The high quality resonances are narrow-band reflectivity peaks. A shift of this narrow peak is easily detected. In contrast, a shift in broadband high reflectivity is not easily detectable if the measurement setup does not span a very wide band of wavelengths. Additionally, in a practical device, the LC molecules tend to orient themselves parallel to the HCG bars, since this minimizes their free energy. Accordingly, we focus on tuning the TE polarized high quality resonances of HCGs in the rest on this chapter.

5.3 Modeling HCGs

This section is devoted to explaining the steps involved in modeling HCGs. We start with the air-clad case and proceed to the more complex LC-clad case. The reflectivity of the HCGs studied in this thesis is modeled with the commercial finite element based computational electromagnetics package COMSOL Multiphysics. We use the electromagnetic waves, frequency domain interface within the radio frequency (RF) module. The interface solves the electric field based time harmonic wave equation which is valid for linear materials. This is adequate for our purposes since we don't consider any non-linear effects. We simulate one unit cell of the grating, with a periodicity defined by Floquet boundary conditions. This condition requires that the solution on one side of the unit cell equals that on the other side multiplied by a complex-valued phase factor. Port conditions are used for specifying an incident wave and for

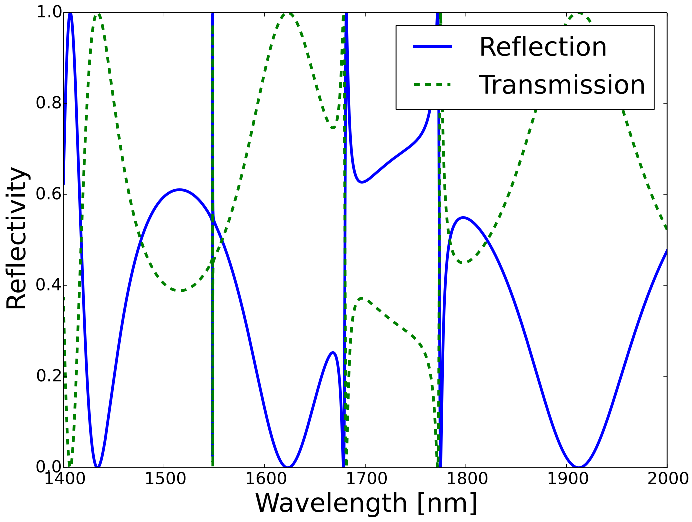

Figure 5.9: Simulation results for a HCG in air with high quality resonances for TE polarized normally incident light using COMSOL Multiphysics. The HCG has the following parameters; Λ =716 nm, t_g =1494 nm and $\eta = 70\%$.

allowing the solution to leave simulation domain without generating non-physical reflections. The input to the ports is an electric field vector and a propagation constant. Accordingly we can excite the input port with an appropriately polarized electric field and propagation constant. The interested reader is referred to the COMSOL user manual [19] for more details about the formulation used in the RF module. An example of the type of geometry used in simulations is shown in fig.5.8. This is only considered as an example, we use a HCG with different parameters later. For each wavelength, the reflectivity and transmission of the HCG is computed from the S-parameters of the ports. The reflection and transmission are obtained as the absolute value of the square of the S_{11} and S_{21} parameters respectively. The simulation results for a HCG with Λ =716 nm, t_g =1494 nm and $\eta = 70\%$ are shown in fig.5.9.

In order to simulate LC-clad HCGs, we integrate the simulation in COMSOL with the LC simulation introduced earlier in section 2.3. The geometry used for the LC simulation is identical to that in fig.5.8 with the exception that the ports are replaced by the top and bottom electrode for applying a voltage over the LC. The director is chosen to be initially planar aligned (parallel to the high index bars of the HCG) with a pre-tilt of 2° at the surface of the electrodes. The properties of the LC E7 are used in the simulation. We use strong anchoring conditions for the LC at the electrodes. At the surface of the HCG, we use weak anchoring with an anchoring energy of 10^{-4}Jm^{-2} for the LC. A visualization of the LC simulation results for various applied voltages is shown in fig.5.10. For voltages lower than the Fréederickz threshold voltage (V_{th}), the LC does not switch. When the applied voltage is equal to V_{th}, the LC starts to switch. The LCs reorient, becoming increasingly normal to the surface of the HCG, as the voltage increases above V_{th}. The refractive index distribution of the LC layer can be extracted from the LC solver. This refractive index distribution is imported into COMSOL, where it is used as the refractive index

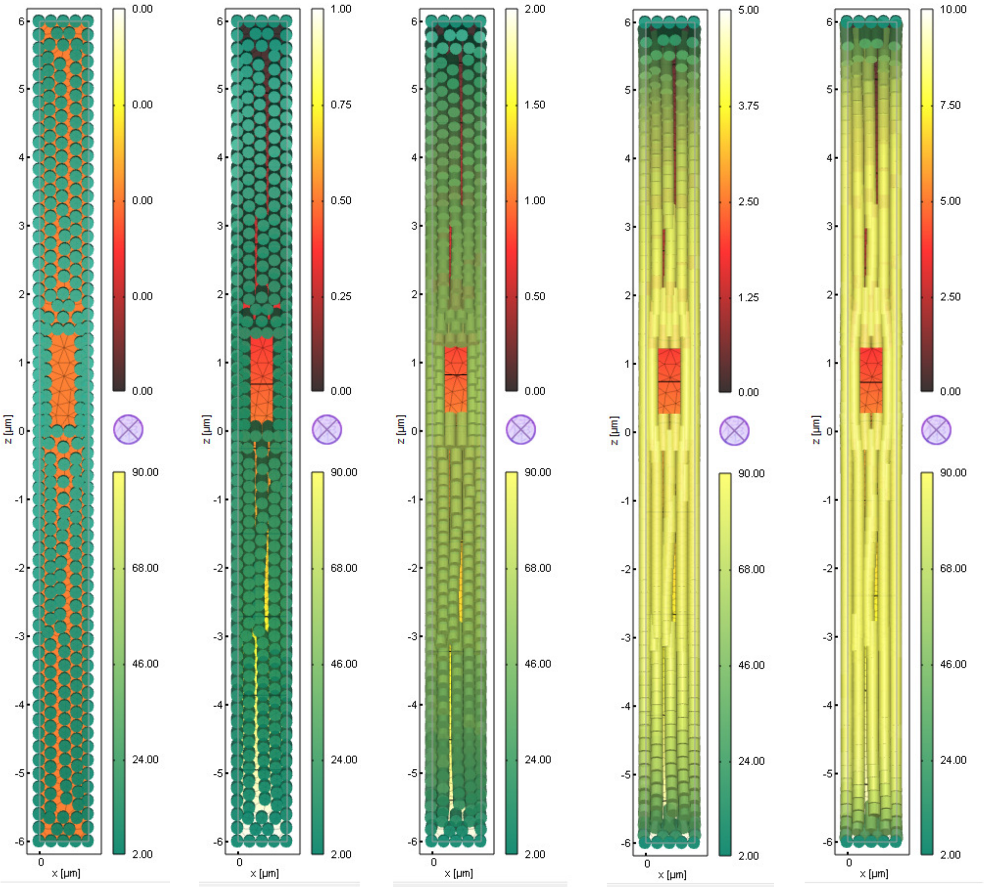

0V **1V** **2V** **5V** **10V**

Figure 5.10: Simulation of the LC orientation in an LC-clad HCG for increasing applied voltages. In each of the figures, the upper and lower color bars are for the applied voltage (V) and the tilt of the LC molecules (°). The LC molecules are shown as green cylinders. The HCG has the following parameters; Λ =716 nm, t_g =1494 nm and $\eta = 70\%$.

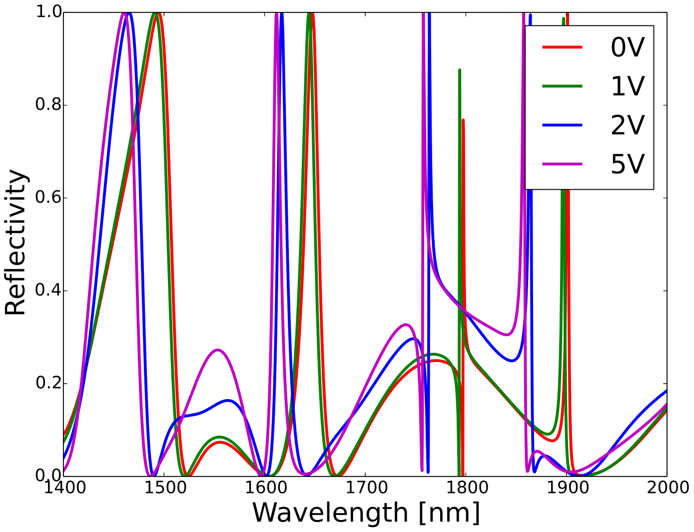

Figure 5.11: Simulation results for the reflectivity of an LC-clad HCG plotted as a function of the wavelength for varying applied voltages. The HCG has the following parameters; Λ =716 nm, t_g =1494 nm and $\eta = 70\%$.

for the material surrounding the HCG. The reflectivity can then be calculated just like for the air-clad HCG. The reflectivity curve corresponding to each applied voltage is shown in fig.5.11. For 0 V, the LC molecules are parallel to the high index bars of the HCG; normally incident TE polarized light feels an index n_e in the cladding of the HCG. Compared to the air-clad case, the reflectivity curve shifts to longer wavelengths for 0 V. As the applied voltage increases beyond V_{th}, the LCs reorient and the refractive index felt by the TE polarized light decreases. This causes the high quality resonances to shift to shorter wavelengths. By increasing the applied voltage from 0 V to 5 V, the high quality resonance peaks shift by about 40 nm.

5.4 Designing a HCG

In this thesis, we focus on HCGs 'written' on an SOI chip and working in the wavelength window between 1500 nm and 1700 nm. The chip has a 220 nm thick silicon layer which sits on a 2 μm thick buried oxide layer. The first step in the design is the determination of the optimal physical parameters (Λ, t_g, η) of the HCG.

- The search for the optimal value of the HCG period is guided by the condition for a near-wavelength grating i.e. the period of the grating must be larger than the wavelength inside the high index bars for the shortest wavelength incident on the HCG. In our case, $n_{silicon} = 3.48$ [20] and λ =1500 nm. This yields Λ_{min} =431 nm. The upper bound for the HCG period is the longest wavelength incident on the HCG.

- We are constrained by the fact that the thickness of the silicon layer and hence the thickness of the HCG is fixed at 220 nm. Therefore we have no freedom in this parameter.
- The fill factor of the HCG is the only parameter which has no constraint. However, accurate reproduction of the exact desired fill factor is determined by the lithographic processing through which the HCG is defined.
- The optimal parameters for the HCG are determined by doing parameter sweeps, using the constrained parameter values discussed above. We proceed by fixing the η of the HCG at an arbitrary value. Since the t_g is also fixed, this enables us to continuously vary the Λ in order to determine its effect on the reflectivity of the HCG. Next, we fix the Λ at a value within the near-wavelength regime and sweep the η. This results in the surface plots in fig.5.12. The optimal set of HCG parameters can then be extracted from these plots.

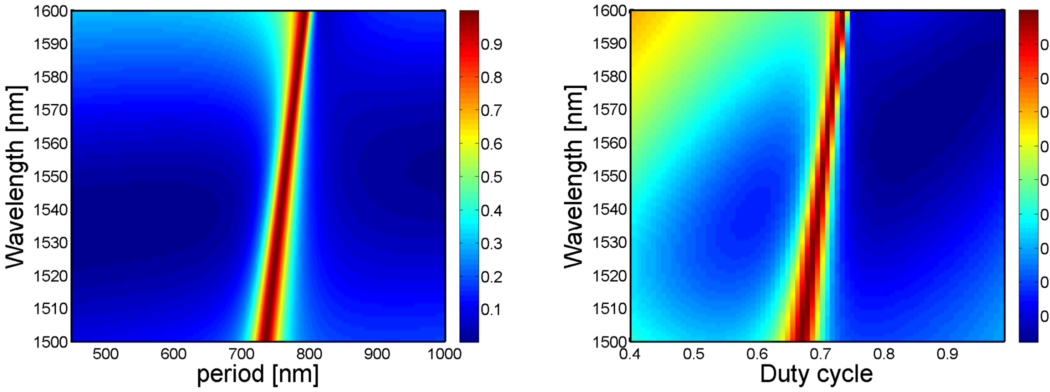

(a) HCG period

(b) HCG thickness

Figure 5.12: Determining the optimal Λ, t_g, and η of a HCG. Parameter sweeps for the Λ and the η. The color bar shows the magnitude of the reflectivity.

Following these simple design rules, we arrive at the following design. We design five HCGs with t_g =220 nm, $\eta = 70\%$ and Λ=764 nm, 768 nm, 772 nm, 776 nm, 780 nm. The HCGs have dimensions of 50 μm by 50 μm. In order to model the HCGs we use the geometry shown in fig. 5.13. The reflectivity of some of these HCGs for TE polarized normally incident light is shown in fig.5.14. The reflectivity for TM polarized light is also shown. We notice that at the reflection maxima, the TE reflection is at least thrice as strong as the TM reflection.

We now investigate what happens to the reflectivity of the HCGs when they are clad with LC. In order to achieve this, we replace the 6 μm thick air layer with LC. The alignment of the LC is chosen to be planar with a pre-tilt of 2° at the top electrode and at the surface of the chip. The silicon substrate acts as the second electrode of the device. Since we have a 2 μm thick oxide layer as well as an LC layer between the electrodes, higher applied voltages (compared to the example considered earlier) would be needed to reorient the LC. We expect the reflectivity maxima to shift to longer wavelengths for 0 V compared to the air-clad case.

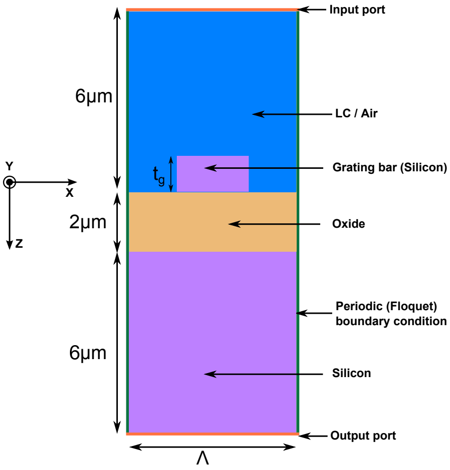

Figure 5.13: Rough sketch of the simulation domain used in COMSOL for a SOI HCG.

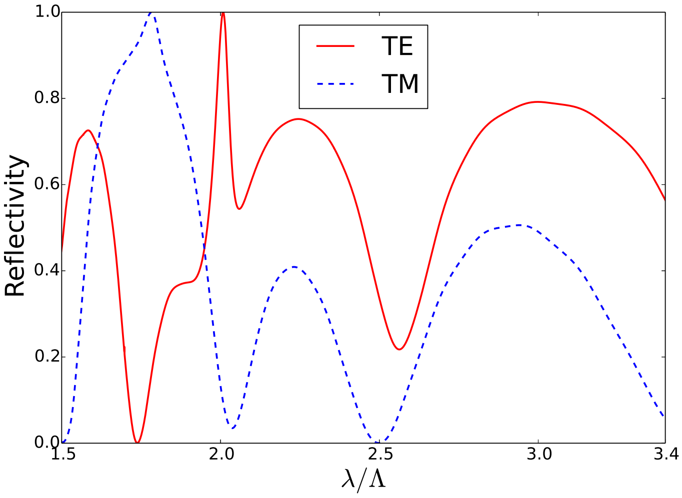

Figure 5.14: Reflectivity spectra for three of the HCGs (in air) for TE and TM polarized light. The HCGs have t_g =220 nm and $\eta = 70\%$.

As the applied voltage is increased beyond V_{th}, the LC molecules reorient more and more. The index felt by the TE polarized incident light decreases and the reflectivity maxima shift to shorter wavelengths. We consider the HCG with Λ =764 nm. The effect of the applied voltage on the reflectivity of the LC-clad HCG is shown in fig. 5.15. With no applied voltage, the reflectivity is shifted to longer wavelengths compared to the air-clad case. As the voltage is increased, the reflectivity curve shifts to shorter wavelengths due to the lower refractive index. By increasing the applied voltage from 0 V to 70 V, we tune the position of the reflection peak by more than 40 nm. So far we have performed simulations in order to arrive at a design for an LC-clad HCG which has desirable characteristics. In the next section, we explain the fabrication steps needed to obtain an LC-clad HCG.

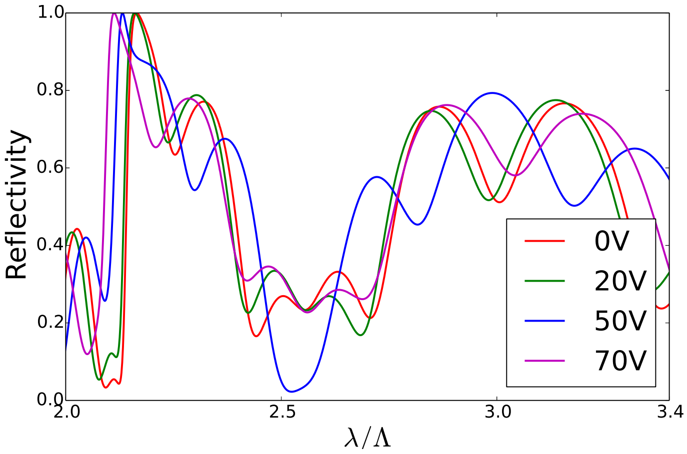

Figure 5.15: Reflectivity spectra for an LC-clad HCG. The HCG has Λ =772 nm, t_g =220 nm, and $\eta = 70\%$. The reflectivity spectra for different applied voltages are shown.

5.5 Fabrication of HCGs

We integrate the chip with the HCGs into LC cells in order to facilitate reorientation of the LCs by application of a voltage. The HCGs are fabricated on SOI chips following the specifications provided by the design in the previous section by the ePIXfab [21] multi-project-wafer runs at IMEC. The cell consists of the SOI chip (with the HCGs) and a top glass plate held together by UV curable glue. Spherical spacer balls mixed with the glue determine the cell gap. Since the HCGs are rather small, it is necessary to cut the glass plate to the appropriate size. The glass plate has a conductive layer of indium tin oxide (ITO) and a nylon alignment layer deposited on it. The ITO and the bottom of the chip are contacted electrically and make it possible to apply a voltage over the LC cell. The nylon alignment layer is rubbed such that the LC director has a planar alignment (with a pretilt of 2°) in a direction parallel to the HCG bars. This ensures TE polarized light incident on the HCG feels n_e and n_o of the LC for low and high applied voltages respectively. We fill the cell with the LC E7. A schematic of the finished HCG LC cell is shown in fig.5.16.

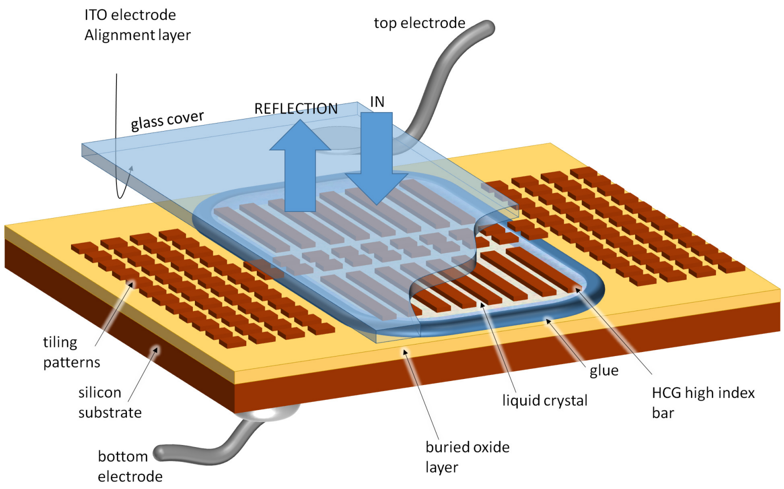

Figure 5.16: Schematic of an SOI chip with HCGs integrated into a LC cell. The sketch is purely illustrative given that it is not drawn to scale.

Following the fabrication of the LC cell, we proceed to investigate the alignment of the LC. The LC cell is observed with the polarization microscope in reflection mode under crossed polarizers. We make sure the rubbing direction of the alignment layer on the top glass plate is parallel to the polarizer of the microscope. Since the alignment at the top glass plate is planar and parallel to the HCG bars, the transmission in this configuration should be low for no applied voltage. However, we observe a change in transmission and color with increasing applied voltage. This indicates that there is some twist in the cell and that it is not thick enough to fulfill the Mauguin condition. Fig. 5.17(a) shows the HCGs for 0 V_{rms}. The area over the HCG is dark, indicating that the LC is uniformly aligned parallel to the HCG bars. As the applied voltage is increased, we observe that the LC over the HCG switches uniformly. This is deduced from their uniform color. This indicates that the LC reorients uniformly over the HCGs.

5.6 Characterization of the fabricated HCGs

In this section we turn our attention to the characterization of the air and LC-clad HCGs fabricated in the previous section. SEM pictures of one of the HCGs is shown in fig.5.18.

The SEM pictures reveal that the HCG bars are uniform along their length. However, the difference in period between the different HCGs (4 nm) is too small to be resolved by the lithographic fabrication steps. The five HCGs are identical except for some small fabrication defects. The cross section view (fig.5.18(b)) of the HCGs reveals them to be trapezoids rather than rectangles. The layers above and filling the space between the HCG bars in fig.5.18(b) are left overs of the processing required to obtain the cross section. Since the reflective properties of a HCG arise from the phase-matching and coupling of the waveguide array modes in it, HCGs with trapezoidal and rectangular shaped high index regions have different reflectivity spectra. We consider a concrete example of this; we simulate a HCG whose high index bars are

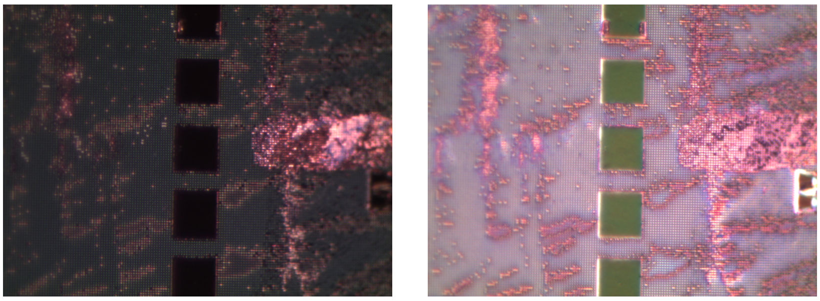

(a) 0V (b) 6.8V

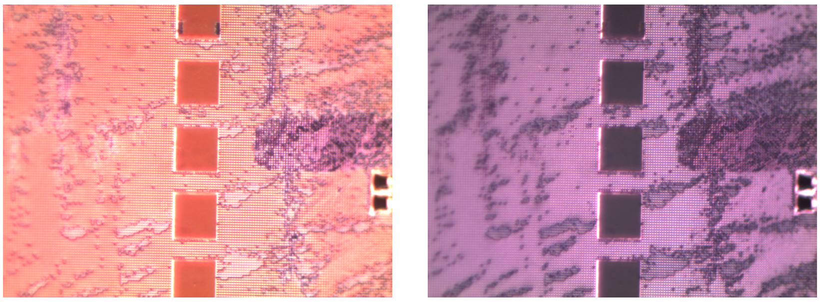

(c) 10V (d) 20V

Figure 5.17: LC cell with HCGs under crossed polarizers in reflection mode. The rectangles in the pictures are the HCGs. The background shows the dummy structures which surround the HCGs.

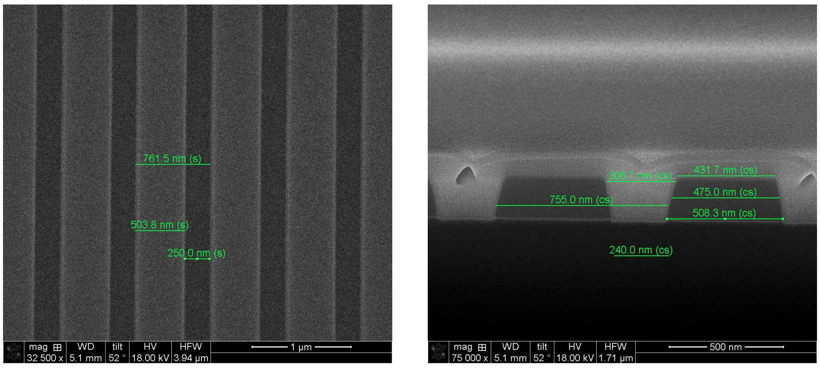

(a) Top view (b) Cross section

Figure 5.18: SEM pictures of an air-clad HCG fabricated on SOI. The target parameters for the HCG are $\Lambda = 764$ nm $\sim$ 780 nm, t_g =220 nm and $\eta = 70\%$

(isosceles) trapezoids. The dimensions of the parallel sides are 432 nm (top) and 508 nm (bottom) respectively and the perpendicular height (t_g) is 220 nm. The period is 748 nm. We compare the reflectivity of this trapezoidal HCG with that of a rectangular HCG which has the same period and fill factor ($\eta = 67.9\%$) i.e. its high index bars are 508 nm wide. This enables us to determine the effect of tapering at the top of the HCG bars. The reflectivity of both HCGs are compared for various types of cladding in fig.5.19.

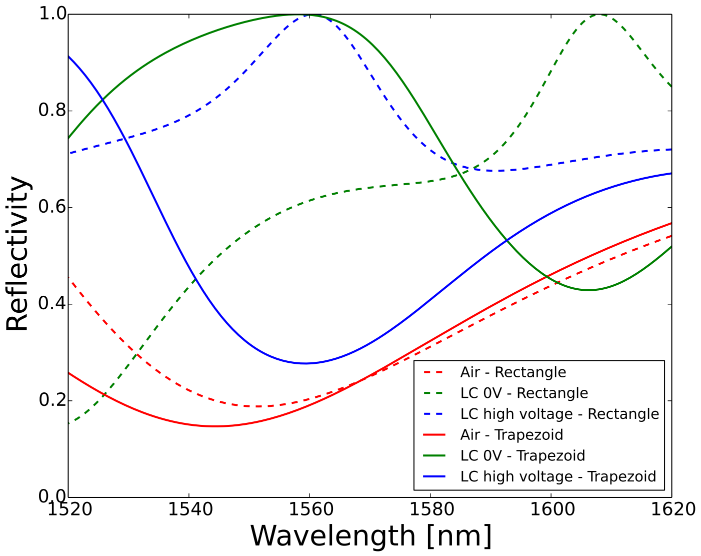

Figure 5.19: Comparison of trapezoidal and rectangular HCGs. The trapezoidal HCG has a Λ =748 nm, t_g =220 nm and its parallel sides are 432 nm (top) and 508 nm (bottom) long respectively. The rectangular HCG has Λ =748 nm, t_g =220 nm, and $\eta = 67.9\%$.

The dimensions used for the trapezoidal HCG above were extracted from fig.5.18(b). The reflectivity peaks for the trapezoidal HCG occur at shorter wavelengths compared to the rectangular HCG. The high quality resonance peaks of the trapezoidal HCGs are broader than those of the rectangular HCGs. However, the switching behavior is preserved. For LC aligned parallel to the HCG bars, the peak reflectivity shifts to longer wavelengths compared to the air-clad case. As the voltage applied over the LC increases beyond V_{th}, the reflectivity peak shifts to lower wavelengths. Interestingly, the reflectivity peak of the trapezoidal HCG falls well within the wavelength window of interest. Having understood the reflectivity of our trapezoidal HCGs, we move on to experimental measurements of their reflectivity.

5.6.1 Measurements of HCG Reflectivity

In order to measure the reflectivity of the HCGs fabricated earlier, we use a free-space setup at the Université Libre de Bruxelles (ULB). We use a fiber-coupled tunable laser source (OSICS) whose emission spans the wavelength window between 1500 nm and 1620 nm as the light source. The fiber output from the laser is directed at a 20x microscope objective. This turns the diverging beam from the fiber into a collimated beam. The laser beam then passes through a polarizing beam splitter (PBS), which is oriented such that it only transmits light polarized parallel to the HCG grating bars. Following this, the laser beam passes through a 50/50 beam splitter and falls on another 20x microscope objective which focuses it onto the HCGs on the chip. The chip is taped to a glass plate which is itself taped to an xyz stage. This makes it possible to easily move the chip in three dimensions. Light reflected from the HCGs passes through the 20x objective and then the 50/50 beam splitter. A neutral density filter controls the intensity of the laser light after the 50/50 beam splitter and a lens focuses this light onto the sensor of an InGaAs visible and IR camera. Since, the HCGs have quite small dimensions (50 μm x 50 μm) and the measurement is for IR light, it is necessary to track both the position of the HCGs and the laser beam. We achieve this by illuminating the chip with a white light source. White light is introduced into the setup by placing the output of its source in front of a lens facing one side of the PBS. Since the optical path length is different for the IR and visible wavelengths in the setup, a second (removable) lens is placed between the PBS and the 50/50 splitter to make sure the foci of both beams occur at the surface of the chip. A schematic of the measurement setup is shown in fig.5.20

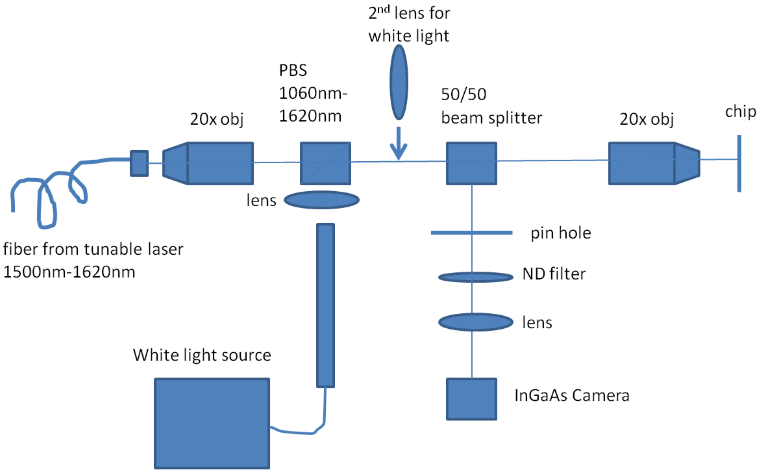

Figure 5.20: Schematic of the setup used to measure the reflectivity of the HCGs.

A measurement of the reflection of one of the HCGs is performed as follows;

- We make sure the laser is off and we turn on the white light source. We use the two lenses assigned for visible light and adjust the position of the chip until we get an image of the HCGs on the camera. The field of view of our rudimentary imaging system is such that we can observe two of the HCGs simultaneously.
- We then use the camera control software to draw the outline of the boundary of the HCG. The white light source is now turned off. The wavelength and power level of the laser are set, the lens used for focusing the white light is removed.
- The laser is turned on. Since we use two 20x microscope objectives between the fiber output of the laser and the chip surface, we can image the beam spot at the fiber output

onto the surface of the chip. The fiber is single mode, with a core diameter of about 10 μm, so we expect the beam to have a comparable size when the chip's surface is at its focal point. We now make sure the beam of the laser is positioned within the HCG boundary traced earlier.

- Without moving the chip, we turn off the laser and image the chip with visible light to ensure we are still on the HCG. Having done this, we turn off the white light source and switch the laser on again. We recall that in all simulations performed earlier, we always considered normal incidence. However, in our setup, the light reaching the chip is focused. In addition to the normal, we have light from several other angles falling on the HCG. We place a pin hole between the lens (in front of the camera) and the neutral density filter to select a small cone of angles around the center of the reflected beam.
- The light passing through the pinhole is collected by a lens and focused on the camera's sensor. We can then read out the intensity of the reflection from the HCG. Since we need to set the wavelength manually, we measure all five HCGs in sequence, always starting from the same direction (the bottom).
- We also measure the reflectivity just outside the HCGs (at the top and bottom), and normalize each measurement with the average of these two measurements. We repeat this procedure, performing 7 (five HCG and two normalization) measurements for each wavelength. We perform measurements at 10 equally spaced wavelengths within the wavelength range from 1520 nm to 1620 nm.
- In order to tune the reflectivity of the LC-clad HCGs, we use a function generator to apply a sinusoidal 1KHz AC voltage to the cell. For each voltage we perform 7 measurements for each of the 10 wavelengths.

We start our analysis of the measurement data with the measurement of the reflected intensity from one of the LC-clad HCGs as a function of the applied voltage. This is shown for three different wavelengths in fig.5.21. The intensity of the reflection of the HCG shows a rather unexpected dependence on the applied voltage.

- **1550nm:** At 0 V_{rms} the reflection is high, as the voltage increases, the reflection decreases until it attains a minimum at 13 V_{rms}. As the voltage is increased further, the reflection increases again, attaining a maximum at 20 V_{rms}. From here it decreases to a second minimum at 30 V_{rms} and proceeds to attain another maximum in reflection 45 V_{rms}.
- **1580nm:** At 0 V_{rms} the reflection is low, as the voltage increases, the reflection increases until it attains a maximum at 13 V_{rms}. As the voltage is increased further, the reflection decreases, attaining a minimum at 20 V_{rms}. From here it increases to a second maximum at 30 V_{rms} and proceeds to attain a another minimum in reflection 45 V_{rms}. Between 45 V_{rms} and 67 V_{rms}, the reflection increases.
- **1610nm:** At 0 V_{rms} the reflection is low, as the voltage increases, the reflection decreases until it attains a minimum at 13 V_{rms}. As the voltage is increased further, the reflection increases again, attaining a maximum at 20 V_{rms}. From here it decreases to a second minimum at 30 V_{rms} and proceeds to attain a another maximum in reflection 45 V_{rms}.

The maxima and minima in reflected intensity are coincident for 1550 nm and 1610 nm. The maxima and minima in reflection for 1580 nm are opposite to those for 1550 nm and 1610 nm. The simulations show that the reflectivity curve of LC-clad HCGs shifts to shorter wavelength when the applied voltage is increased. This behavior is confirmed by the measurement. For example, the reflection at 0 V$_{rms}$ for 1580 nm is low. It corresponds to the reflection for 1550 nm just after its first minimum i.e. around 13 V$_{rms}$. Additionally, the first reflection maximum for 1580 nm occurs 13 V$_{rms}$. It corresponds to the second reflection maximum for 1550 nm at 20 V$_{rms}$.

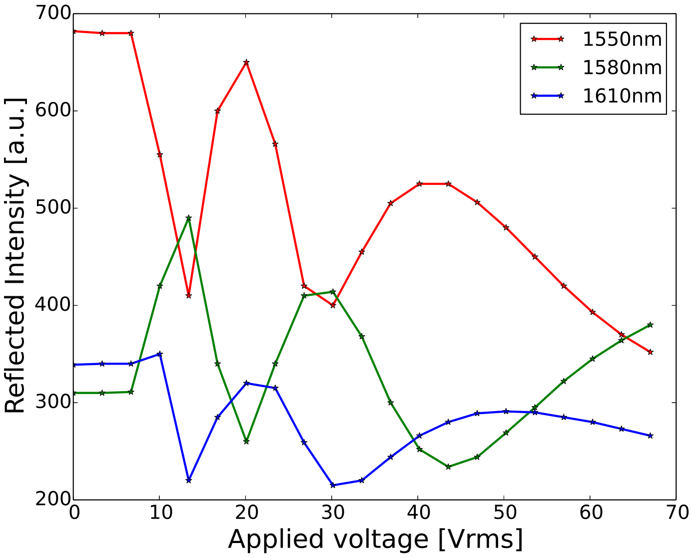

Figure 5.21: Measurement data for the reflected intensity of an LC-clad HCG as a function of the applied voltage.

The result of the reflectivity measurement for the air-clad HCGs are shown in fig.5.22. The measurement confirms the observations made with the SEM. The reflectivity curves are all very similar, indicating that the HCGs all have similar dimensions. The measurement results are similar to the simulation results for the reflectivity of an air-clad trapezoidal HCG (see fig. 5.19). It exhibits a minimum within the wavelength window considered in the measurement. This confirms that the HCGs are indeed trapezoids. The reflected intensity for the LC-clad HCGs are shown for 0 V$_{rms}$ (fig.5.23), 20 V$_{rms}$ (fig.5.24) and 67 V$_{rms}$ (fig.5.25).

Overall, the reflectivity shifts to shorter wavelengths with increasing applied voltage. For 0 V$_{rms}$, the reflectivity of the LC-clad HCGs has a reflectivity peak close at 1590 nm. When the applied voltage is increased to 20 V$_{rms}$, the reflectivity peak shifts to 1580 nm. For an applied voltage of 67 V$_{rms}$, we notice another reflectivity peak around 1610 nm. The original reflectivity peak shifts to 1530 nm for this voltage. The magnitude of the reflectivity exceeds unity for one of the LC-clad HCGs with no applied voltage. For an applied voltage of 20 V$_{rms}$, the reflectivity of the HCGs exceeds unity in the wavelength range between 1550 nm and 1590 nm. This makes it difficult to accurately quantify the tuning range of the reflectivity peaks of the

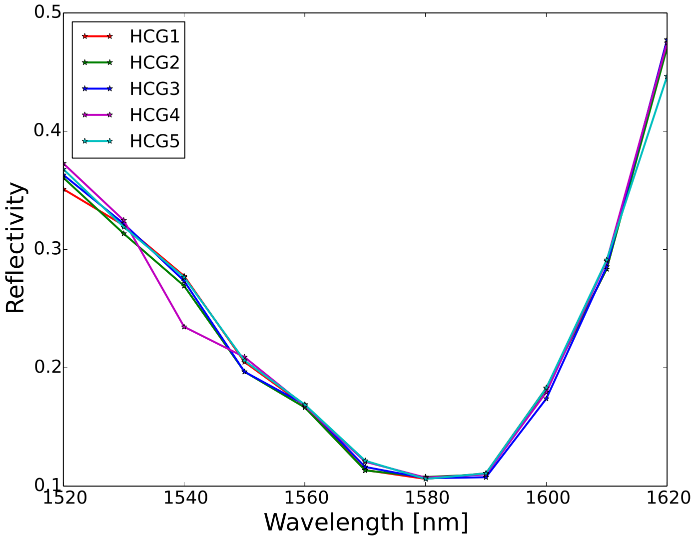

Figure 5.22: Measurement data for air-clad HCGs. We also plot the simulation for an air-clad trapezoidal HCG which has Λ =748 nm, t_g =220 nm and parallel sides 432 nm (top) and 508 nm (bottom) long respectively.

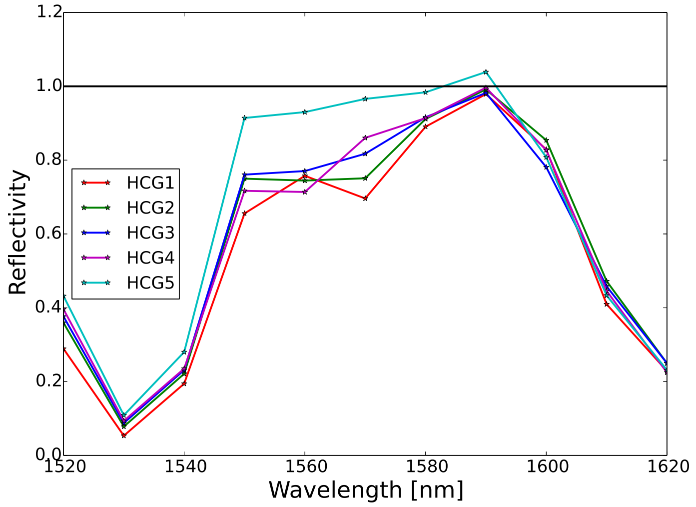

Figure 5.23: Measurement data for LC-clad HCGs for an applied voltage of 0 V$_{rms}$.

LC-clad HCGs.

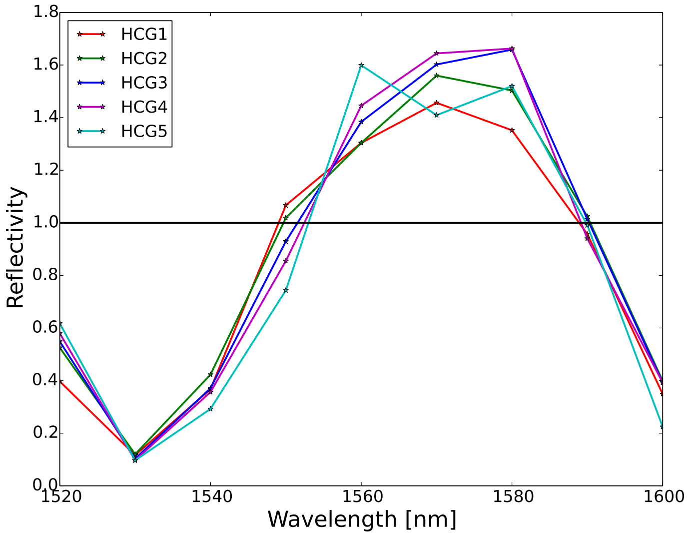

Figure 5.24: Measurement data for LC-clad HCGs for an applied voltage of 20 V_{rms}.

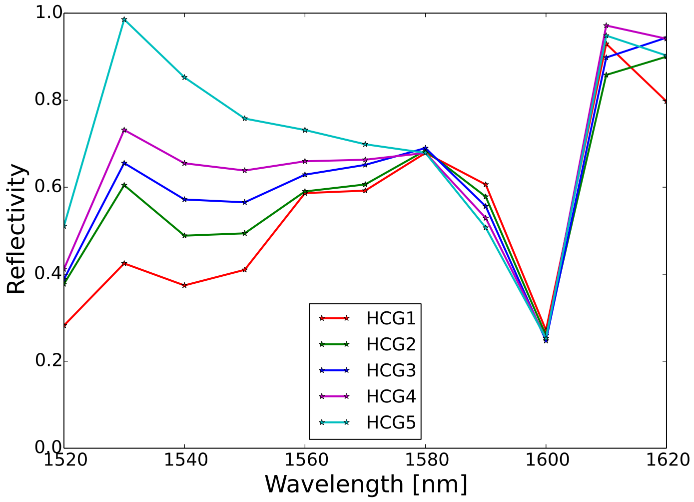

Figure 5.25: Measurement data for LC-clad HCGs for an applied voltage of 67 V_{rms}.

5.7 Discussion

Several issues affect the performance of the LC-clad HCGs, we consider them in this section. It is not possible to accurately measure the reflectivity of the HCGs because of the inaccuracy of the normalization measurement for LC-clad HCGs. For the air-clad HCG measurements, the reflection of the dummy tiling structures surrounding the HCGs is approximated quite well by a uniform layer of silicon. Consequently, the normalization for the air-clad case is good and the measurement is in excellent agreement with the simulation. However, when the dummy tilings are LC-clad, their reflection is very complicated. This is mainly due to variations in the LC alignment. Fig. 5.19 shows that the LC alignment (even for 0 V) over the dummy tilings is not as uniform as above the HCGs. Hence, using it as a benchmark for obtaining reflectivity for the LC-clad HCGs results in the larger-than-unity values we see. This can be resolved by using the reflection from a uniform silicon or gold layer as the normalization. In this case, the measurement can be made easier by evaporating a layer of gold onto the chip close to the HCGs.

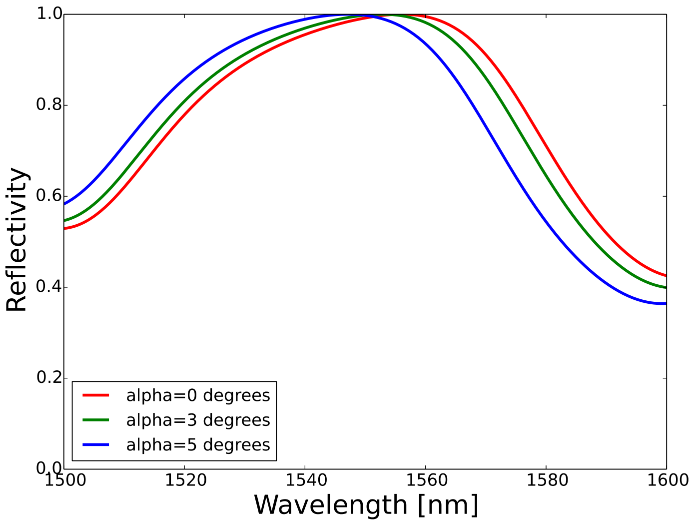

Figure 5.26: Simulation of the variation of the reflectivity of an LC-clad trapezoidal (Λ =748 nm, t_g =220 nm and parallel sides 432 nm (top) and 508 nm (bottom) long respectively) HCG with the angle of incidence (alpha) with respect to the normal for 0 V$_{rms}$.

Another issue which has an impact on the measurements is the size of the HCGs. Due to their small size (50 μm by 50 μm), a complicated measurement set-up is required to measure the reflection. Increasing the size of the HCGs will eliminate the need to focus the laser beam onto the HCG. Furthermore, the focusing of the laser beam means the beam reaching the HCGs contains normal as well as off-normal components. The HCGs were designed for normally incident TE polarized light. If the incident beam makes a small angle with the normal to the HCG, the high quality resonance peaks shifts to a different wavelength as shown in fig.5.26.Consequently, even though we use a pin hole to block off-axis beam components, the small cone of angles (around the normal) it transmits may result in the measurement of a broader peak.

A final issue which could have an impact on the performance of the HCG devices considered in this thesis. In the current configuration of the LC cell, high applied voltages are needed to switch the LC. This is mainly due to the fact that in addition to the LC, there are respectively 2 μm and 220 nm thick oxide and silicon (the HCG) layers. The magnitude of the applied voltage needed to reorient the LC can be reduced by contacting the HCG bars, so they function as electrodes. Moreover, in such a design, applying different voltages to different HCG bars would make it possible to focus and/or steer the reflection of the HCG. This would result in smart HCGs with widely tunable reflective properties.

5.8 Conclusion

HCGs are near-wavelength gratings whose bars have a high refractive index contrast with their surroundings. Their reflection exhibits novel features like broadband high reflectivity (for TM polarized light) and high quality resonances (for TE polarized light). HCGs support sub-wavelength waveguide array modes. Since they are near-wavelength, only two such modes can propagate. These modes accumulate phase as they propagate in the HCG in the normal direction. When these modes attain their Fabry-Perot resonance conditions simultaneously, the reflection exhibits broadband high reflectivity and high quality resonance peaks if they have a relative phase of π and 2π respectively. When a HCG is LC-clad, the LC causes the reflection of the HCG to shift to a different wavelengths. For TE polarized high quality resonance peaks, the inclusion of the LC leads to a redshift compared to the air-clad case. The reflectivity of the LC-clad HCG can be tuned by varying the voltage over the LC. In this thesis, we only consider tuning of the high quality resonance peaks which arise when TE polarized light is incident on a HCG.

We design HCGs which exhibit high quality resonances in the wavelength range between 1500 nm and 1700 nm. The HCGs we designed are fabricated by IMEC. We integrate the fabricated HCGs into conventional LC cells and obtain LC-clad HCGs with electrical contacts for applying a voltage over the LC. Measurements confirm the LC-clad HCGs have voltage tunable reflectivity.

Bibliography

[1] *A compact optical spectrometer based on a single-grating Fresnel diffractive optical element*, volume 8374, 2012.

[2] Maurine Malak, Konstantins Jefimovs, Irène Philipoussis, Joab Di Francesco, and Toralf Scharf. *On-chip near-infrared optical spectrometer based on single-mode Epo waveguide and gold nanoantennas*. Journal of Micro/Nanolithography, MEMS, and MOEMS, 13(2):023011, 2014.

[3] Junseok Heo, Zifan Zhou, Wei Guo, Boon S. Ooi, and Pallab Bhattacharya. *Characteristics of AlN/GaN nanowire Bragg mirror grown on (001) silicon by molecular beam epitaxy*. Applied Physics Letters, 103(18):–, 2013.

[4] Sun-Kyung Kim and Hong-Gyu Park. *Coherent vertical beaming using Bragg mirrors for high-efficiency GaN light-emitting diodes*. Opt. Express, 21(12):14566–14572, Jun 2013.

[5] Geert Morthier and Patrick Vankwikelberge. *Handbook of distributed feedback laser diodes*. Artech House, 2nd edition, 1997.

[6] Martin Maiwald, Jörg Fricke, Arnim Ginolas, Johannes Pohl, Bernd Sumpf, Götz Erbert, and Günther Tränkle. *Dual-wavelength monolithic Y-branch distributed Bragg reflection diode laser at 671 nm suitable for shifted excitation Raman difference spectroscopy*. Laser & Photonics Reviews, 7(4):L30–L33, 2013.

[7] Feng Xie, Catherine G. Caneau, Herve P. LeBlanc, Ming-tsung Ho, Jie Wang, Satish Chaparala, Lawrence C. Hughes, and Chung-en Zah. *High power and high temperature continuous-wave operation of distributed Bragg reflector quantum cascade lasers*. Applied Physics Letters, 104(7):–, 2014.

[8] Jacques Albert, Li-Yang Shao, and Christophe Caucheteur. *Tilted fiber Bragg grating sensors*. Laser & Photonics Reviews, 7(1):83–108, 2013.

[9] Amelia L. Ricchiuti, David Barrera, Koji Nonaka, and Salvador Sales. *Temperature Gradient Sensor Based on a Long Fiber Bragg Grating and Time Waveform Analysis*. In Advanced Photonics, page SeW3C.5. Optical Society of America, 2014.

[10] Wending Zhang, Ligang Huang, Feng Gao, Fang Bo, Li Xuan, Guoquan Zhang, and Jingjun Xu. *Tunable add/drop channel coupler based on an acousto-optic tunable filter and a tapered fiber*. Opt. Lett., 37(7):1241–1243, Apr 2012.

[11] V.B. Voloshinov, G.A. Knyazev, L.A. Kulakova, and N. Gupta. *Acousto-optic control of light beams in the infrared range*. Physics of Wave Phenomena, 21(2):134–138, 2013.

[12] S. Liebich, M. Zimprich, A. Beyer, C. Lange, D. J. Franzbach, S. Chatterjee, N. Hossain, S. J. Sweeney, K. Volz, B. Kunert, and W. Stolz. *Laser operation of Ga(NAsP) lattice-matched to (001) silicon substrate*. Applied Physics Letters, 99(7):–, 2011.

[13] Christoph Berger, Armin Dadgar, Jürgen Bläsing, Alexander Franke, Thomas Hempel, Rüdiger Goldhahn, Jürgen Christen, and Alois Krost. *Growth of AlInN/AlGaN distributed Bragg reflectors for high quality microcavities*. physica status solidi (c), 9(5):1253–1258, 2012.

[14] C. Gierl, T. Gruendl, P. Debernardi, K. Zogal, C. Grasse, H. A. Davani, G. Böhm, S. Jatta, F. Küppers, P. Meißner, and M.-C. Amann. *Surface micromachined tunable 1.55 μm-VCSEL with 102 nm continuous single-mode tuning*. Opt. Express, 19(18):17336–17343, Aug 2011.

[15] W.P. Pallmann, C.A. Zaugg, M. Mangold, V.J. Wittwer, H. Moench, S. Gronenborn, M. Miller, B.W. Tilma, T. Südmeyer, and U. Keller. *Gain characterization and passive modelocking of electrically pumped VECSELs*. Opt. Express, 20(22):24791–24802, Oct 2012.

[16] V. Karagodsky, F.G. Sedqwick, and C.J. Chang-Hasnain. *Theoretical analysis of subwavelength high contrast grating reflectors*. Opt. Express, 18(16), 2010.

[17] V. Karagodsky and C.J. Chang-Hasnain. *Physics of near-wavelength high contrast gratings*. Opt. Express, 20(10), 2012.

[18] Connie J. Chang-Hasnain and Weijian Yang. *High-contrast gratings for integrated optoelectronics*. Adv. Opt. Photon., 4(3):379–440, Sep 2012.

[19] *COMSOL Multiphysics v4.3a. RF Module model library, refrence guide and user's guide.* `http://www.comsol.com`. Accessed: 2014-12-04.

[20] *RefractiveIndex.info, Refractive index database.* `http://refractiveindex.info/?shelf=main&book=Si&page=Li-293K`. Accessed: 2015-01-27.

[21] *ePIXfab*. `http://www.epixfab.eu`. Accessed: 2014-11-12.

6
Conclusion

6.1 Introduction

The work presented in this book provides the reader with a better understanding of the tunability of shallow-etched, deep-etched and slot waveguides and high contrast gratings. The basic working principle of each device is explained. Understanding of liquid crystals is then applied in each case to extend the working principle to cases where the device is in contact with an anisotropic medium. In each case, the working principle is used to design devices with desirable characteristics. Experimental characterization of the devices then follows. The results of the characterization are compared with simulations to confirm that the devices function as expected. The outcome is a theoretical framework, designs and experimental devices related to the tuning of silicon photonic components. The main achievements of this work are stated in the following section.

6.2 Achievements

- Designs for LC-clad shallow-etched waveguides with tunable lateral leakage loss and hence tunable magic width and magic wavelength are obtained. In particular, we show that the magic width can be tuned by 20 nm (from 780 nm to 800 nm) by reorienting the LC director from being aligned along the longitudinal (parallel to the waveguides) direction to being aligned along the vertical (perpendicular to the waveguides top surface) direction. In this case, the lateral leakage loss of the 780 nm wide shallow-etched waveguide can be modulated from 0 dB/cm to 20 dB/cm by reorienting the LC as mentioned earlier. With regards to the wavelength tunability, we show that the magic wavelength of a 790 nm waveguide can be switched by 78 nm (from 1588 nm to 1510 nm) by reorienting the LC director from being aligned along the longitudinal direction to being aligned along the vertical direction.

- LC cells integrating a silicon chip with shallow-etched waveguides and LCs are obtained. The shallow-etched waveguides in the cells are fabricated according to the designs obtained earlier. Optical and electrical characterization of the LC cells confirm that the lateral leakage of the waveguides can indeed be tuned with an applied voltage. The magic wavelength of a 785 nm wide shallow-etched waveguide can be tuned by 39.5 nm (from 1564 nm to 1524.5 nm) by increasing the applied voltage over the LC from 0 V$_{rms}$ to 201 V$_{rms}$. The lateral leakage loss of a given waveguide can be modulated at a fixed wavelength by an applied voltage. At a wavelength of 1570 nm, the lateral leakage of the 785 nm wide waveguide can be switched by 15.8 dB/cm, from 5.7 dB/cm at 0 V$_{rms}$ to 21.5 dB/cm at 201 V$_{rms}$.

- Designs of LC-clad HCGs whose reflectivity exhibit high quality resonance peaks in the wavelength range between 1500 nm and 1700 nm are obtained. It is shown that the position of the high quality resonance peaks of a rectangular HCG with a period of 764 nm, fill factor of 70$\%$ and thickness 220 nm can be shifted by 40 nm (from 1656 nm to 1616 nm) by reorienting the LC director from being aligned along the HCG bars to being aligned vertically (perpendicular to the top surface of the HCG bars). It is also shown that trapezoidal HCGs exhibit high quality resonance peaks. However, the latter are broader than those of rectangular HCGs. For a trapezoidal HCG with parallel sides 432 nm and 508 nm long, a thickness of 220 nm and a period of 748 nm, the position of the high quality resonance peak can be shifted by over 50 nm (from 1558 nm to 1505 nm).

- LC cells in which the trapezoidal HCGs are integrated with LCs are obtained. Measurements of the reflection of the LC-clad HCGs as a function of the applied voltage show that the high quality resonance peaks of the HCGs shift to lower wavelengths with increasing applied voltage. The position of the high resonance peak is shifted by at least 10 nm. It is also shown that for fixed wavelengths the reflection of the trapezoidal HCG can be modulated by varying the applied voltage. For 1550 nm the reflection of the HCGs is high at 0 V$_{rms}$. As the applied voltage is increased, the reflection decreases until it attains a minimum at 13 V$_{rms}$. A further increase in applied voltage then results in an increasing reflection until we once more attain a maximum at 20 V$_{rms}$. From here it decreases again to another minimum and a maximum at 30 V$_{rms}$ and 45 V$_{rms}$ respectively.

- A design for a voltage controlled on-chip integrated optical switch is obtained. The switch is based on an LC-clad LC-clad deep-etched waveguides. It is shown that the modes of 450 nm wide deep-etched waveguides can be tuned when they are LC-clad. For narrower air-clad deep-etched waveguides, we find no guided modes. However, when they are LC-clad it is determined that the loss of the waveguide modes can be increased by increasing the applied voltage over the LC. It is shown that the loss of the TE and TM modes in an 200 nm wide LC-clad deep-etched waveguide can be increased from 0 dB/cm to 5 dB/cm and 0 dB/cm to 3.3 dB/cm respectively by increasing the applied voltage over the LC from 0 V to 200 V. Finally, for a 180 nm wide LC-clad deep-etched, it is not possible to work with the TE mode since it has a loss of about 50 dB/cm for no applied voltage. On the other hand, the loss of the TM mode can be increased from 0 dB/cm to over 50 dB/cm by increasing the applied voltage from 0 V to 200 V.

6.3 Outlook

The work carried out during this PhD has led to a better understanding of the tuning of silicon photonic components with LCs. However, there are some interesting aspects of the devices studied in this thesis which could not be investigated due to lack of time. They are listed below:

- In proof-of-principle investigations such as the ones carried out in this thesis, the emphasis is usually placed on exploring the basic functionality of the device. In our case, this corresponds to altering the properties/functionality of passive silicon photonic components by switching their LC cladding. In this thesis we provide adequate evidence of the altering basic functionality of silicon photonic devices. However, we don't investigate the integration of these LC-clad silicon photonic components in more complex systems.
- Voltage tuning of the lateral leakage loss of shallow-etched waveguides was demonstrated. High applied voltages had to be used because the bottom part of the chip functioned as the second electrode of the cell. The applied voltage can be reduced by fabricating waveguides with electrical contacts to the shallow-etched cladding of the waveguides. Additionally, designs could be conceived where patterned electrodes placed in the shallow-etched cladding at a suitable distance from the waveguide core are used to electrically control the orientation of the LC cladding along the length of the waveguide. This could lead to waveguides in which the phase and loss of the waveguide modes can be dynamically controlled in the longitudinal direction.
- Further measurements need to be performed to better characterize the HCGs studied in this thesis. It would be desirable to fabricate a new design with larger HCGs. This should make the measurements easier and yield more conclusive evidence of the tunability of HCGs. Additionally, the top-bottom voltage tuning used for tuning the LC-clad HCGs requires large applied voltages. The same tuning can be achieved by making contacts to the HCG bars. Moreover, by applying different voltages to different HCG bars, we could obtain a device with voltage steerable/focus-able reflectivity.
- Voltage-dependent loss and subsequent cut-off is demonstrated for sufficiently narrow LC-clad deep-etched waveguides. The next step should be the fabrication and characterization of these devices.

The work carried out in this thesis opens up very attractive possibilities for realizing photonic integrated circuits, components and systems with tunable functionality. Shallow-etched waveguides typically have low propagation loss, but they are usually only excited with TE polarized light due to the lateral leakage loss phenomenon of TM modes. It is shown that when these waveguides are LC-clad, they can be used in practical devices with both polarizations. One of the main advantages of the LC-clad shallow-etched waveguides studied in this thesis is the fact that they are wider than other silicon photonic single-mode waveguides and hence are potentially more fabrication tolerant. Moreover, we show that the magic wavelength of a given shallow-etched waveguide can be tuned over a 40 nm wide wavelength window. This makes these waveguides attractive as low-loss single-mode tunable interconnects for wavelength division multiplication applications. The selective wavelength transmission of the LC-clad shallow-etched waveguides is accompanied by a tunable (and high) extinction ratio (about 20 dB/cm). This makes them very attractive for applications where it is necessary to accurately control the loss and polarization of on-chip signals. One example of such a device is a Mach-Zhender interferometer in which the contrast between the different arms is precisely adjustable. Finally, the power lost from the shallow-etched waveguide is converted to coherent TE polarized radiation. Accordingly, by dynamically controlling the rate of leakage along the waveguide, it should be possible to achieve on-chip beam forming. This opens up possibilities for applications in information processing, signal routing, information imaging and sensing.

In contrast, the LC-clad HCGs studied in this thesis open up the possibility for applications with compact voltage-tunable reflectors. Designs could be conceived in which the reflection of an HCG can be steered and/or focused in addition to being tuned. Such focusable steerers are especially interesting as replacements for microelectromechanical (MEM) mirrors. Finally, we show that the loss of the modes in narrow deep-etched waveguides can be increased with an applied voltage. This functionality is once more very interesting for applications where it is necessary to accurately control the loss of a signal on-chip.

A

Measurement data - HCG Reflection

For each wavelength we perform 7 measurements. Two normalization (N_1 and N_2) measurements and one measurement for each grating (G_1, G_2, G_3, G_4 and G_5). The regions of the chip below and above the gratings are used for the normalization measurements.The reflectivity of a grating is calculated using both normalizations. For example the reflectivity of G_1 at a given wavelength is given by;

$$R_1 = \frac{2 * G_1 * R_{Si}}{N_1 + N_2} \tag{A.1}$$

with R_{Si} is the simulated reflection (for the wavelength considered) of a 220 nm thick silicon layer sitting on a 2 μm thick silica layer which is itself supported by a silicon substrate. The experimentally measured reflection of the HCGs in air is given in table A.1.

	N_1	G_1	G_2	G_3	G_4	G_5	N_2
1520 nm	98	146	150	151	155	153	85
1530 nm	134	228	223	229	231	227	125
1540 nm	140	265	257	261	224	264	133
1550 nm	180	348	334	334	355	350	180
1560 nm	152	351	348	353	351	353	149
1570 nm	167	388	387	397	412	415	161
1580 nm	69	195	198	196	197	195	67
1590 nm	75	234	232	227	232	234	77
1600 nm	82	301	300	286	295	301	89
1610 nm	83	296	296	298	303	304	84
1620 nm	94	355	350	355	353	332	83

Table A.1: Reflected power in arbitrary units for an air clad HCG.

	N_1	G_1	G_2	G_3	G_4	G_5	N_2
1520 nm	196	625	777	814	856	934	234
1530 nm	141	414	606	681	726	844	216
1540 nm	193	558	635	664	675	804	140
1550 nm	86	299	342	347	327	417	70
1560 nm	79	294	289	299	277	361	143
1570 nm	54	178	192	209	220	247	125
1580 nm	106	382	391	393	392	422	202
1590 nm	180	622	630	624	633	660	219
1600 nm	148	431	444	406	430	420	86
1610 nm	172	432	498	483	470	457	79
1620 nm	64	174	190	190	171	176	41

Table A.2: Reflected power in arbitrary units for an LC clad HCG for 0 V_{rms}.

	N_1	G_1	G_2	G_3	G_4	G_5	N_2
1520 nm	70	440	582	608	642	684	176
1530 nm	86	304	313	269	254	252	34
1540 nm	84	304	350	307	295	242	13
1550 nm	70	287	274	250	230	200	22
1560 nm	30	212	212	225	235	260	63
1570 nm	57	310	332	341	350	300	92
1580 nm	74	322	358	395	396	362	97
1590 nm	134	285	305	302	280	295	53
1600 nm	186	280	320	315	315	180	175

Table A.3: Reflected power in arbitrary units for an LC clad HCG for 30 V_{rms}.

	N_1	G_1	G_2	G_3	G_4	G_5	N_2
1520 nm	109	517	692	712	755	936	100
1530 nm	109	418	595	645	720	970	202
1540 nm	131	360	470	550	630	820	350
1550 nm	140	230	277	317	358	425	201
1560 nm	259	457	460	490	514	570	232
1570 nm	260	500	512	550	560	590	218
1580 nm	310	850	857	864	850	850	231
1590 nm	124	630	601	578	550	527	165
1600 nm	110	362	346	330	337	337	165
1610 nm	71	442	408	427	462	451	65
1620 nm	55	310	350	367	366	351	134

Table A.4: Reflected power in arbitrary units for an LC clad HCG for 100 V_{rms}.

B
Publications list

B.1 Journal papers

1. Yufei Xing, **Thomas Ako**, John George, Dietmar Korn, Hui Yu, Peter Verheyen, Marianna Pantouvaki, Guy Lepage, Philippe Absil, Christian Koos, Juerg Leuthold, Jeroen Beeckman, Wim Bogaerts, ***Digitally controlled phase shifter using a silicon slot waveguide with liquid crystal infiltration.*** IEEE PHOTONICS TECHNOLOGY LETTERS Vol. 27. Jun. 2015.

2. **Thomas Ako**, Anthony Hope, Jeroen Beeckman, Wim Bogaerts and Kristiaan Neyts, ***Electrically tuneable lateral leakage loss in shallow-etched silicon waveguides.*** OPTICS EXPRESS. Vol. 23. Jan. 2015.

3. Aimi Abbas, Said Rahimzadeh-Kalaleh Rodriguez, **Thomas Ako**, Tangi Aubert, Marc Verschuuren, Dries Van Thourhout, Jeroen Beeckman, Zeger Hens, Jaime Gomez Rivas and Bjorn Maes, ***Active liquid crystal tuning of metallic nanoantenna enhanced light emission from colloidal quantum Dots.*** ACS NANO LETTERS. Sep. 2014.

4. **Thomas Ako**, Jeroen Beeckman, Wim Bogaerts and Kristiaan Neyts, ***Tuning the lateral leakage loss of TM-like modes in shallow-etched waveguides using liquid crystals.*** APPLIED OPTICS. Vol. 53. Jan. 2014.

B.2 Conference papers

1. Yufei Xing, **Thomas Ako**, John George, Dietmar Korn, Hui Yu, Peter Verheyen, Marianna Pantouvaki, Guy Lepage, Philippe Absil, Christian Koos, Juerg Leuthold, Jeroen Beeckman, Wim Bogaerts, ***Direct digital control of an efficient silicon+liquid***

crystal phase shifter. 11th International Conference on Group IV Photonics (GFP), France, p.43-44 (2014).

2. **Thomas Ako**, Jeroen Beeckman and Kristiaan Neyts, ***Lateral leakage loss of TM-like modes in silicon-on-insulator ridge waveguides.*** Proceedings of the Symposium of the IEEE Photonics Society Benelux Chapter. Mons 2012.
3. **Thomas Ako**, Jeroen Beeckman and Kristiaan Neyts, ***Silicon-on-insulator (SOI) rib waveguides with liquid crystal overlay.*** 13th International Symposium on Colloidal and Molecular Electrooptics, Abstracts. Ghent 2012.
4. **Thomas Ako**, Jeroen Beeckman and Kristiaan Neyts, ***Silicon-on-Insulator (SOI) optical waveguides with liquid crystals.*** 24th International Liquid Crystal Conference, Abstracts. Mainz 2012.
5. Kristiaan Neyts, Wout De Cort, **Thomas Ako**, Roel Baets and Jeroen Beeckman, ***Tuning and trimming of SOI ring resonators with liquid crystal.*** 4th Workshop on Liquid Crystals for Photonics, Abstracts. HKUST, Hong Kong. 2012. 12-12.
6. Kristiaan Neyts, **Thomas Ako**, Wout De Cort, Pieter Vanbrabant and Jeroen Beeckman. ***Waveguides with liquid crystals.*** Proceedings of the SPIE: the international society for optical engineering. SPIE. Vol. 8114. San Diego 2011.